2017

Statistical Analysis of Multi-Row Film Cooling Flowfields

Craig Fernandes
University of Central Florida

STATISTICAL ANALYSIS OF MULTI-ROW FILM COOLING FLOW FIELDS

by

CRAIG PATRICK FERNANDES
B.S. University of Central Florida, 2014

A thesis submitted in partial fulfilment of the requirements
for the degree of Master of Science
in the Department of Mechanical and Aerospace Engineering
in the College of Engineering and Computer Science
at the University of Central Florida
Orlando, Florida

Summer Term
2017

Major Professor: Jayanta S. Kapat

ABSTRACT

A huge part of modern day power generation research and development strives to achieve higher thermal efficiencies and specific work outputs for both gas turbine Brayton and combined cycles. Advances in cooling technologies, both internal to turbine blades and external, provide the easiest way to accomplish this by raising the turbine inlet temperature far beyond the super-alloy's allowable temperature. Discrete film cooling injection, an external cooling technique, ensures a cool blanket of compressed air protects the blade surface from the harsh mainstream gas. To optimize the coverage and effectiveness of the film, a thorough understanding of the behavior and flow physics is necessary.

The objective of the current study is to use hotwire anemometry as a tool to conduct 1D time-resolved turbulent measurements on the flow field of staggered multi-row film cooling arrays with cylindrical and diffuser shaped holes inclined at 20 degrees to the freestream. The study aims to investigate the flowfield to determine why the performance of diffuser shaped jets is enhanced even at comparatively high blowing ratios. In addition, blowing ratio effects and flowfield discrepancies at set downstream locations in the array centerline plane are also investigated.

The experiments are conducted on an open-loop wind tunnel for blowing ratios in the range of 0.3 to 1.5 at a density ratio of 1. Boundary layer measurements were taken at 12 locations at the array centerline to obtain mean velocity, turbulence level, turbulence intensity, and integral length scales. Measurements were also taken at a location upstream of the array to characterize the incoming boundary layer and estimate the wall normal position of the probe in comparison with the logarithmic law of the wall.

Mean effective velocity profiles were found to scale with blowing ratio for both geometries. A strong dependence of turbulence levels on velocity gradients between jets and the local fluid was

also noticed. For cylindrical jets, attached cases displayed lower integral length scales in the near wall region compared with higher blowing ratio cases. This was found to be due to entrainment of mainstream fluid showing increased momentum transport below the jets. Diffuser cases at all blowing ratios tested do not show increased length scales near the wall demonstrating their enhanced surface coverage. Row-to-row discrepancies in mean velocity and turbulence level are only evident at extremely high blowing cases for cylindrical, but show significant deviations for diffuser cases at all blowing ratios.

Unlike the cylindrical cases, jets from diffuser shaped holes, due to their extremely low injecting velocities, dragged the boundary layer with each row of blowing. Increased velocity gradients create a rise in peak turbulence levels at downstream locations. At high blowing ratios however, faster moving fluid, due to injection, at lower elevations acts as a shield for downstream jets allowing significantly further propagation downstream. Near the wall low magnitude integral length scales are noticed for diffuser jets indicating low momentum transport in this region.

The results show good agreement with effectiveness measurements of a previous study at a higher density ratio. However, to accurately draw the comparison, effectiveness measurements should be conducted at a density ratio of 1. Recommendations were made to further the study of multi-row film cooled boundary layers. The scope includes a CFD component, other flowfield measurement techniques, and surface effectiveness studies using N2 as the coolant for a much broader picture of this flowfield.

ACKNOWLEDGMENTS

First and foremost, thank you Dr. Jayanta Kapat for your guidance, and support all throughout my graduate career.

Thank you to my committee members: Dr. Kareem Ahmed and Dr. Subith Vasu.

A special thanks to Dr. Greg Natsui for mentoring me in my early stages as a grad student.

Thank you to Tyler Voet and Zachary Little for your abundant help in co-authoring my publications.

Thank you to Justin and Erik for their continual support and guidance through the critical stages of this thesis.

Thanks to Siemens Energy for their collaboration and support of research projects I worked on at CATER.

Finally thanks to everyone at the Center for Advanced Turbomachinery and Energy Research for all the knowledge, experiences, work and ideas shared.

TABLE OF CONTENTS

LIST OF FIGURES

LIST OF TABLES

CHAPTER 1: INTRODUCTION

Demand for electricity continues to increase and rules and regulations on cleaner energy generation push natural gas and renewable energy projections to approximately 1500 and 1250 billion kilowatt-hours by the year 2030. Lower natural gas prices coupled with high resource availability and technology advancements are leading to the retirement of power plants with coal-fired electricity generation. In addition, renewable energy sources are still not able to meet global demands, hence natural gas is projected to be the primary source of electricity generation [1].

Turbines are a predominant means of power extraction from resources like natural gas, hydroelectricity, wind, nuclear and coal. Gas turbines in particular produce 90% of the worlds power and 98% of aero-propulsion thus exemplifying the worlds reliance on this magnificent technology.

Due to their strong impact on energy production and stringent rules and regulations on emissions, even incremental improvements in the specific work output, efficiency and reduction in NOx emissions in particular are of great importance. Improvements in specific work output of a gas turbine call for a better look at the Brayton cycle upon which it operates. The Brayton cycle ideally consists of four steps, isentropic compression, isobaric heat addition, isentropic expansion and isobaric heat extraction. The specific work output can then be defined as:

$$\frac{W}{c_p T_1} = \frac{T_3}{T_1}\Big[1 - \Big(\frac{P_2}{P_1}\Big)^{\left(\frac{1-\gamma}{\gamma}\right)}\Big] - \Big[\Big(\frac{P_2}{P_1}\Big)^{\frac{\gamma-1}{\gamma}} - 1\Big] \tag{1.1}$$

Equation 1.1 above shows that an increase in specific work output of a Brayton cycle can be achieved by increasing the turbine inlet temperature given by T_3. Modern gas turbines incorporate a series of highly advanced cooling techniques to optimally increase the turbine inlet temperature (TIT) that the first stage turbine blades see. Current firing temperatures far exceed the metal allow-

able temperatures thanks to advances and implementation of thermal barrier coatings and various cooling techniques. While thermal barrier coatings protect the surface from the harsh nature of the hot gas, cooling techniques bleed high pressure cold air from the compressor, and duct it to the first stages of the turbine. They generally operate by providing a heat sink for the removal of heat from the material. This extraction of compressed air causes a proportional decrease in net work output and ultimately the efficiency of the cycle. The reduction in efficiency needs to be more than compensated by the effects of cooling the blades and vanes by increasing the TIT. Impingement, rib turbulators, and trailing edge pins are some of the internal cooling techniques used in modern day turbine blades. While these cooling techniques have a huge impact on the lifespan of turbine blades, they are hindered by manufacturing limitations and with the onset of implementing additive manufactured of gas turbine blades, the horizons of blade design have been widened.

Contrary to the heat sink approach to cooling a turbine blade, film cooling is an external cooling technique that aims to create a relatively cold blanket layer just above the blade surface. A Secondary fluid (coolant) is injected at one or more discrete locations on a surface which is exposed to an environment of high temperature and serves to protect the surface in the immediate and downstream regions [2]. In effect, the blade sees the film temperature rather than the temperature of the hot gas thus reducing the temperature gradient above the surface causing less heat transfer. Coverage of the surface and film cooling effectiveness are in essence the two main parameters that drive research and development of this particular cooling technology. While this may seem trivial, jet in cross-flow scenarios are very complex and the flow physics are governed by hole geometry, configuration of airfoil geometry and turbulent coolant/mainstream conditions, which give it additional complexity [3].

Several decades of research has been conducted on various combinations of parameters to optimize the performance and understanding of these extremely complex flow phenomena. Goldstein et. al. [2], Bogard and Thole [4], and Han et. al. [3] all provide excellent summaries of the

aforementioned research efforts and developments of film cooling. The various parameters that are common to film cooling research and which affect performance are introduced below.

Geometric parameters

This section defines the variables and film cooling parameters that pertain to the discussion of the flowfield. It incorporates geometric as well as fluid condition definitions.

Hole Diameter, d: defined as the cross section of the cylindrical portion of the hole and is used to non-dimensionalize all other quantifiable length measurements.

Inclination Angle, α: defined as the angle between the film cooling surface and the hole axis in the wall normal direction.

Hole Length, L: defined as the length from the hole axis from plenum side to film cooling surface side.

Compound Angle, β: defined as the angle between hole axis projected onto the film cooling surface and the streamwise direction of mainstream flow.

Lateral Pitch, P_z: defined as the distance between the hole axis breakout of two holes in the lateral (z) direction.

Streamwise Pitch, P_x: defined as the distance between the hole axis breakout of two holes in the streamwise (x) direction.

Lateral Expansion Angles, $\Phi_{1,2}$: defined for diffuser shaped holes as the angle between the hole axis and the side walls (span-wise direction) of the hole.

Layback Angle, Φ_3: defined for diffuser shaped holes as the angle between the hole axis and the bottom wall (streamwise direction) of the diffused hole.

Plunge Depth, L: defined for diffuser shaped holes as the length of the hole where the diffuser shaping is applied.

Area Ratio, AR: defined as the hole exit to inlet area of a film cooling hole. This definition is more relevant for shaped holes where the inlet to exit areas differ.

Flow Condition parameters

Freestream Turbulence Intensity, T.I.: defined as a scale that characterizes the turbulence expressed as a percentage. Ideal flow with no turbulent instabilities would result in a T.I. of 0%. Engine like conditions are approximately 12%.

Blowing Ratio, M: also known as the mass flux ratio is defined as the ratio of coolant mass flux to mainstream mass flux.

$$M = \frac{(\rho U)_c}{(\rho U)_\infty} \tag{1.2}$$

Density Ratio, DR: defined as the ratio of coolant to mainstream density. Typical engine condition density ratio is around 1.8.

$$M = \frac{(\rho)_c}{(\rho)_\infty} \tag{1.3}$$

Momentum Flux Ratio, I: defined as the ratio of coolant to mainstream momentum flux. Can also be derived from the square of blowing ratio divided by the density ratio.

$$M = \frac{(\rho U^2)_c}{(\rho U^2)_\infty} = \frac{M^2}{DR} \tag{1.4}$$

Velocity Ratio, VR: defined as the ratio of coolant to mainstream velocity ratio. Can also be derived from blowing ratio divided by the density ratio.

$$M = \frac{(U)_c}{(U)_\infty} \tag{1.5}$$

CHAPTER 2: LITERATURE REVIEW

Several research efforts have been made to study the various parameters that govern the film cooling performance. Since the jet in cross-flow scenario cannot be solved analytically, studying individual parameters and combinations of helps with predictability of flow behavior and development of approximations for computational modeling. The following paragraphs briefly outlines some of the research efforts conducted over the past few decades to give a better understanding of the parameters and how they influence film cooling performance.

General Film Cooling

Baldauf et. al. – 2002 [5]

Baldauf et. al. conducted flat plate film cooling effectiveness measurements using infrared thermography for coolant injected from a single row of streamwise inclined cylindrical 5mm holes. The researchers tested blowing ratios in the range of 0.2 to 2.5, varying density ratio = 1.2, 1.5, and 1.8 and in effect varied momentum flux ratio as well. In addition, mainstream turbulence intensity was varied at 1.5% and 4%. Geometric changes were also made where hole inclination angles of 30, 60, and 90 degrees were tested upon and three different lateral pitches = 2d, 3d, and 5d. From the variety of blowing ratio variations, peak laterally averaged effectiveness was observed at low blowing ratios just downstream of injection, and is diluted fast by the mainstream flow. Low to moderate blowing ratios showed increased magnitude of the peak laterally averaged effectiveness further downstream of injection as compared to that of low blowing ratio cases. M = 0.6 case was noted to have the highest laterally averaged effectiveness peak. Baldauf et. al. found that M = 1 case was optimal for an injection angle = 30 degrees showing highest overall effectiveness. Jet in

cross-flow mixing generally dominates flow from typical ejection geometry of $P_z/d = 3$ and 30 degree inclination while adjacent jet interactions have a much higher effect for high blowing ratios and large downstream distances.

Gritsch et. al. – 1998 [6]

This study measures film cooling effectiveness using an infrared camera system for three different hole configurations, cylindrical, fan shaped, and laid-back fan shaped at blowing ratios up to 2 and a DR of 1.85. Coolant was injected from a single hole with entrance diameter 10mm and a length to diameter ratio of 6. Additional information about lateral expansion angles and layback angle can be seen in Figure 2.1 below. The shaped hole configuration was chosen such that the length of the cylindrical section at the hole entrance of the expanded holes are at least two hole diameters to allow the flow to reattach before entering the expanded section, and therefore, to improve the diffusion of the flow. Gritsch et. al. found that the holes with expanded exits displayed significantly increased film cooling effectiveness compared to the cylindrical hole, especially at high blowing ratios. It was also shown that laid back fan shaped holes provided better lateral spreading particularly at high blowing ratios, thus having much higher laterally averaged effectiveness. Shaped holes are a large part of the current research efforts thanks to studies such as this one that exemplify the enhancement of adiabatic film cooling effectiveness and coverage.

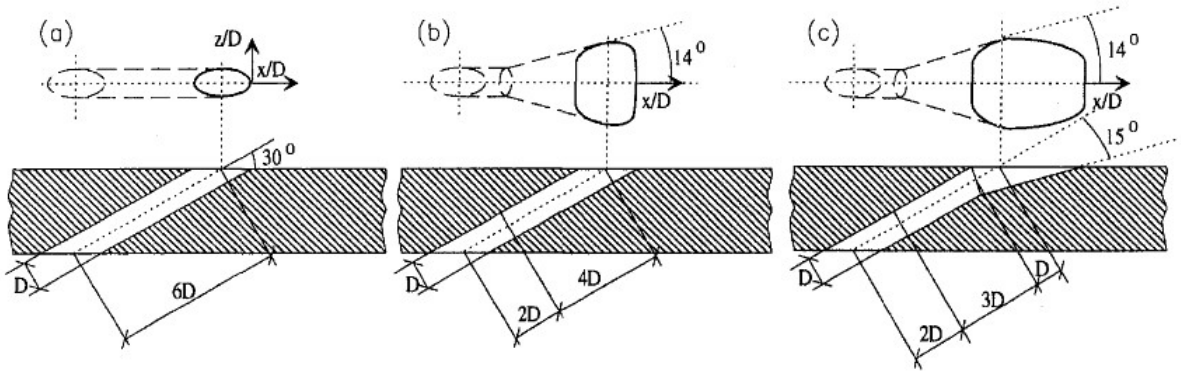

Figure 2.1: Cylindrical, fan-shaped and laid-back fan-shaped film cooling hole geometries by Gritsch et. al. [6]

Burd et. al. – 1999 [7], Burd and Simon 1997 [8]

Burd and Simon conducted single sensor hotwire anemometry at three locations in the exit plane of film cooling holes with varying length and plenum configurations. Measurements were conducted on a single row of 11 holes inclined at 30 degrees to the freestream, with diameter of 19.05mm, span-wise pitch to diameter ratio of 3. Burd and Simon also conducted surface adiabatic effectiveness measurements downstream of the injection site using a traversing thermocouple probe. Findings from this research study show that hole length is a more important distinction compared to the delivery means of the flow i.e. plenum geometry. The study also provides a good dataset of effective velocity and turbulence intensity at the hole exit plane for velocity ratios 0.5 and 1. In a much more in depth publication, Burd and Simon compare spectral distributions of flow at the exit plane for the varying L/d and hole entrance geometries. It was found that nominally, the same ranges of peak-energy frequencies were seen for flows through short and long holes. Slightly higher dominant frequency ranges were noticed for the downstream portion of the hole exit plane in comparison with the hole center and upstream portion. The publication also documents integral lengthscales which are of the same order of magnitude, and dissipation microscales which tend to

be more prominent for short holes with respect to the various hole entrance geometries tested.

Kohli and Bogard – 1997 [9]

Kohli and Bogard conducted experiments on a single row of 35 and 55 degree inclined film cooling flow at a density ratio of 1.6 and varying momentum flux ratios. Cylindrical holes had a nominal diameter of 11.1mm, P_z/d of 3 and L/d of 2.8 which are representative of actual engine conditions. Two component mean velocity, thermal field and turbulence intensity measurements were taken along with centerline and lateral distributions of film cooling effectiveness. Effectiveness measurements were made using ribbon thermocouples glued to the surface, velocity measurements were made using a laser Doppler velocimetry system mounted on a 3D traverse and thermal field measurements were made using a thermocouple probe. Results showed that film cooling effectiveness for 55 degree holes was 10% and 30% lower for low and high momentum flux ratios in comparison with 35 degree holes. 55 degree holes showed much higher diffusion in the thermal field in the region near the holes and was concluded to be the primary reason for decreased effectiveness. From thermal fields, jets were also noticed to begin to merge laterally by x/d = 10 downstream for holes that are spaced 3 diameters apart. Turbulence measurements within, above and immediately downstream of the 55 degree holes were recorded to be much higher indicating a heightened amount of mixing with the mainstream and resulting in greater diffusion of the cooling jet.

Pietrzyk and Bogard – 1990 [10]

This research published is conducted on a single row of 35 degree inclined cylindrical film cooling holes. 2D laser Doppler anemometry was done in a vertical plane along the jet centerline at a blowing ratio of 0.5 and density ratio of 2 and is compared to a previous study of unit density

jets at 0.5 and 1 blowing ratios. Geometry specifications include 11 jets issuing from 12.5mm diameter holes, with L/d = 3.5, and P_z/d = 3. The research provides a detailed discussion of the mean velocity profiles, development of near-field and far field turbulent shear stress, and shear stress correlation coefficients. Results showed significant differences between the dense and unit density jets. Velocity fields at the hole exit for the same velocity ratio were comparable for the different density jets. The dense jet case showed lower velocities in the near wall region than either of the unit density jets. Turbulence levels and uv shear stresses maximum values were comparable downstream of jets for both cases but the relaxation rates for the high density jet was observed to be significantly lower for the dense jet.

Thole, et. al. – 1998 [11]

In a study incorporating the same three geometries as that in the study by Gritsch et. al., this research studied the flowfield of single hole injection at a blowing ratio and density ratio of 1. The study presents 2D mean velocity vectors, and line plots, turbulence intensity and turbulent shear stress at the jet centerline. In addition span-wise turbulence intensity, and streamwise mean velocity is also presented downstream of injection for all three hole geometries. Velocity gradients were significantly reduced for the expanded jets compared to the cylindrical case resulting in lower turbulence production in the downstream region as well. Reduction in jet penetration for expanded holes meant that the peak turbulence levels was observed over the expanded holes whereas injection from cylindrical holes showed peak levels just downstream of the hole exit. Ingestion of mainstream fluid was stated to be a disadvantage of the forward-laterally expanded hole as coolant tended to exit primarily from the leeward side of the hole.

Aga, Rose and Abhari – 2009 [12]

Compound angle studies have been conducted by Aga, Rose and Abhari investigating flat plate film cooling flow structure on a single row of seven cylindrical holes with 20 degree inclination angle and 45 degree compound angle. Other geometric parameters include a hole diameter of 5mm, L/d = 2.8, P_z/d = 4. Three component stereoscopic PIV is used to measure the 3 components of velocity in the flowfield. Flow condition cases with blowing ratios of 1, 2, and 3 and density ratios of 1 and 1.55 are tested. This research showed the skewed vortex structure wherein one part of the classic counter rotating vortex pair structure diminished considerably and a single vortex structure was apparent. Quite remarkably, no jet lift off was observed even for M = 3. Generally the trajectory of the jet vorticity was found to align with the initial injection angle, however the highest momentum jet aligned with the freestream direction due to the vorticity and entrainment effects. High blowing ratios were observed to thin the boundary layer by piling it up on one side of the jet at the expense of the other side. While the thinning of the boundary layer would lead to higher heat transfer, the greater spreading of the coolant (an effect of the compound angle) would cause greater film cooling effectiveness. The Streamwise vortex appeared to maintain its trajectory after ejection. A majority of the coolant rapidly mixed with the freestream due to the actions of the normal vortices and the primary streamwise vortex core causing it to align with the freestream direction after ejection. Greater spreading of normal vorticity in the span-wise direction was observed for the high density ratio case as well. High DR and Low I case also showed loss of horizontal jet momentum and faster mixing into the boundary layer.

Sen, Schmidt, Bogard − 1996 [13]

Sen et. al. also carried out experiments on compound angled film cooling holes but the focus was more so on heat transfer. Three hole configurations were tested upon: a simple cylindrical configuration with no compound angle, a cylindrical hole with β of 60°, and a cylindrical hole with β = 60° and a 15° forward-diffusing expansion at the hole exit. All geometries tested upon had a

single row of 9 holes with diameter of 1.11 cm, α of 35°, P_z/d of 3, and L/d of 4. Momentum flux ratios were varied from 0.16 to 3.9 with a constant density ratio of 1. An IR thermography system was used for heat transfer measurements on a constant heat flux wall. Heat transfer coefficients and net heat flux reduction (a quantification of film cooling performance) was presented for the various test cases. The study showed much higher heat transfer rates at higher momentum flux ratios for β = 60° holes in comparison with the β = 0° case which reduces film cooling performance. This study showed discrepancy in the film cooling performance as that reported by a previous study by the same research group since they used NHFR instead of laterally averaged adiabatic effectiveness and concluded that NHFR should be used if possible.

Takeishi et. al. – 2014 [14]

In quite an unorthodox study, Takeishi et. al. conducted a study using swirling coolant flow in the plenum injected into a low speed wind tunnel with varying angles of the impingement jets used to swirl the flow. Film cooling effectiveness, temperature contours and flow field measurements were conducted using PSP, LIF, and PIV techniques respectively to help analyze the flow structure and impact on cooling performance. Two different hole geometries were tested upon: a 5mm diameter cylindrical hole with inclination angle 30°, and a laid back fan shaped hole with the same diameter and inclination angle, along with 15° lateral and forward expansion angles. Blowing ratios in the range of 0.5-2 at a constant unit density were tested with 0, 10, 20, and 30 degree impingement angles. For cylindrical holes, effectiveness decreased at a low swirl number (a parameter to describe the angular momentum of the coolant) and increased at a high swirl number. Effectiveness was seen to increase for swirling flow injection through cylindrical holes as the kidney vortex structure was destroyed and the film adhered to the surface better. Shaped cooling holes displayed a slightly different trend where an impingement angle of 10° showed maximum effectiveness values. While swirling coolant increased the effectiveness in some cases, it was also

shown to be detrimental in others so additional testing would be needed to find an optimal situation applicable to engine-like conditions.

Bons, MacArthur and Rivir – 1996 [15]

This study investigated the effects of freestream turbulence intensity on the film cooling effectiveness downstream of a single row of jets inclined at 35° to the mainstream. The five cylindrical holes had a diameter of 1.905cm, L/d ratio of 3.5 and were spaced 3 diameters apart. Blowing ratios tested varied from 0.55 to 1.85 with a constant density ratio of 0.95. Freestream turbulence intensities were varied in two ways separately: jet injection from top and bottom upstream of the film holes, and grid turbulence generators. Film effectiveness measurements are conducted using embedded thermocouples downstream of the row of holes and velocity measurements are conducted using hotwire anemometry. The coolant is heated to 20°C above the temperature of the mainstream to create the temperature field. The study showed that high freestream turbulence intensity drastically reduces the FC effectiveness at low and moderate M, but results in higher effectiveness values at high M. This is because the high freestream turbulence reduces the extent of blow-off, and bends the coolant separated from the wall back down raising the effectiveness for x/d $>$ 30. It was also found that high turbulence intensity also dramatically increases the lateral spreading of the jets, resulting in higher effectiveness values between the holes.

Single Row Flowfield Measurements

While film cooling effectiveness and coverage are the end goal of film cooling research, a comprehensive understanding of the flow field and jet structure is also of paramount importance. The flow physics of the jet in cross-flow scenario has deterministic value and improves predictability of flow behavior in certain scenarios such that optimization of turbine cooling design and com-

putational model validation are a very real possibility. Flow measurements are a major part of the present study and therefore the next section outlines some of the past research efforts on this front.

Wright, McCain, and Clemenson − 2011 [16], [17]

Lesley Wright and her research group conducted a flat plate film cooling study investigating the jet structure and film cooling effectiveness using particle image velocimetry and pressure sensitive paint for low and high freestream turbulence intensities of 1.2% - 12.5%. A single row of seven 4.75mm diameter cylindrical film cooling holes were inclined at an angle of 35° to the freestream, had an L/d ratio of 4.66 and a lateral spacing of 4. A separate study involving the same geometry and testing conditions was conducted on fan-shaped holes with a lateral expansion angle of 10°. Blowing ratio cases of 0.5, 1, and 1.5 were tested and three PIV planes were measured: jet centerline, edge of the hole (0.5d), and quarter plane (0.25d). For cylindrical holes, the study clearly showed that a turbulence intensity increase causes the jet to spread over a much larger area for all blowing ratios tested. At low blowing, for both turbulence intensities, the jet remained attached to the surface whereas for high blowing, the jet remained detached. While higher turbulence intensities increased the diffusion of the jets, film cooling effectiveness downstream of injection was still found to be minimal considering that the jets remained detached from the surface. For the fan shaped holes, jet attachment was observed for all blowing ratios tested while maximum velocity of the jet is reduced due to the spreading caused by the geometry. Turbulence intensity increase in the freestream also caused increased spread of the cooling jet. Effectiveness maps showed marginal variation for the wide range of flow conditions due to jet attachment and limited interaction with the mainstream and reduced jet velocity. This indicative of the large advantage that shaped holes have compared to cylindrical holes.

El-Gabry et. al. − 2011 [18]

This research investigates the flow field of flat plate film cooling from a single row of 3 cylindrical holes inclined at 30 degrees to the freestream. Velocity and turbulent quantities are measured in two dimensions using hot wire anemometry with a cross-wire. The holes had a diameter of 1.9cm and a length of 18d. Blowing ratios of 1 and 2 were tested at a constant unit density ratio. The paper presents streamwise and wall normal velocity, rms of the fluctuations, and shear stress contours in streamwise and span-wise oriented planes. Both blowing ratio cases showed obvious jet lift off and the distinct kidney vortex. M = 1 case showed more jet deflection towards the surface but still not completely attached. Velocity fluctuations in the streamwise, wall-normal and span-wise direction were 30%, 25% and 10% of the freestream at the highest blowing ratio and approximately half the magnitude for M = 1. As with other studies, highest magnitude turbulent stresses was observed in the shear layer between jet and freestream on the freestream side and downstream wake side of the jet.

Eberly and Thole − 2014 [19]

Eberly and Thole conducted a flat plate single row investigation for low (1.2) and high (1.6) density ratios documenting film cooling effectiveness downstream of injection as well as time-resolved flow statistics. In addition, blowing ratios in the range of 0.5 2 were also varied giving the study a holistic overview of the geometry configuration. The configuration tested had five 8.2mm diameter holes with a length of 4.7d and a lateral spacing of 6.7d. The paper also conducted a separate cylindrical case for benchmarking and validation of experimental setup compared to past studies in literature. Laser Doppler Velocimetry (LDV) and Time-Resolved Particle Image Velocimetry (TRDPIV) was used to characterize the boundary layer while TRDPIV alone was used for flowfield measurements. Film effectiveness measurements were acquired with the use of an infrared camera. Effectiveness maps as well as velocity, turbulence intensity and vorticity contours for the density ratio and blowing ratio combinations were presented in a very organized

fashion. Notably, the maximum non-dimensionalized streamwise velocity for the high blowing ratio case with a low density ratio was 1.6 in comparison with the high density case which was 1.3. High turbulence levels were found in the exiting cooling jet and in the shear region for the highest blowing ratio and convected far downstream after merging with the high turbulence levels found in the separated region just downstream of injection. The highest turbulence intensity was measured at the highest momentum flux case. It was also found that turbulence intensity measured in the shear layer did not scale with momentum flux ratio as the lowest peak turbulence intensity in the shear layer was observed for the M = 1 case. This was attributed to the fact that the mass flux between the two flows was so similar. An analysis of the vorticity contours showed that the vortical instabilities were spaced approximately one diameter apart and displayed Kelvin-Helmholtz style instabilities near the site of injection. Further downstream at approx. x/d = 4, vorticity was noticed to breakdown into random turbulence.

Bernsdorf, Rose, and Abhari – 2005 [20]

This research paper uses PIV to investigate the flow structure of a jets emanating from a single row of cylindrical holes inclined at 30° and 50°. Density ratios of 1 and 1.5 are also tested by heating the mainstream fluid and cooling the secondary fluid to attain the difference in density ratios. Besides the inclination angle difference, both geometries tested had seven 5mm diameter holes, with L/d of 2.8 and P_z/d of 4. Blowing ratios were also varied between 1, 2, and 2.7 to show the vast differences of velocity and vorticity contours oriented in the span-wise and streamwise direction. Surprisingly, the hole exit angle had a weak effect on the trajectory of the jet and in some cases, the penetration for injection angled at 30° was found to be even higher than that at 50°. Inclination angle was concluded to have a higher effect on trajectory at low momentum flux ratios and the experimental trajectory data collapsed well for momentum flux ratios towards a logarithmic profile. The contours also showed thinning of the incoming boundary layer where

the effects were amplified as blowing ratio, density ratio and hole angle were increased which are expected to increase the mean heat transfer coefficients of the flow.

Multi Row Flowfield Measurements

There exists a plethora of experimental work on single row of film cooling flowfield measurement and visualization. There also exists a substantial amount of heat transfer/ surface effectiveness measurements for single and multi-row studies. Yet, not much effort has been put into capturing the flowfield of multi-row film cooling arrays. Of particular interest is the streamwise and lateral jet-to jet interaction as films progress downstream from their injection site.

Yavuzkurt, Moffat and Kays – 1980 [21]

These researchers used a tri-axial hotwire to measure the 3D flowfield velocities in the full-coverage and recovery region of a film cooling array. The array consisted of 11 staggered rows of alternately nine and eight cylindrical holes with a diameter of 1.03cm and an inclination angle of 30°. Measurements were conducted at a density ratio of 1 and at blowing ratios of 0.4, and 0.9. Since measurements were conducted with a tri-axial probe, all three components of velocity, six Reynolds stresses as well as turbulent kinetic energy (TKE) were obtained. Hotwire measurements were conducted in several different locations: 2.5d downstream of the third row, seventh row, eleventh row as well as 27 and 67 hole diameters downstream in the recovery region. Axial velocity profiles were compared with the 1/7th power law profile for turbulent boundary layers to show the variation downstream of injection. The study also described a dependence of TKE on blowing ratio, more specifically an inverse proportionality of magnitude. High TKE values were observed for low blowing ratios and low TKE values for high M, attributed to the mean velocity gradients between jet and freestream. For low blowing, the energy sink near the wall competes

with high turbulent mixing; for high blowing, the energy sink in the outer layer competes with the entrainment and convection of mainstream fluid toward the wall in the lanes between the jets. The researchers also described the boundary layer in the recovery region as a two layer model: an outer boundary layer and a 2D inner boundary layer that governs the heat transfer.

Abdullah et. al. – 2012 [22]

Abdullah et. al. conducted flat plate surface heat transfer and 3D flowfield measurements on an in-line array of cylindrical holes inclined at 20° using Infrared Thermography and 3D Laser Doppler Velocimetry. Heat transfer measurements were conducted at unit density ratio for blowing ratios 0.5, 1.0, and 2.0 whereas flowfield measurements were only conducted for the latter two. The test array had 20 holes arranged in a 5x4 matrix. Hole diameters for the two types of tests varied while other non-dimensional parameters were kept constant. The heat transfer and aerodynamics test geometries had a hole diameter of 7mm and 10mm respectively, both with an L/d of 3.8, P_z/d of 6 and P_x/d of 10. Results showed that the 20° hole angle provides better cooling effectiveness compared to the commonly used 35° hole angle due to the lower vertical velocity component and minimization of penetration of secondary fluid causing the film to stay attached at higher blowing ratios. Laterally averaged film cooling effectiveness for M = 1 and 2 showed similar film cooling effectiveness values downstream of row three. This was attributed to the fact that the coolant supplied for M = 2 simply caused more spreading which in turn provided wider coverage of the surface downstream of the hole. Film effectiveness at the low blowing ratio case was still higher than both of the high blowing ratios tested.

Jessen, Konopka, and Schroeder – 2011 [23]

The objective of this research was to conduct flow measurements on a multi-row film cooling array in the effects of an adverse pressure gradient flow using 3 component PIV. The array had a

staggered configuration (P_x/d = 6, P_z/d =3) with laid-back fan shaped holes. Each hole had a 10mm cylindrical diameter with = 30°, no compound angle and a length of 24d. The shaped section of the geometry had a lateral diffusion angle of 10° and a forward expansion angle of 8°. Two different injection gases are used to simulate the difference in density ratio (air and CO_2) while blowing ratio is also varied from 0.28 to 0.48. Jessen presents streamwise and span-wise velocity contours, along with mean velocity and U'_{rms} line plots at the hole axis breakout, trailing edge and 2 diameters downstream of the trailing edge. Results showed that turbulence intensities in the upper boundary layer were significantly increased by the injections through the previous rows for zero pressure gradient flow. In an adverse pressure gradient flow, boundary layer growth was significantly enabling jet penetration much deeper into the mainstream. Velocity gradients and turbulence intensities near the wall showed a slight reduction in comparison with the zero pressure gradient flow. A study of the effects of density ratio increase showed higher turbulence intensities in the shear layer for CO_2 injection which would promote mixing and thus potentially reduce film cooling efficiency.

Natsui – 2015 [24]

The current study supplements the data and analysis acquired by Natsui's dissertation. Two of the geometries tested by Natsui have been used for the current study for flow visualization and direct comparisons can be drawn to validate the dataset as well as show effectiveness correlations. Natsui presented a thorough film cooling effectiveness study using pressure sensitive paint and CO_2 coolant injection on cylindrical and laterally diffused shaped geometries of two different spacings. Particle image velocimetry was conducted on the cylindrical geometry that will be used in the present study to show repeatability of test conditions. Hotwire anemometry was used in this study to show velocity, U'_{rms}, and lengthscale line plots at discrete locations above the array however for only 2 blowing ratios. Considering the experimental setup, and geometries are identical,

aspects of Natsui's work will be presented in this publication for ease of access and reference.

Motivation, Objective and Novelty of Study

In order to raise gas turbine specific work outputs, there exists a need to continually improve upon the material selection, effectiveness of thermal barrier coatings, and cooling technologies. High fidelity measurements of heat transfer as well as the fluid dynamics involved provides a strong framework for research in this field. Building a diverse set of experimental data also helps develop and validate computational models thus giving users the ability to optimize cooling designs with a certain degree of predictability and accuracy.

This study has four different objectives:

1. To quantitatively compare film cooling flow statistics of multi-row film cooling arrays using 1-D hotwire anemometry at a range of blowing ratios.
2. To analyze the similarities and differences of boundary layer characteristics at set locations downstream of holes in the centerline plane.
3. To compare the flowfield emanating from an array of laterally diffused film cooling holes vs. cylindrical holes with identical spacing, inclination angle, boundary layer conditions, and blowing ratios in the range of 0.5 1.2.
4. To make comparisons of the flowfield measurements to the film cooling surface effectiveness measurements carried out by Natsui.
5. To provide a strong base for CFD validation and computational model development

The current work also has many novel aspects to it.

1. To improve the available database of flowfield measurements of shallow inclination angle (20°) film cooling geometries.

2. To improve the available database of flowfield measurements of staggered multi-row film cooling arrays. There are very few studies published on multi-row film cooling flow fields.

3. A comparison at set locations downstream of each streamwise jet in the centerline plane of the multi-row array. Since multi-row flow-field studies are not conducted very often, this aspect to the study adds value for CFD validation as well as future learning of the behavior of boundary layers with multiple rows of coolant injection.

4. A quantitative comparison of flow statistics of film cooling flows emanating from cylindrical and diffuser shaped arrays. Usually either single hole or single row studies are conducted and very few studies touch upon the jet to jet interaction. It is even more rare to find diffuser shaped flow field statistics in literature.

5. To suggested an explanation of the trends in surface effectiveness measurements based on flowfield statistics even though density ratios of the two different studies vary.

CHAPTER 3: RESEARCH DESIGN

This section describes the facility that was used for experimental film cooling testing. The wind tunnel layout is first presented in detail, then a thorough description of the geometries tested upon.

Wind Tunnel Layout

The low speed wind tunnel used for experimental film cooling data acquisition has previously been described by Natsui [24] and some of the details are repeated in this section. The wind tunnel is constructed in a modular fashion allowing a range of experiments to be conducted with fast turn-around time between experiments. Surface heat transfer measurements using pressure sensitive paint, thermal flowfield measurements using laser induced fluorescence, and flowfield velocimetry using particle image velocimetry and hotwire anemometry is all possible.

The wind tunnel is comprised of four distinct parts: main-flow conditioning, test section, exit diffuser, and secondary flow plenum. The mainstream flow is forced in an open-loop blow-down type wind tunnel by a 3000 L/s, 15kW blower. A secondary 2.2kW suction fan is used to remove air from a boundary layer bleed 67.5d upstream of the first row of holes. The leading edge of the boundary layer bleed is 3mm thick. The mainstream flow is conditioned with honeycomb and a series of mesh screens before entering an acrylic 1-D contraction which contracts the flow in the direction of the test section height. Figure 3.1 below shows a cross-sectional view of the wind tunnel with contraction, boundary layer bleed, plenum, test section, and test plate mounted in the flow.

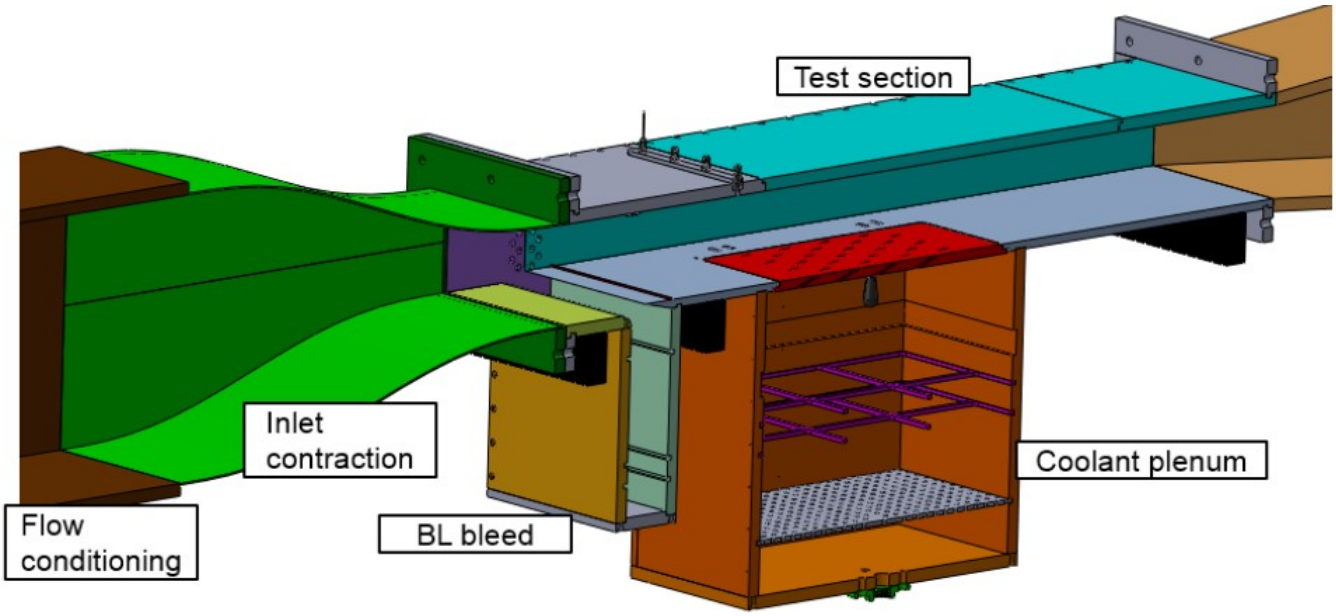

Figure 3.1: Isometric cross-sectional view of wind tunnel layout [24]

A rigid frame was constructed using 15 series 80-20 aluminum extrusions atop which the entire rig was mounted. The contraction section is flanged to a constant area duct comprised of the test section. The test section is then flanged to an exit diffuser section that ducts the air out of the room. The test section has a cross section of 21 x 6. The top and side walls are made of acrylic while the bottom wall of the test section is made of aluminum. The top and one side wall is left clear for optical access when conducting experiments such as PIV, PSP, or LIF. The rest of the test section is painted black including the actual test geometries to reduce the scatter of laser light and reduce stray reflections from surfaces. The test section bottom wall has a large rectangular hole cut out where the test geometry is installed. The top wall of the test section is build modular and can be changed to accommodate the different testing techniques. For PIV and PSP, a clear acrylic top wall is installed for laser access and or camera viewing. For hotwire testing, the top wall is switched out for one with a slot. A 2D traverse is mounted to this plate allowing the hotwire probe

to be traversed through the slot and into the channel for flow velocity measurements. The test section side wall that is painted black contains pressure taps equidistantly spaced to measure static pressure drop along the test section. While these measurements were not conducted for this set of tests, the pressure measurements were previously taken and can be seen in [24].

Secondary Flow

Secondary flow is supplied by an air compressor and is ducted to a venturi where the differential pressure, static pressure and temperature is measured. The facility allows easy switching between the air compressor and a CO_2 microbulk for different density fluid testing. The current study only uses air at a density ratio of approximately 1. A flow regulator far upstream of the throat is used to adjust the coolant mass flow rate to the system. After passing the venturi, the air is ducted to a plenum which comprises of 1in. thick acrylic walls, a splash plate, honeycomb, and fine wire mesh screens to ensure that the secondary flow is uniformly distributed through the film cooling holes. The plenum is installed on the bottom side of the test section forcing air to be injected through the film cooling holes.

The venturi, and plenum are fitted with T-type thermocouples to measure the temperature of the secondary flow as it passes through the system to the film cooling holes. Static pressure taps are located along the plenum to ensure that the plenum is acting as a true plenum space. Plenum pressure and temperature measurements are used for density calculations of the coolant just prior to injection. Upstream of injection, four sheathed T-type thermocouples, and three pitot probes are used to measure the freestream temperature and total pressure. This temperature, along with the static pressure, measured on the side-wall, at the same streamwise location is used to calculate the freestream fluid density. The thermocouples and total pressure ports are positioned in the middle of the channel, ensuring that they do not interfere with the fluid dynamics of the boundary layer

developing on the bottom surface. Figure 3.2 below shows the plenum setup along with freestream measurement locations while Figure 3.3 shows the test section setup with reference to the first row of holes.

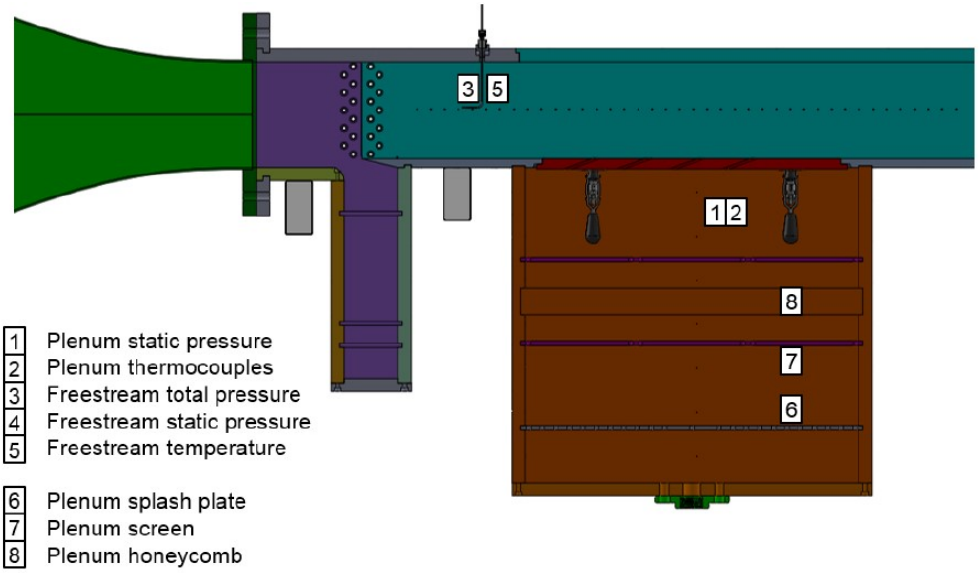

Figure 3.2: Cross-sectional view of test section and plenum [24]

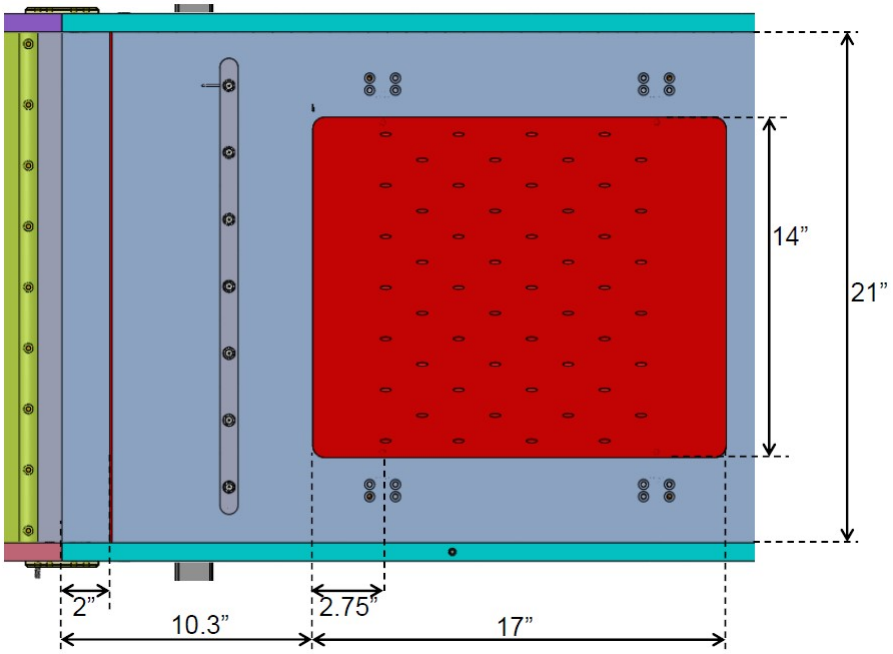

Figure 3.3: Top view of test section with sample test specimen installed [24]

Incoming Boundary Layer

As with all film cooling studies, the incoming boundary layer is of high importance as it defines the primary flow condition and determines its impact on the emanating jets. The boundary layer profile is measured at 4d upstream of the first row trailing edge for each test. The parameters describing the boundary layer are summarized in Table 3.1 below. The boundary layer profile is plotted in Figures 3.4 and 3.5 using inner and outer wall coordinates respectively.

Table 3.1: Incoming Boundary Layer Characteristics

Characteristic	Value	Units
Freestream Velocity, U_∞	40	m/s
Boundary Layer Thickness, δ_{99}	6.36	mm
Displacement Thickness, δ_1	0.79	mm
Momentum Thickness, δ_2	0.62	mm
Shape Factor, H	1.27	-
Reynolds number on δ_2, $Re_{\delta 2}$	1.59k	-
Reynolds number on d, Re_d	9.78k	-
Freestream Turbulence Intensity, TI	3.57%	-
Non-dimensionalized BL thickness, δ_{99}/d	1.67	-
Non-dimensionalized Displacement thickness, δ_1/d	0.21	-
Non-dimensionalized Momentum thickness, δ_2/d	0.16	-

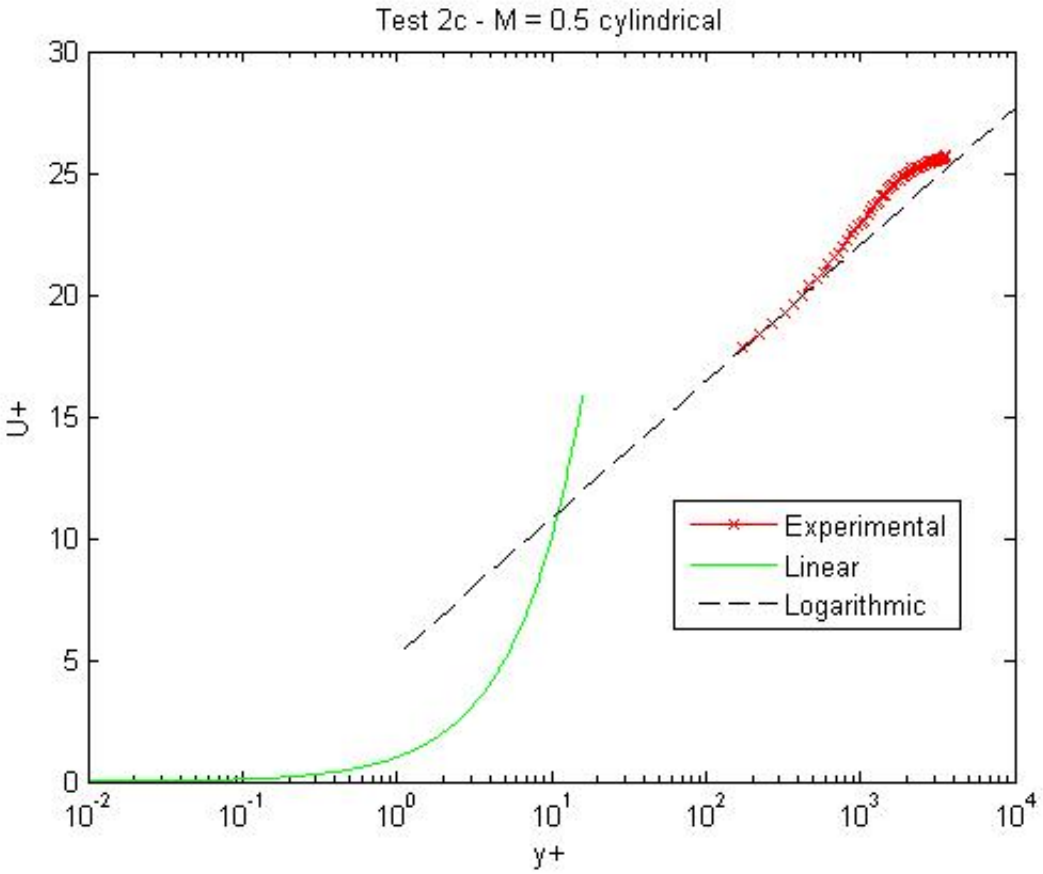

Figure 3.4: Boundary layer in inner wall coordinates

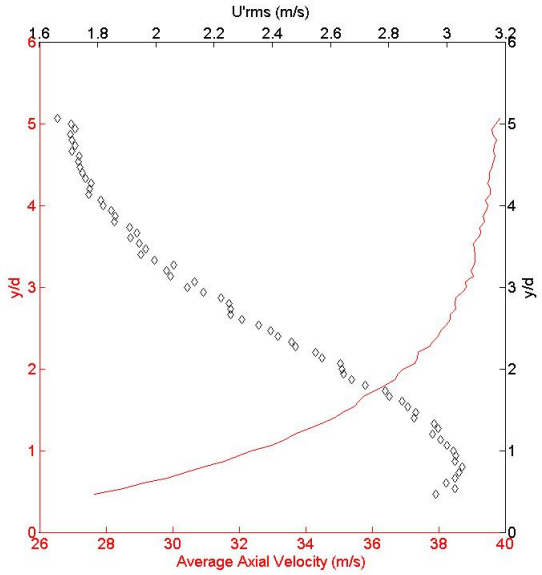

Figure 3.5: Boundary Layer Profile in outer wall coordinates

Test Geometries

For this particular study, two different geometries were tested upon. The first geometry is a staggered array of cylindrical holes while the second geometry is a staggered array of cylindrical holes with laterally diffused exits. The geometry with cylindrical holes is machined out of aluminum and the diffuser geometry is 3D printed via stereolithography (SLA). While shaped holes have become the industry norm for film cooling, cylindrical hole configurations have a certain degree of simplicity and a strong conglomeration of comparable data in literature (heat transfer and fluid dynamics) for comparison to other studies. In addition, it also serves as a good baseline for computational fluid dynamics validation and model development.

Each test geometry has 8 rows, of alternating 7 then 6 holes, with an inclination angle of 20°. The arrays have nominal spacings of P_x/d and P_z/d of 7.5. The holes have an L/d of 11.2 which correspond to a test plate thickness of 3.84d. The diffuser shaped film cooling holes in the present study are modeled after the fan-shaped hole studied by Gritsch et. al. with slight variation of certain parameters. These variations are described in Table 1 below. Figure 5 below also shows a representation of the diffuser shaped hole geometry used in the present study.

Table 3.2: Diffuser shaped hole parameters

Parameter	Symbol	Gritsch et. al. [6]	Present Study
Inclination Angle (°)	α	30	20
Hole Diameter (mils)	d	400	150
Total Hole Length	L/d	6	11.2
Plunge depth	L_p	4	4
Lateral Expansion Angles (°)	$\Phi_{1,2}$	14	14
Layback Angle	Φ_3	0	0
Area Ratio	AR	3	2.66
Fillet Radius	r_f	0	1

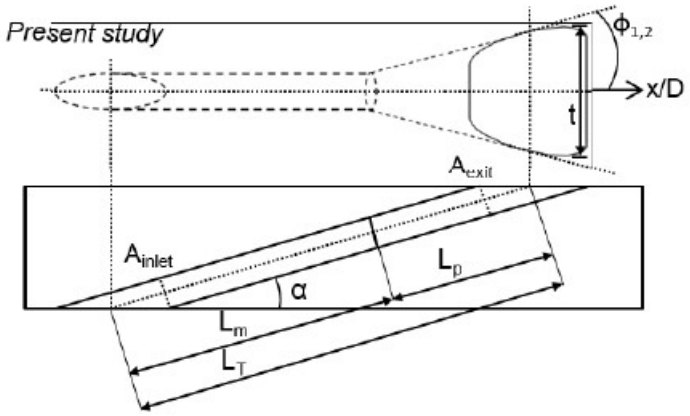

Figure 3.6: Diffuser Hole Geometry [24]

CHAPTER 4: HOTWIRE ANEMOMETRY

The following chapter provides detail on the experimental procedure of the hydrodynamic measurements conducted. A brief discussion of the hotwire anemometry mechanics is presented followed by details about the equipment used, probe calibrations conducted, convergence studies and probe wall-normal position estimation.

Background

The hotwire sensor is essentially a cylindrical heating element in crossflow. The crossflow impacting the hot cylinder extracts heat primarily via convective heat transfer. The temperature of the wire is kept constant by means of a regulating switch and hence the fluctuating current is a function of the velocity and temperature of the impacting airstream. Advantages of hotwire anemometry include its high temporal and spatial resolution, particularly in the near-wall region. Unfortunately, it can only sample at a single location in the flowfield at any given instance in time hence resolving the entire flowfield is extremely inefficient.

Heat Transfer

Energy balance of a steady state cylinder heating element in crossflow can be expressed by

$$i^2 R = hA(T_w - T_\infty) \tag{4.1}$$

Substituting Nusselt number for the fluid heat transfer coefficient,

$$i^2R = \frac{ANuk_f}{d}(T_w - T_\infty) \tag{4.2}$$

In the forced convection regime,

$$Nu = A_1 + B_1Re^n = A_2 + B_2U^n \tag{4.3}$$

where

$$Re = \frac{\rho U d}{\mu} \tag{4.4}$$

Substituting and simplifying,

$$i^2R^2 = E^2 = (T_w - T_0)(A + BU^n) \tag{4.5}$$

This can be further simplified to

$$E^2 = \alpha + \beta U^n \tag{4.6}$$

This relation is known as Kings Law and provides a curve fit for voltage to velocity conversion. Unfortunately, this relation is only theoretical and deviates from this ideal model requiring an experimental calibration to be conducted. The voltage measured to actual velocity transfer function can be derived however a fourth order polynomial curve fit is found to work better for experimental measurements.

Wheatstone Bridge Circuit

The wheatstone bridge comprises of the hot wire sensor on one arm, placed opposite a variable resistor which defines the operating resistance and temperature of the wire. As flow velocity is increased, the wire resistance will decrease causing a voltage difference across the diagonal and an error voltage at the input of the servo amplifier. Acknowledging the error, the probe current is increased to compensate for the heat loss from the wire, thus keeping the temperature constant. As a result of the high gain of the current regulating servo amplifier, the wire time constant is reduced on the order of microseconds.

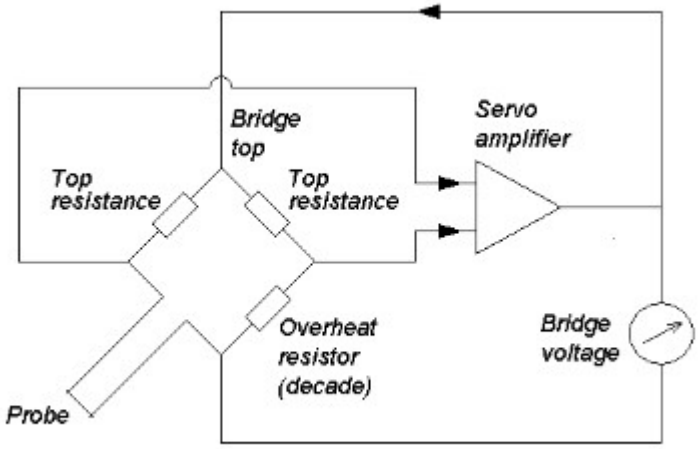

Figure 4.1: Wheatstone Bridge Circuit [29]

Hardware

The hotwire sensor used for these experiments is a Dantec single-wire miniature hotwire probe (model 55P11) with wire diameter and length of 5m and 1.25mm respectively. The probe is mounted to a 2D traverse providing movement in the x and y directions with 0.125m and 0.5m

resolution respectively. A Dantec Streamline Pro Anemometer controls the hotwire sensor and is connected to an A/D converter and the signal is then digitized using a PXIE-6366 DAQ card mounted on a PXIE-1062Q chassis. The motion controllers that control the traverses are also connected to the chassis.

Frequency Response

The frequency response of the Dantec 55P11 probe/CTA system is optimized by applying a square wave signal to the bridge top. A filter for the pre-amplified bridge unbalance signal of 8 was applied to reduce the baseline oscillations. In addition, a gain of the servo loop amplifier of 14 is applied to obtain the bandwidth of the system. The bandwidth can be calculated as the ratio 1/1.3t and corresponds to a single order system with only one pole or time constant [25]. For the maximum velocity of approximately 82m/s, the optimized servo-loop bandwidth was found to be approx. 69.930kHz. This allows for a sampling frequency of about 140kHz while filtering the signal at 70kHz.

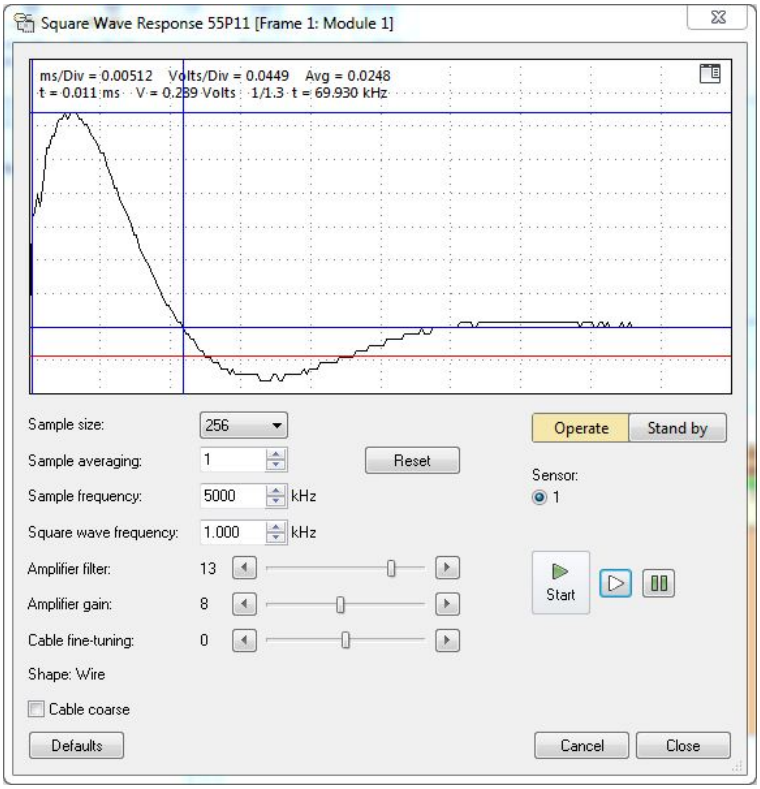

Figure 4.2: Square Wave Test at 82m/s

Calibration

A hotwire sensor is calibrated using a TSI Model 1127 manual velocity calibrator. The calibrator consists of a controllable jet orifice with a 10mm diameter exit nozzle, designed for velocities in the range of 3-150m/s, which provides steady, well-conditioned flow to the sensor that is mounted in the potential core of the jet. The probe support resistance, BNC cable and sensor prongs are measured using a shorting probe and subtracted from the actual resistance of the sensor. The calibration is conducted for flow velocity within the range of 7-80 m/s. The offset and gain are adjusted to ensure the min and max flow rates are well distributed over a range of -5 and 5 volts. Flow rate through the jet orifice is varied taking twenty voltage readings between -3.6 and 3.6

volts spaced approximately 0.36 volts apart and the corresponding differential pressure is recorded manually. 60,000 samples are obtained at a sampling frequency of 60 kHz for each flow rate through the calibrator. Chamber and ambient temperature are also recorded for each of the 26 data points. Jet velocities are calculated using the differential pressure between the chamber and room, along with stagnation temperature, absolute pressure and air properties [26]. A relation between measured bridge voltage and flow velocity can then be derived using a fourth order polynomial curve fit.

Sampling Convergence

A convergence study is conducted prior to data collection ensuring that the fluid turbulent characteristics are being captured accurately. In order to conduct the sampling convergence, it is important to have an estimate for the turbulent timescales of interest. The Kolmogorov length scales can be estimated according to equation 4.7 [27].

$$\eta = (\frac{\nu^3 L_c}{U^3})^{1/4} \tag{4.7}$$

This produces an η estimate of 9.52 μm. Dividing by the convective velocity of the flowfield yields a timescale of 0.238 μs.

A reasonable estimate for the ratio of integral time scales to kolmogorov time scales can be given by equation 4.8

$$\frac{t_L}{t_\eta} = (\frac{U L_c}{\nu})^{1/2} \tag{4.8}$$

Using the channel height as the characteristic length, freestream velocity as the convective velocity, and ν of 15.11×10^{-6}, the ratio calculated is 635.17. Multiplying this ratio now by the Kolmogorov time scale gives an estimate for the time scale of the largest possible eddy in the flowfield, 3.81 ms. Since this study is geared more towards momentum transport within the boundary layer, the sampling frequency required is not as high as that for measuring scales on the lower end of the spectrum.

A sampling convergence study can now be conducted with the knowledge of the max and min timescales of the flowfield. A vertical pull at the trailing edge of the first row of holes is obtained to determine the vertical location of highest turbulence level at a blowing ratio of 0.5. This vertical location is then sampled at varying frequencies (2 kHz to 200kHz) for 10s. A sampling frequency of 60 kHz is chosen for data acquisition to improve temporal resolution and to maximize the size range of eddies that can be captured. Sampling Convergence is conducted for the 60kHz, 10s velocity measurements to determine the number of samples required for convergence of the mean, and standard deviation for a statistically stationary measurement of the flow field. The signal is filtered at 30kHz using a fourth order butterworth filter through Streamware Pro.

For this study the highest turbulence level at a blowing ratio of 0.5 was recorded to be 3.2921 at location 9 as shown in Figure 4.3 below. Figures 4.4 and 4.5 displays the convergence of mean velocity and turbulence level at location 9 after approximately 300 thousand samples

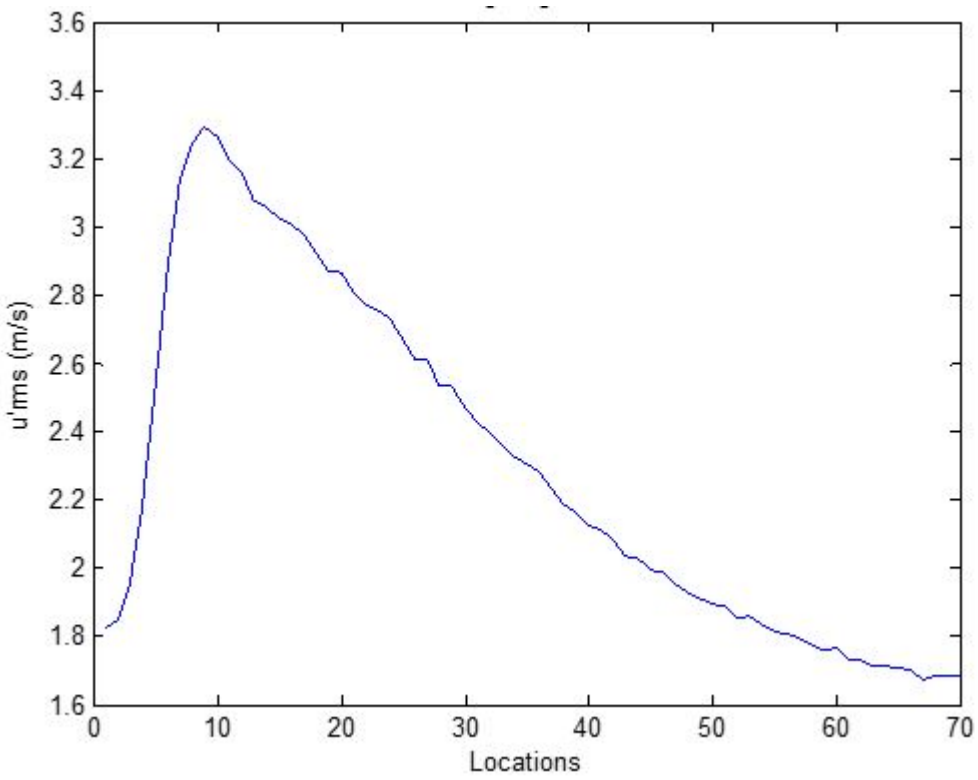

Figure 4.3: Vertical Pull at Trailing Edge of first hole - M = 0.5

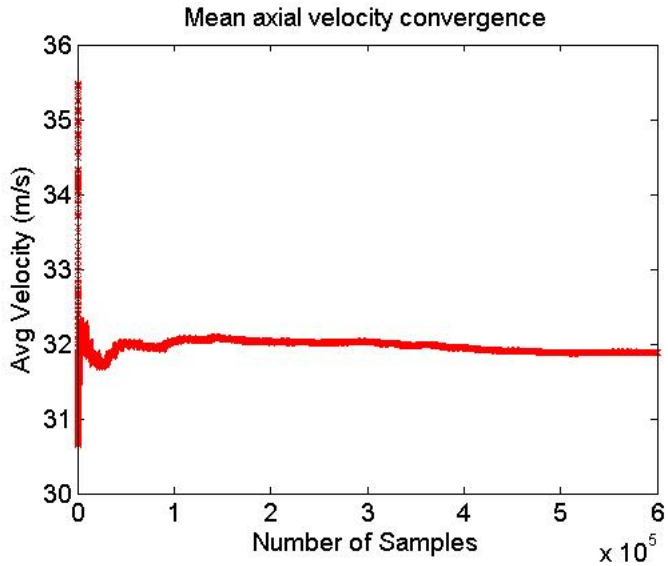

Figure 4.4: Sampling convergence of mean velocity (m/s)

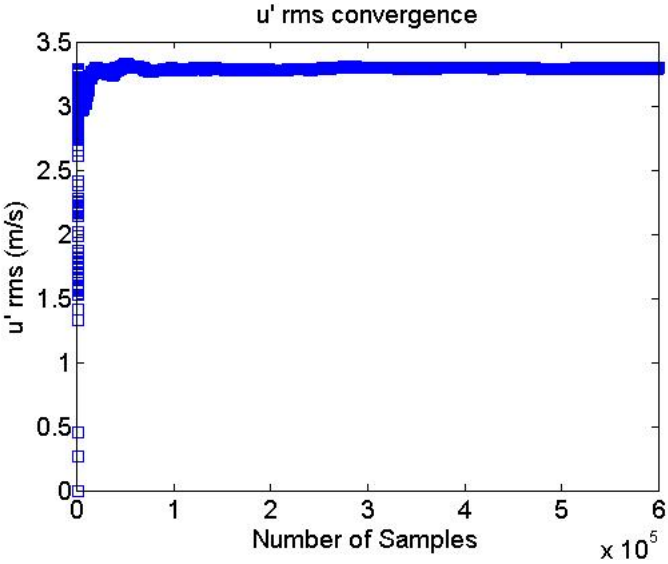

Figure 4.5: Sampling convergence of u'_{rms} (m/s)

Data Collection

The hotwire sensor is traversed to 13 horizontal locations which include 12 locations spaced 5d from the global zero and 1 location upstream of the first row of holes (-4d from global zero). The 12 testing locations are displayed in Figure 4.7 below and the physical distance from the global zero can be seen in Table 4.1 below. At each of the 13 horizontal locations, the sensor was traversed vertically to 70 discrete locations with a spacing of approx. 0.07d. The number of vertical locations were chosen after sampling the highest blowing ratio case for cylindrical geometry ensuring that the entire flowfield was captured at the furthest location downstream. Data is collected by interfacing Dantec software, StreamWare Pro, for anemometry and NI automation software for traversing via a LabView code and printed to 910 text files of raw voltages for each case of the test matrix.

The text files are then imported into Matlab where the raw voltages are converted to velocities using the fourth order polynomial curve fit obtained from calibration and statistical quantities such as mean velocity, u'_{rms}, turbulence intensity and integral length scale for each vertical location are obtained.

The velocity obtained from single wire hotwire anemometry is a function of velocity magnitude and direction of the incoming flow. The effective velocity measured by the probe can be given by Jorgensen's Equation [29] where k and h and sensitivity factors for the tangential and bi-normal contributions. For a probe L/d = 250, k and h are approximated to be 0.2, and 1.05 respectively. Ideally the values for k and h are 0 and 1 respectively. Figure 4.6 below shows the normal, bi-normal and tangential coordinates as X, Y, and Z respectively.

$$U_{eff} = F(U, \alpha, \beta) \tag{4.9}$$

$$U_{eff}^2 = U_N^2 + k^2 U_T^2 + h^2 U_B^2 \tag{4.10}$$

Table 4.1: Hotwire Testing Locations

Location	**x/d Location**
0	-4
1	0
2	5
3	10
4	15
5	20
6	25
7	30
8	35
9	40
10	45
11	50
12	55

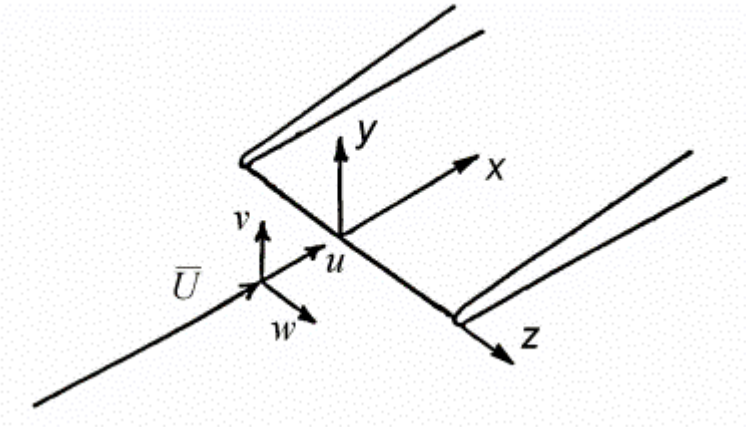

Figure 4.6: Coordinate system of the probe

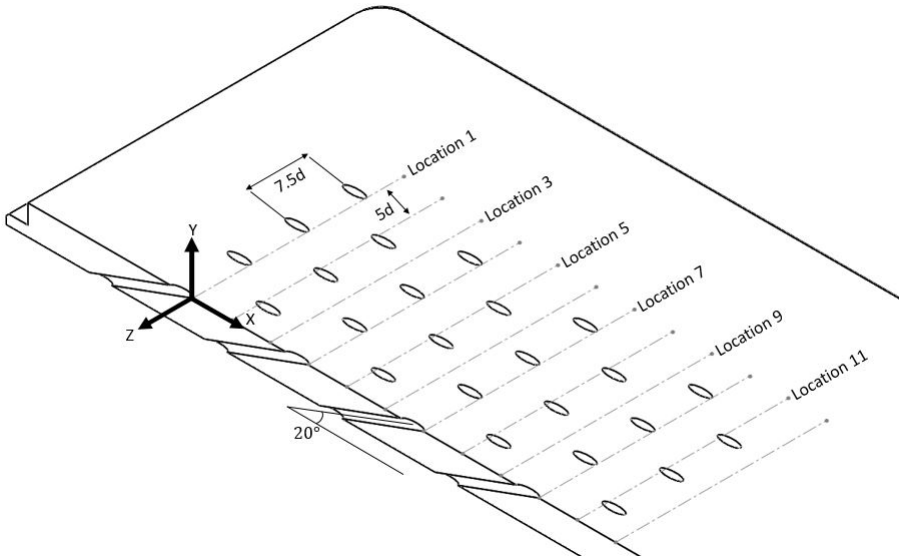

Figure 4.7: Testing Locations for Hotwire Anemometry

Wall Normal Probe Position

Determining the actual position of the probe with relation to the wall is unrealizable through experimental measurement techniques. As a result, it becomes necessary to use a type of fit for flat plate studies that would estimate the true distance from the wall. A velocity scale for the inner region of a boundary layer can be given by the friction velocity as seen in 4.11 where $\tau_{y=0}$ is the wall shear stress and ρ is the density of the fluid.

$$u^* = u_\tau = \sqrt{\frac{\tau_{y=0}}{\rho}} \tag{4.11}$$

Using u_τ, non-dimensional wall coordinates for wall normal distance and velocity can be defined according to 4.12 and 4.13 where ν is the molecular diffusivity.

$$y^+ = \frac{y u_\tau}{\nu} \tag{4.12}$$

$$u^+ = \frac{u}{u_\tau} \tag{4.13}$$

Different descriptions of boundary layer regions at the wall have been defined in literature to describe wall bounded flows. In the region at $y+ < 3$, intermolecular stresses dominate the fluid dynamics giving a linear relationship between u^+ and y^+. A little further away yet still within the near wall region, the intermolecular stresses become negligible and turbulent stresses tend to dominate resulting in a logarithmic profile given by 4.14 where κ is the von Karman constant (0.41) and C is an additive constant assumed to be 5.2 for this study.

$$u^+ = \frac{1}{\kappa} ln(y^+) + C \tag{4.14}$$

The van Driest damping function, Coles wake function and Modified wake functions are some of the other descriptions of the fluid dynamics of boundary layers in the near wall region but are not used in this study. Figure 4.8 below shows the different descriptions of the near wall boundary layer.

To determine the position of the probe above the film cooling surface, the wall shear stress $\tau_{y=0}$ and offset from the wall is initially guessed and calculated values of u^+ are compared to that of the logarithmic u^+ profile. This process is done for an array of $\tau_{y=0}$ and $y_o f f set$ to get the best match of slope and position on the graph of the logarithmic profile. Figure 4.9 below displays an example of the experimental data in comparison with the logarithmic profile for a particular $\tau_{y=0}$ and $y_o f f set$ combination. Since a 2D traverse is used, assuming the film cooling plate deformation and angle of the traverse with respect to the freestream is minimal, the vertical offset from the wall can be estimated as that found at the upstream location.

Figures 4.10 and 4.11 demonstrate the effects of varying the shear velocity and the wall normal offset respectively. Both are iterated simultaneously to obtain the best fit compared with the logarithmic law of the wall. Percentage differences between the two profiles in the ”linear” section of the curve were maintained below 0.5% for each of the tests. Figure 4.12 below is shown below as an example of the fit together with the uncertainties.

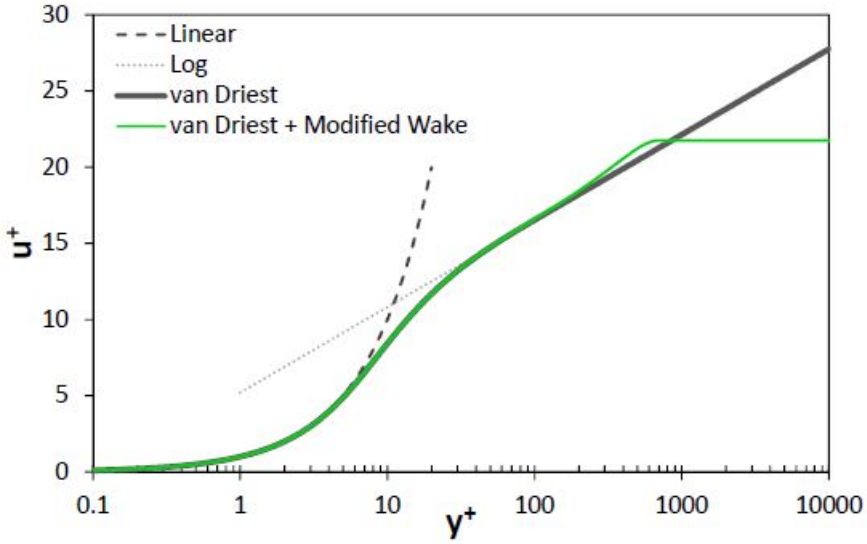

Figure 4.8: Near Wall Boundary Layer [24]

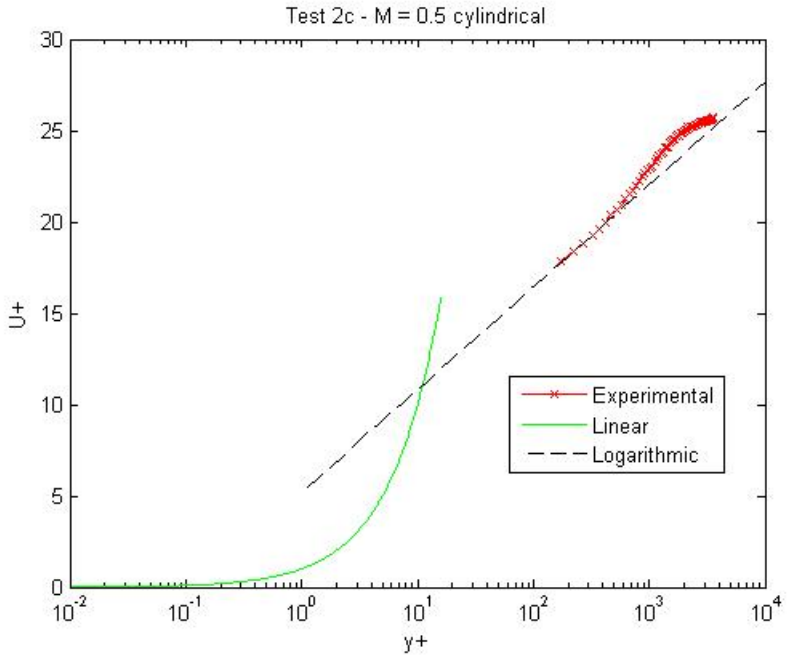

Figure 4.9: Experimental boundary layer compared with log law

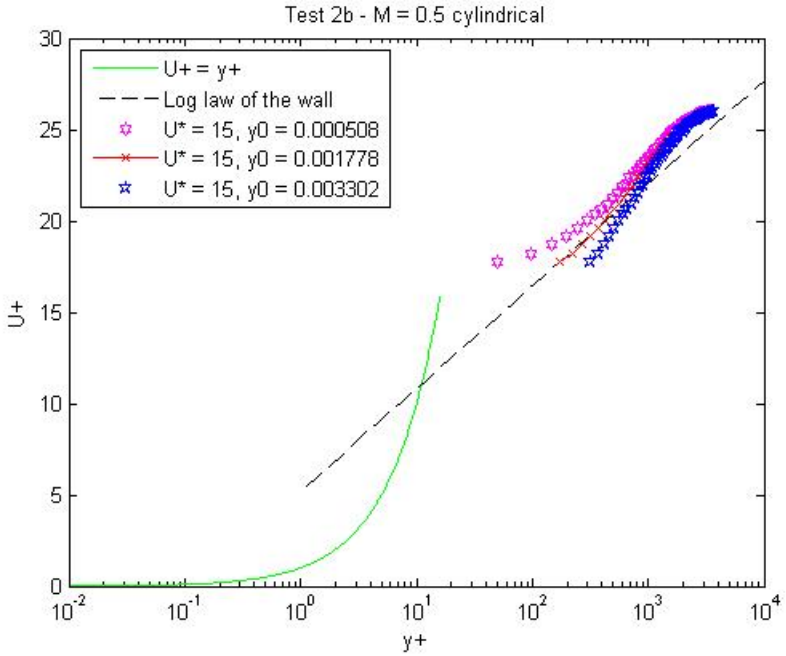

Figure 4.10: Iteration process for wall normal offset from surface

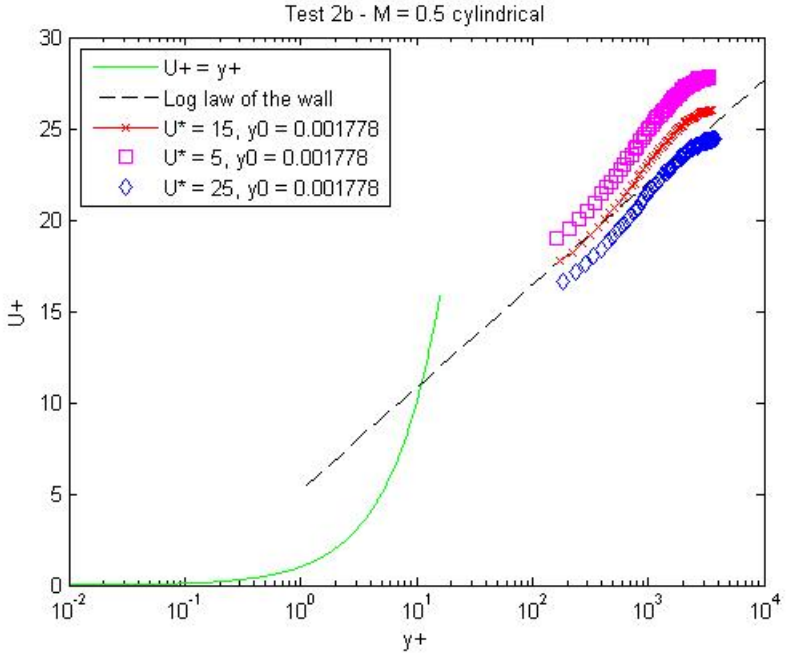

Figure 4.11: Iteration process for friction velocity

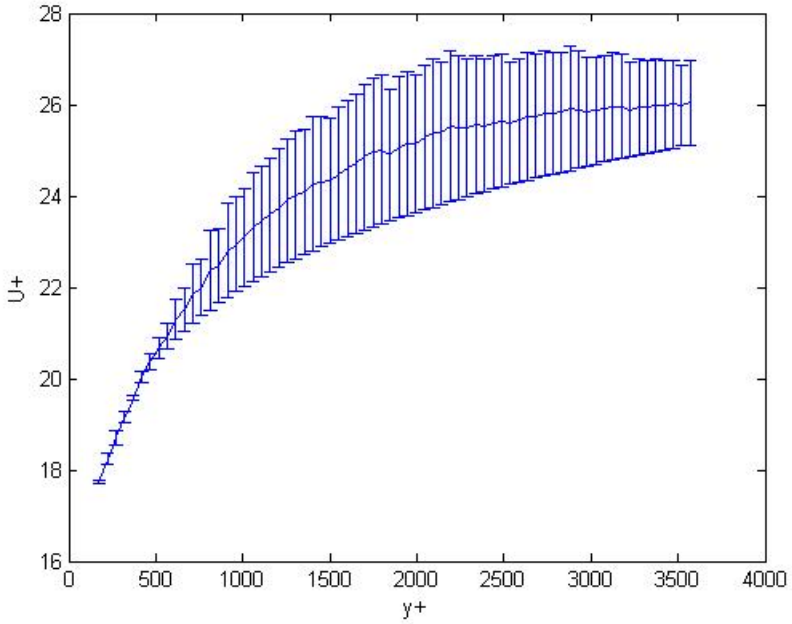

Figure 4.12: Percent Deviation of experimental measurement from log law of the wall, M = 0.5

CHAPTER 5: FINDINGS

The following section presents the results of the hydrodynamic measurements conducted on the multi-row film cooling arrays. The results are broken down into blowing ratio effects on the film cooled boundary layer for both geometries, peak analysis of jet cores and shear layers, and displacement/momentum thickness analysis. Finally, the results are used to suggest effects on surface coverage by comparing results of a previous study on film cooling effectiveness by Natsui where a density ratio of 1.5 was used. As with all scientific experimental work, the boundary layer profiles at M = 0.3 have been compared to that measured by Natsui [24] to validate the dataset and give leverage for predictions of film cooling surface coverage. The baseline case of M = 0.5 was also used for a repeatability study to show precision in measurements and predictive agreement in the dataset. Table 5.1 below displays the tests conducted for cylindrical and diffuser shaped geometries. For ease of reference, the blowing ratios are referred to as the blowing ratios proposed rather than the actual blowing ratios tested throughout this document.

Table 5.1: Hotwire Test Matrix

	M	I	DR	VR	Test #
Cylindrical	0.31	0.10	1.01	0.31	1
	0.49	0.24	1.01	0.49	2
	0.68	0.46	1.02	0.67	3
	0.98	0.93	1.03	0.95	4
	1.17	1.32	1.04	1.13	5
Cylindrical	0.48	0.23	1.01	0.48	2b
	0.49	0.24	1.01	0.48	2c
Diffuser	0.49	0.24	1.01	0.49	6
	0.68	0.46	1.01	0.67	7
	0.98	0.94	1.02	0.96	8
	1.16	1.33	1.02	1.14	9
	1.47	2.07	1.04	1.41	10

Uncertainty

Uncertainty of blowing ratios, calculated using standards documented in ASME 19.1 Test Uncertainty [22], is estimated to be $\pm$ 0.01. This accounts for bias and precision of all measurands and results calculated from those measurands.

Relative expanded uncertainties on a single velocity sample obtained via hotwire anemometry gives the data a maximum total uncertainty of 4.63%. This uncertainty is based on the ISO uncertainty model combining relative standard uncertainties of each input variable into a total uncertainty at a 95% confidence level with a coverage factor of k = 2 [23]. Error sources include a calibrator uncertainty of about 1%, linearisation uncertainty of about 0.928%, along with other contributions from A/D board resolution, ambient temperature variations from calibration to testing, and ambient pressure variation. Typical values along with a concise way to calculate the uncertainties is provided in the Dantec Manual [29].

Variations in temperature cause approximately 2% of error in hotwire measurements per degree Kelvin [23]. To mitigate this issue, calibrations were conducted before and after each test and time between calibration and testing was kept to a minimum. Maximum temperature variation from the calibration temperature was recorded to be 1.7$\circ$C. Probe positioning and humidity variants were neglected in this uncertainty analysis. The uncertainty diagram illustrated in Figure 5.1 below shows the contributions to the uncertainty of a velocity sample and the wall normal position, y of a measurement.

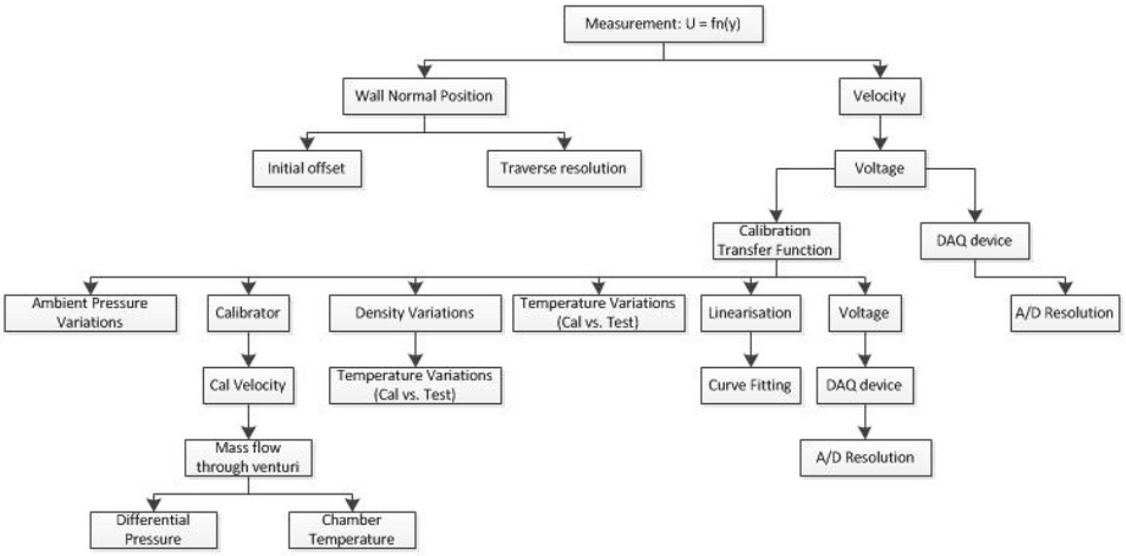

Figure 5.1: Uncertainty diagram for a velocity sample obtained with single-wire hotwire anemometry

Validation

To validate the dataset, the present study is compared with that obtained by Thole et. al. [11]. While the graphs show quite large discrepancies, it is important to note that Thole et. al. provided data at 2 diameters downstream of the trailing edge whereas the closest point measured in the present study is 5d downstream of the first hole. The discrepancies are also attributed to varying flow conditions such as the lower turbulence intensity, boundary layer thickness, etc. The differences in parameters are summarized in Table 5.2 below. In general however, the order of magnitudes are similar for both tests and do show agreeable trends to display the jet potential cores, shear layers, etc. Figures 5.2 and 5.3 below displays the mean velocity and turbulence level

of the two studies. The maximum uncertainty in the test is also displayed on the figure.

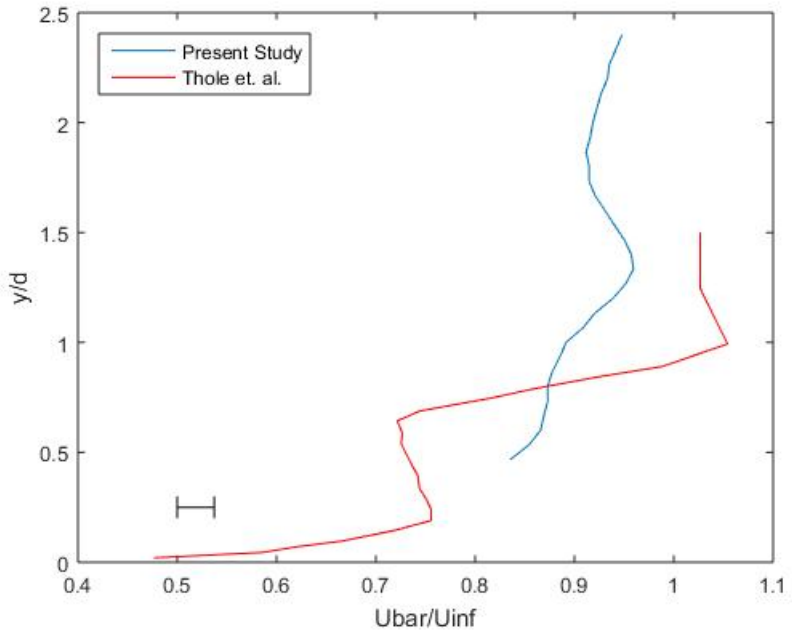

Figure 5.2: Validation of mean velocity dataset compared with Thole et. al. [11], M = 1

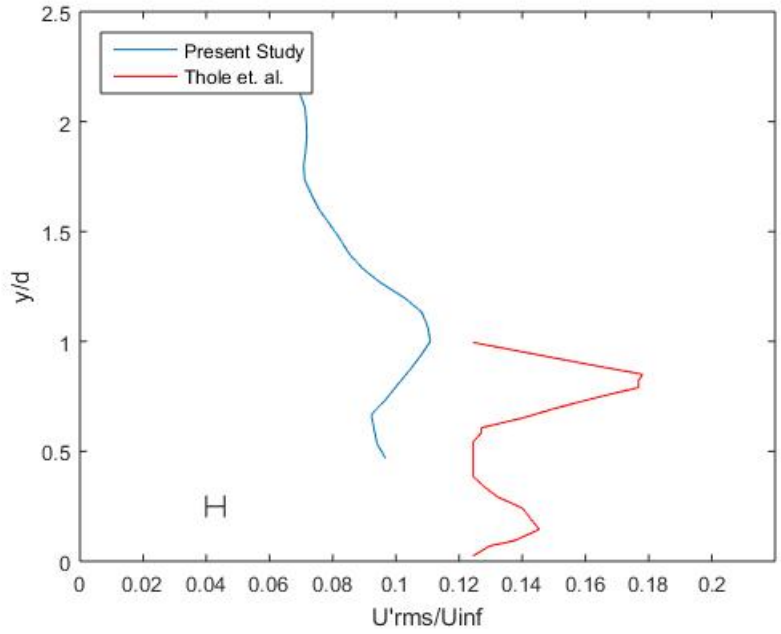

Figure 5.3: Validation of turbulence level dataset compared with Thole et. al. [11], M = 1

Table 5.2: Comparison of Thole et. al. and present study parameters

Parameter	Thole et. al.	Present Study
Measurement Location from TE	X/d = 2	X/d = 5
L/d	6	11.2
α	30 °	20 °
Freestream Velocity (m/s)	85	40
Metering Hole Diameter (mm)	10	3.81
Boundary Layer Thickness, δ_{99}/d	0.8 at X/d = -3 from TE	1.67 at X/d = -4 from TE
Reynolds number on δ_2, $Re_{\delta 2}$	3.8k at X/d = -3 from TE	2.76k at X/d = -4 from TE
Freestream Turbulence Intensity, TI	1.5%	3.57%

To appropriately draw comparisons between the flowfield and film cooling effectiveness

measurements by Natsui it is necessary for the two flowfields to have the same magnitudes and boundary layer shape. Multi-row film cooling boundary layer was measured at M = 0.3 at the trailing edge of each jet in the array centerline. The comparison can then be made between the experimental data and that obtained by Natsui. Figure 5.4 below displays the average velocity measured at the array centerline and hole trailing edge of rows 1, 3, 5 and 7. While minor discrepancies are apparent, the plot shows excellent agreement overall and are within the uncertainty bounds calculated.

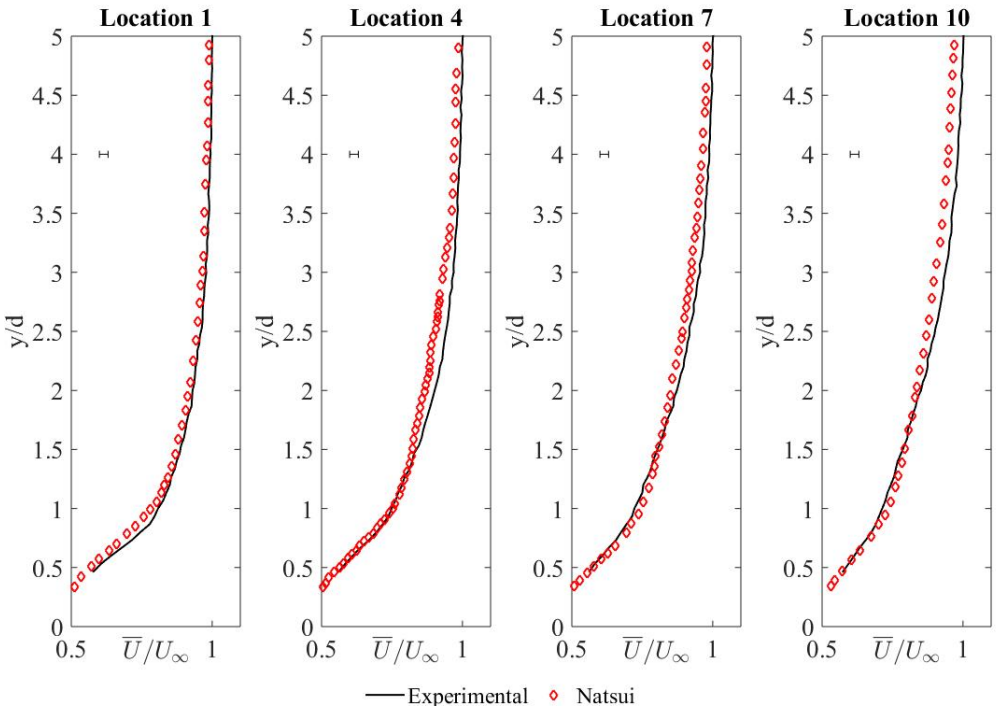

Figure 5.4: Experimental results in comparison with Natsui [24] at M = 0.3

Repeatability

In order to demonstrate precision of measurement, a test case was repeated on three different days with consistent procedure. The three datasets are then processed as described in the procedure

and are plotted in Figures 5.5 through 5.8 below displaying average velocity, turbulence level, and turbulence intensity. At this blowing ratio, the onset of the mixing regime is observed as the jets lift off the surface momentarily and re-attach by 10d downstream. This phenomena can be visually seen 5d downstream of rows 3, 5, and 7 (locations 5, 8, and 11) with the development of a second peak in the U'_{rms} profile.

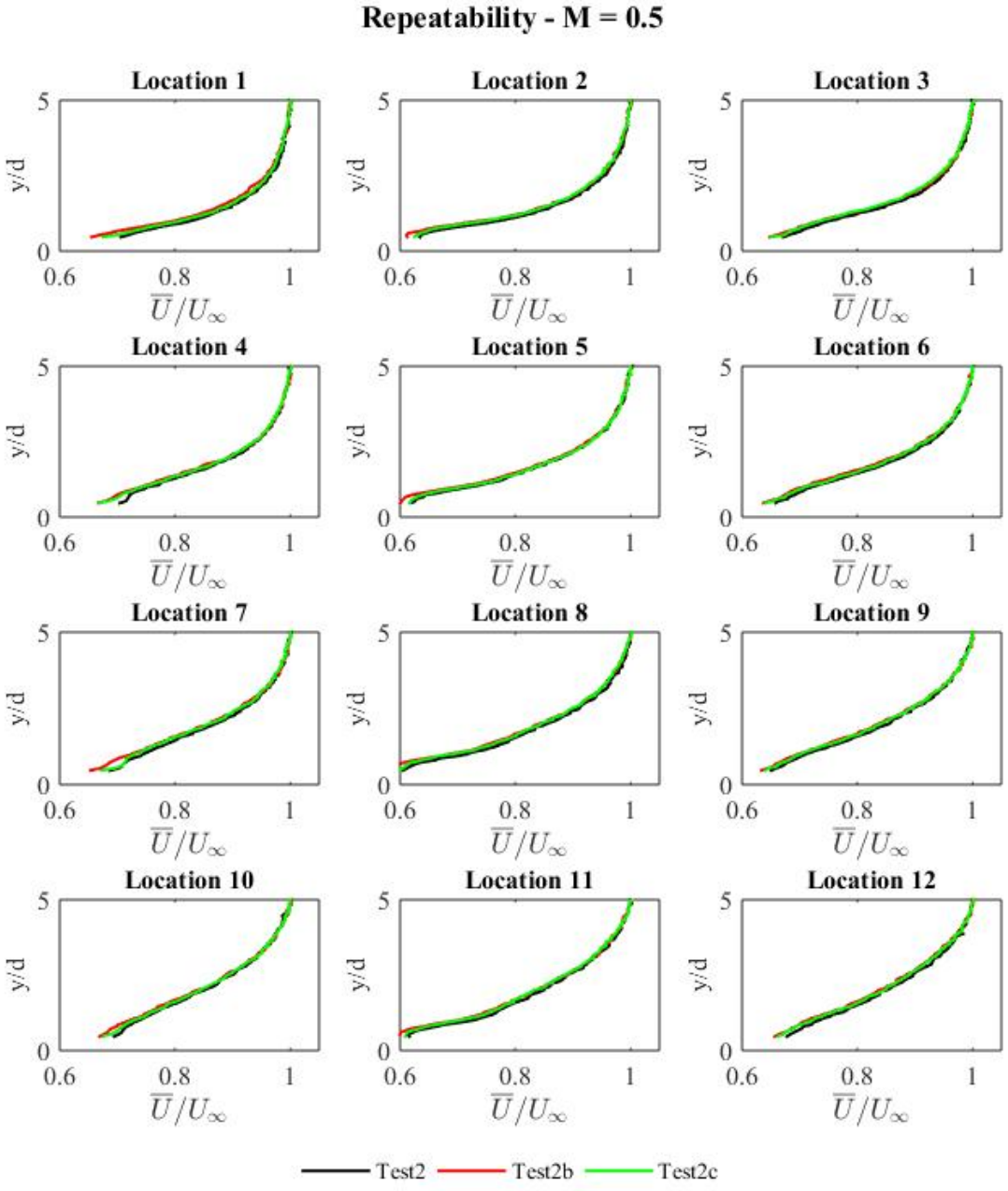

Figure 5.5: Day-to-day average effective velocity repeatability - M = 0.5

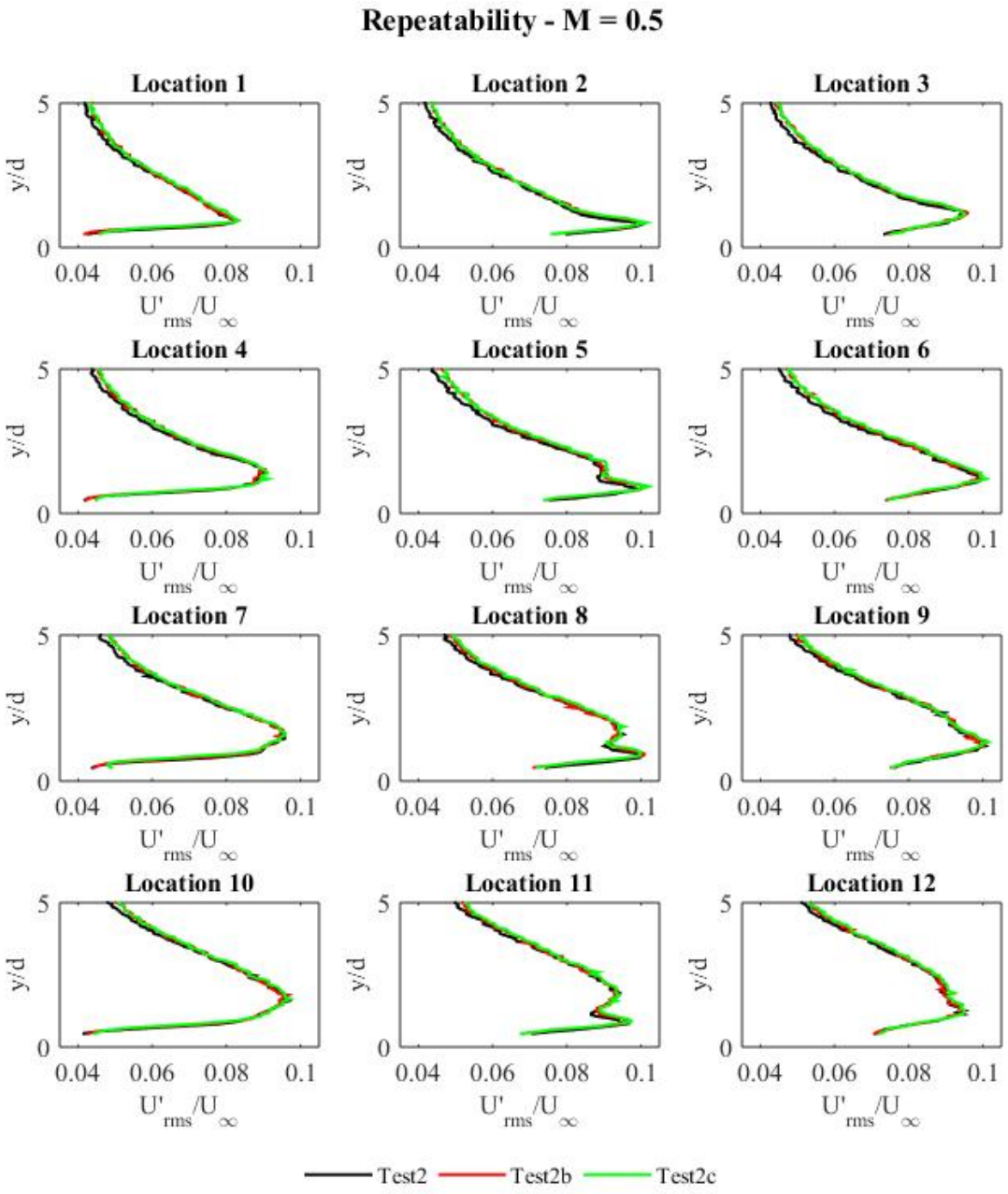

Figure 5.6: Day-to-day turbulence level repeatability - M = 0.5

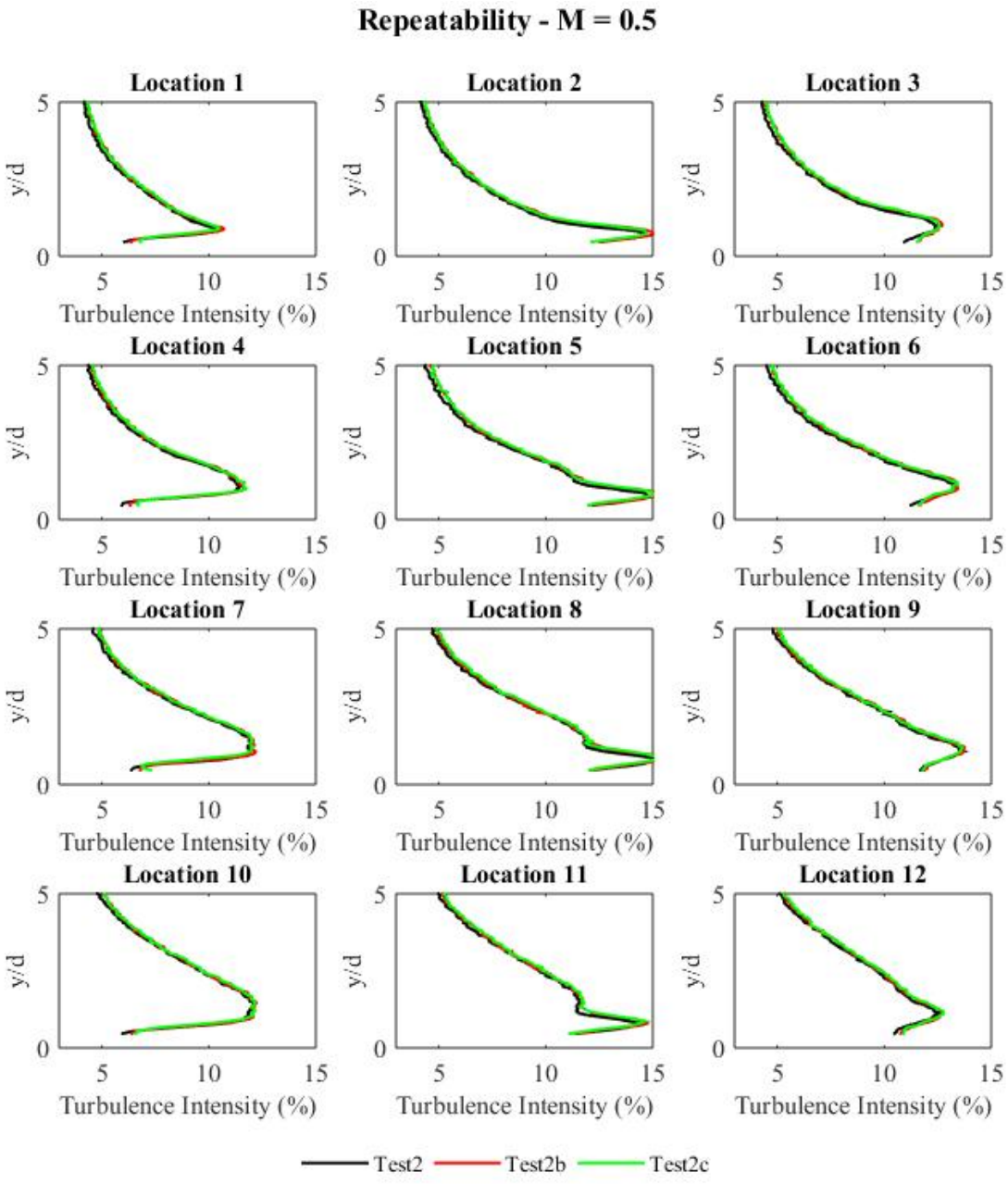

Figure 5.7: Day-to-day turbulence intensity repeatability - M = 0.5

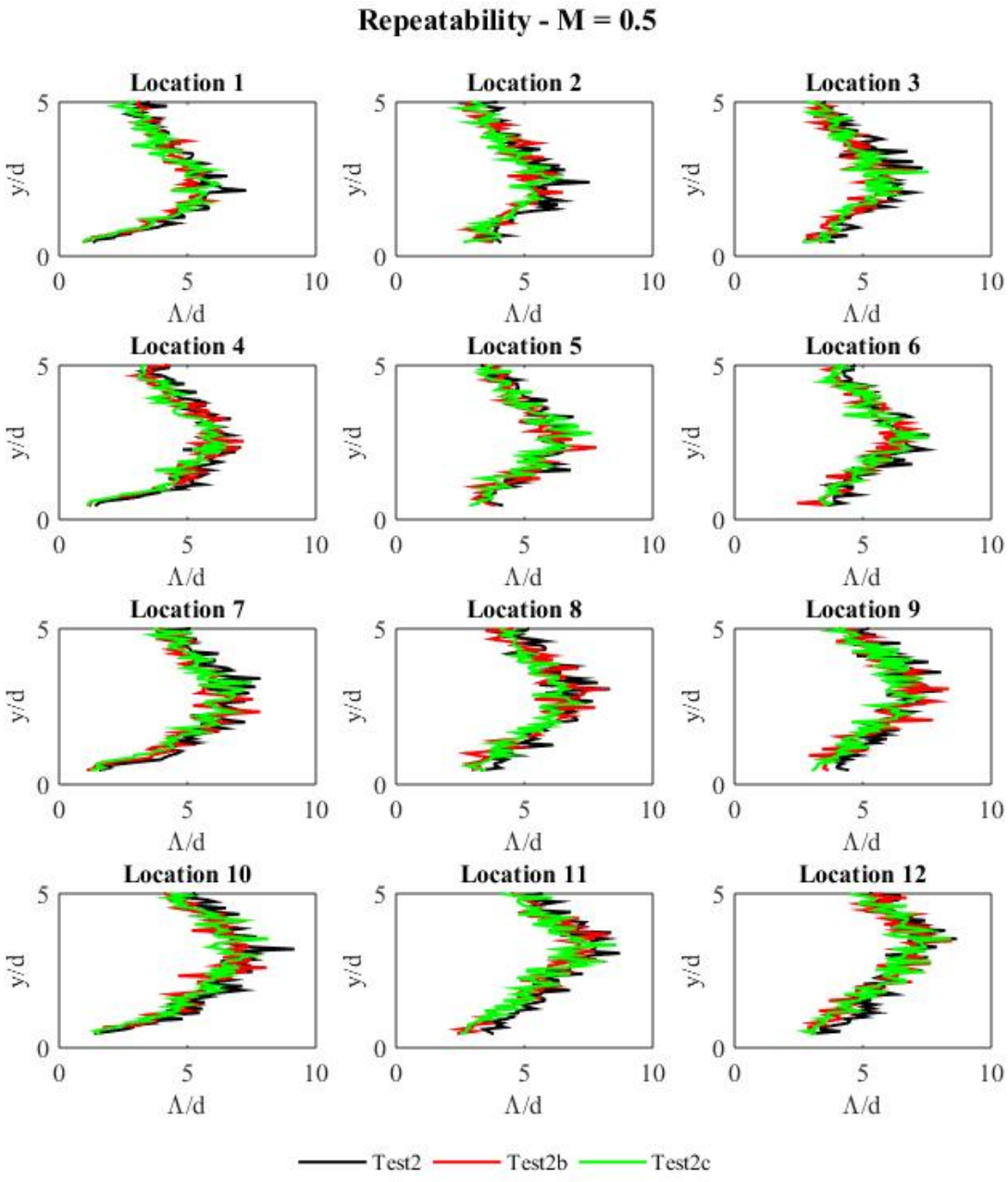

Figure 5.8: Day-to-day turbulence level repeatability - M = 0.5

Statistical Analysis - Blowing Ratio Comparison

The following sections describe the effects of different blowing ratios on the boundary layer approaching the film cooling array. Presented below are plots of mean effective velocity, turbulence level, and turbulence intensity of the boundary layer for cylindrical and diffuser geometries.

Average Effective Velocity

The mean velocity profiles measured in the centerline of the film cooling array is presented in this section. The mean velocity was calculated with equation 5.1 below. The measurement locations coincide with the trailing edge of 4 different holes, 5d, and 10d downstream of each of those holes. For convenience, the jets ensuing from each of the four holes is referred to as jets one through four as per their streamwise location. The data is presented in a 4x3 matrix such that each row displays line plots of each jet and each column displays either the trailing edge, 5d or 10d downstream of the particular jet. Maximum errors in effective velocity for each geometry is also displayed in the plots for convenience.

$$\bar{U} = \frac{1}{N}\sum_{i=1}^{n} u_i \tag{5.1}$$

Figure 5.9 below shows the mean velocity for blowing ratios 0.3, 0.5, 0.7, 1.0, and 1.2 injecting from the cylindrical array. The wall-normal position and mean velocity has been non-dimensionalized by the diameter and freestream velocity respectively. The lowest blowing ratio case does not show much deviation from a typical boundary layer. This is due to injection velocities similar to that seen in the near wall region of wall-bounded flows. Although discrepancies are expected to exist in the very near wall region, the hotwire probe was not traversed low enough to

capture them. Similar to M = 0.3, M = 0.5 case is also still in the mass addition regime and appears to remain attached to the wall. A slight elevation is noticed in velocities near the wall at locations just downstream of injection but tends to relax by 5d downstream. M = 0.7, 1.0, and 1.2 all show jet profiles are taken as evidence of jet lift-off at the trailing edge. Blowing ratio case of 0.7 appears to re-attach as the first two jets relax by 5d downstream. Jets 3 and 4 also re-attach but retain elevated velocities in the near wall region as the jets propagate to 10d downstream. M = 1 case shows clear jet-lift off at each downstream location and identifiable velocity peaks 5d downstream. Jet cores are not distinguishable 10d downstream, however, due to velocities approaching that of the freestream as the jets relax. The highest blowing ratio case tested on the cylindrical geometry displays a maximum jet core velocities of approximately 1.5 at the trailing edge. Shearing of the jets at this blowing ratio causes reduced peak velocities at 5d downstream and a severely dampened profile 10d downstream. However, jets still retain some identity even at this location far downstream thus potentially contributing to coalescing effects on succeeding jets.

Figure 5.10 below shows the mean velocity for blowing ratios 0.5, 0.7, 1.0, 1.2, and 1.5. A blowing ratio of 0.3 has been excluded and a higher blowing ratio case has been included as diffuser shaped geometries are known to remain attached to the surface at significantly higher blowing ratios in comparison with that of cylindrical geometries. A comparison of the two geometries will also be conducted later in the document to exemplify this flowfield discrepancy. At low blowing ratios of 0.5 and 0.7, centerline jets appear to remain attached to the surface assuming the shape of a typical turbulent boundary layer profile initially. However, injection appears to retard the approaching boundary layer changing the shape of the boundary layer profile and recording significantly lower velocities near the wall at locations 5d downstream of each centerline jet. Mean streamwise velocities do appear to speed back up by 10d downstream of each jet yet not enough for downstream jets to retain similarity in shape compared to the upstream jets. While this phenomenon is clearly visible for low blowing ratios, it appears to be present and active for all blowing

ratios. M = 1, 1.2, and 1.5 show appearance of a jet core at the trailing edge of each jet with highest mean velocity at the first row trailing edge. These peaks reduce in magnitude at downstream locations with each row of blowing. For M = 1 case, the jets tend to relax by 5d downstream to profiles similar to that observed in the lower blowing ratio cases. At the high blowing ratios tested, jet cores are visible for 5d downstream of jets 1 and 2 but lose shape by 10d downstream. Noticing that the velocity profiles for M = 1.2 and 1.5 do not fully relax by 10d, it appears that the heightened velocities near the wall propagate further to influence the downstream jets. At these M, downstream jet velocity profiles are observed to ”peel away” from that of the boundary layer. This coalescing effect is also seen for high cylindrical cases. A higher convective velocity in the near wall region coupled with low velocity gradients in this region allows jets to be propagated much further downstream.

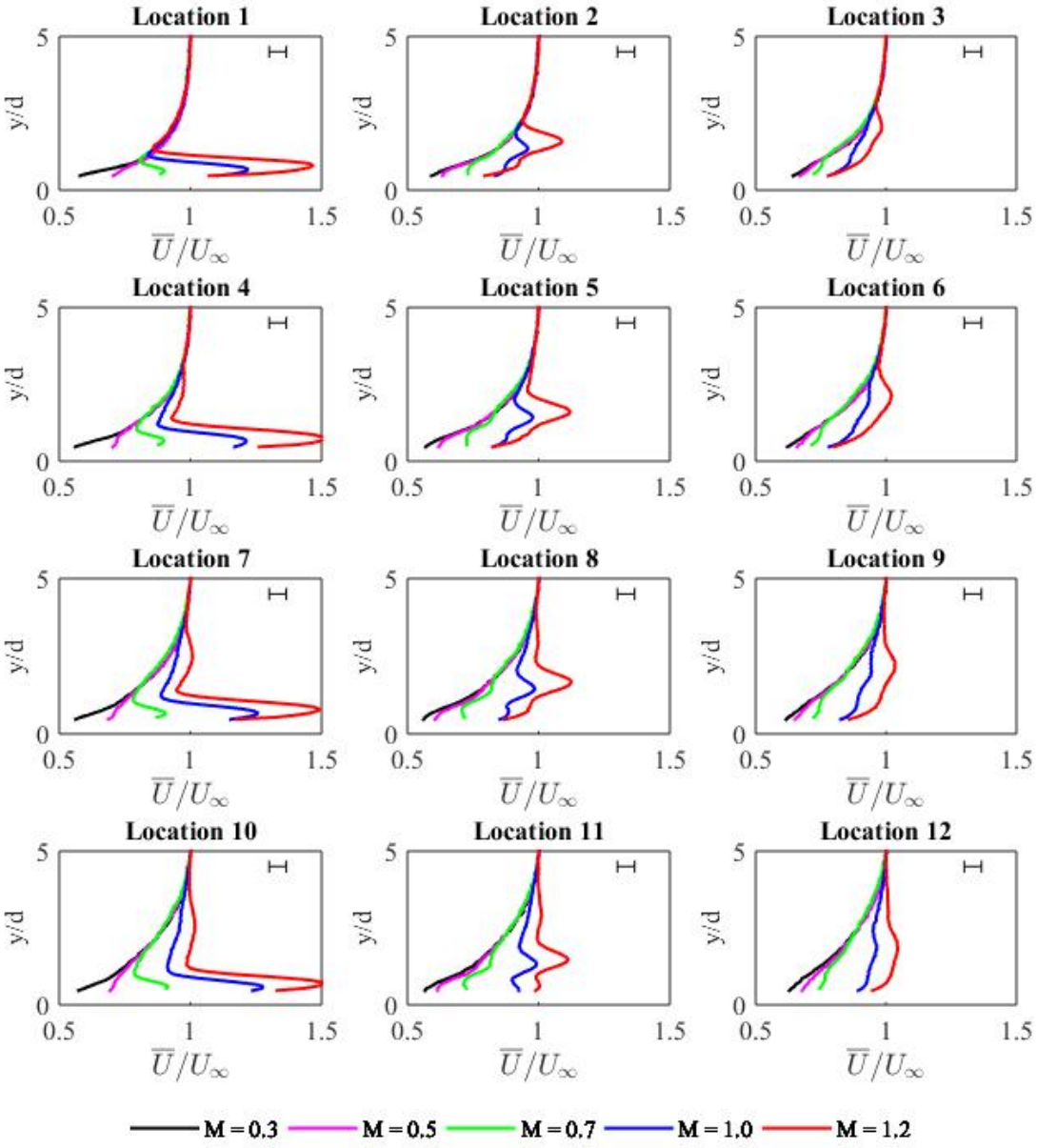

Figure 5.9: Average velocity profiles for cylindrical geometry

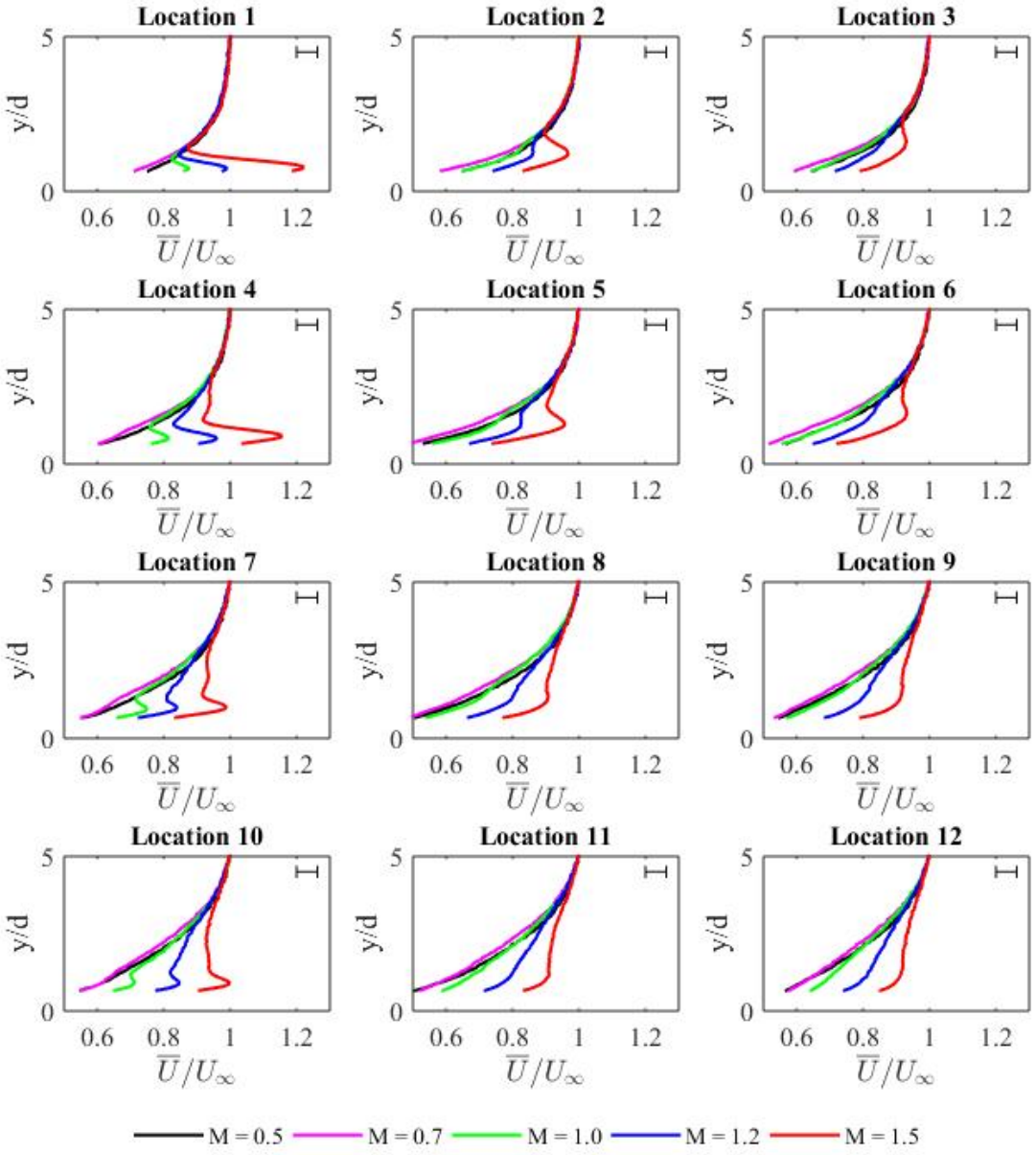

Figure 5.10: Average velocity profiles for diffuser geometry

Typical boundary layers have an associated boundary layer thickness, δ_{99}. In addition, a dis-

placement and momentum thickness given by equations 5.2 and 5.3 below is also used for boundary layer calculations. These calculations assume a density gradient is minimal. Displacement thickness is defined as the distance by which the external potential flow is displaced outwards due to the decrease in velocity in the boundary layer. Momentum thickness is defined as the distance by which the boundary should be displaced to compensate for the reduction in momentum of the flowing fluid on account of boundary layer formation. Since the mean velocity profiles for diffuser vary so much from that of cylindrical at downstream locations, a comparison of these quantities is warranted.

$$\delta^* = \int_0^\infty \left(1 - \frac{\bar{U}}{U_\infty}\right) dy \tag{5.2}$$

$$\delta^{**} = \int_0^\infty \frac{\bar{U}}{U_\infty}\left(1 - \frac{\bar{U}}{U_\infty}\right) dy \tag{5.3}$$

While applying displacement and momentum thickness to film cooled boundary layers is not conventional, the calculations were conducted and are included below. For these calculations, a spline curve fit was used in Matlab and the calculations were done for a delta y/d of 0.001. Figures 5.11 and 5.12 below show the displacement and momentum thicknesses respectively for all blowing ratios and both geometries. The figures are plotted in terms of downstream location from the first row trailing edge.

The trends in displacement and momentum thicknesses are identical but vary in magnitudes obviously. Cylindrical geometries show decreasing thicknesses with increasing blowing ratios. Diffuser geometry, on the other hand, shows an increase in displacement thickness for M up to 0.7 and then a decrease at higher blowing ratios. Sharp drops of displacement thickness with downstream location are caused by minima in the $\bar{U}$ profile.

In general, the diffuser case has significantly higher displacement and momentum thicknesses compared to the cylindrical geometry at any given blowing ratio. This severe discrepancy is found as a result of the boundary layer being ”dragged” in the case of blowing through diffuser geometries. This should result in significantly higher film cooling effectiveness for this particular geometry. However, without additional surface effectiveness measurements at this density ratio, it cannot be confirmed.

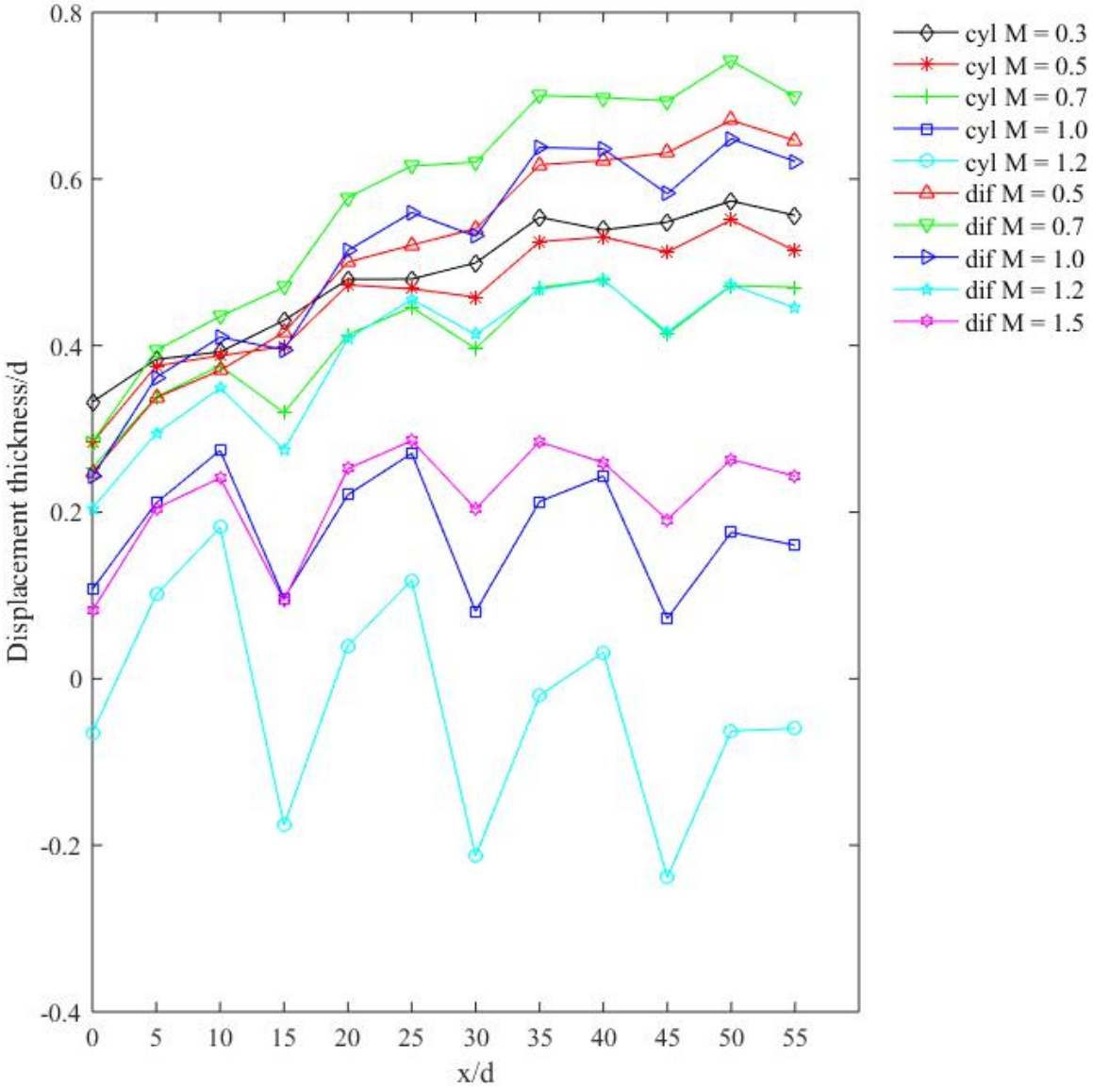

Figure 5.11: Displacement thickness for cylindrical and diffuser geometries

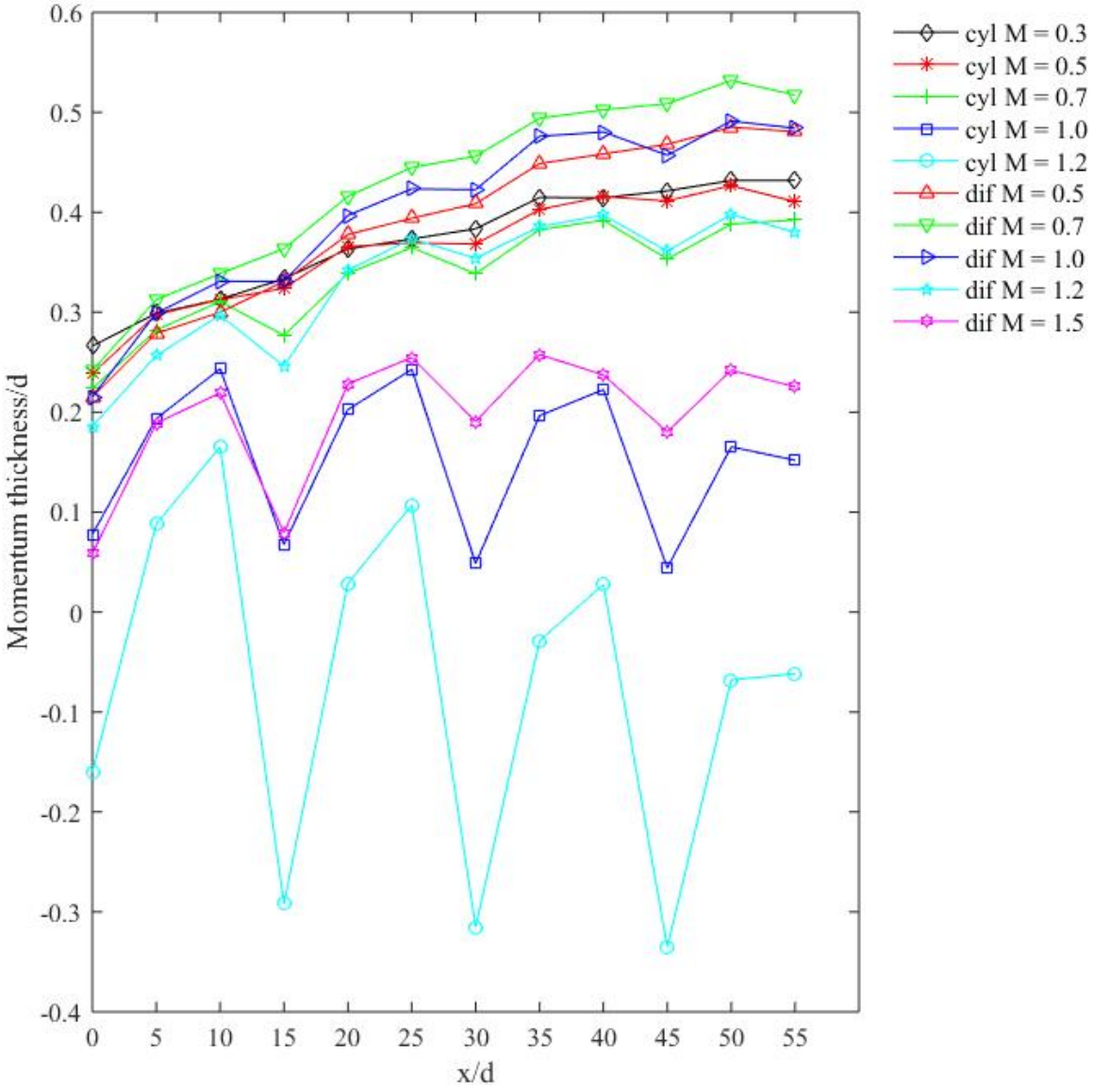

Figure 5.12: Momentum thickness for cylindrical and diffuser geometries

Turbulence Level

In this section, turbulence level profiles measured at the centerline of the film cooling array is presented. Turbulence is said to be an instability generated by shear. The higher the amount of shear, the stronger the turbulence. Shear is driven by velocity gradients in boundary layers. Thus higher gradients of velocity lead to increased turbulence production. Streamwise component of turbulence level can be defined as the standard deviation of the turbulent fluctuations in the streamwise direction given by equation 5.4 defined below. The data is presented in a similar way as the mean velocity profiles however low blowing cases are separated from high blowing ratio cases for improved visual of the profiles. Figures 5.13 and 5.14 below show the turbulence level profiles for blowing ratios 0.3, 0.5, 0.7, 1 and 1.2 injecting from the cylindrical geometry. Again, the wall-normal position and U'_{rms} has been non-dimensionalized by the diameter and freestream velocity respectively.

$$U'_{rms} = \sqrt{\frac{1}{N}\sum_{i=1}^{N}(u_i - \bar{U})^2} \tag{5.4}$$

Low blowing ratios of 0.3 and 0.5 show qualitatively similar turbulence level profiles compared to that of a turbulent boundary layer which peaks at the laminar sublayer. The peak U'_{rms} in these cases display the location of highest shear between the jets and freestream raised since lower velocity fluid is pushed further away from the wall due to injection.

Higher blowing ratios of 0.7, 1, and 1.2 show clear evidence of lift-off with two distinct peaks particularly at 5d downstream of each jet. The peaks signify the shear layer between jet and mainstream and entrainment of mainstream fluid towards the surface generating shear at locations under the ensuing jets. The peaks are clear and distinct as a result of the velocity gradient between freestream and jets for M = 0.7 as opposed to that of M = 1 where the peaks are difficult to identify.

As a result of the velocity gradient between freestream and jets, the U'_{rms} peaks are clearly visible for M = 0.7 as opposed to M = 1 where the velocity gradients are close to unity. At jet velocities greater than that of the freestream, with every row of blowing, turbulent levels in the boundary layer drop. This is due to interaction of vortical structures from the freestream of similar magnitude but opposing those of the ensuing jet having a destructive effect. This low level of turbulence is then convected downstream propagating and growing with every row of blowing.

Figures 5.15 and 5.16 below show U'_{rms} profiles for jets issuing out of the diffuser shaped array at blowing ratios of 0.5, 0.7, 1, 1.2, and 1.5. Low blowing ratios of 0.5 and 0.7 show peaks in certain locations similar to seen in the cylindrical array. First row of blowing peaks are a little difficult to see for M = 0.5. Traversing closer to the wall would obtain these peaks. Not only do these peaks grow in magnitude but also appear to spread in the wall normal direction with every row of blowing. This is attributed to growth of the boundary layer due to mass addition causing growth of the shear layer between jets and freestream. At higher blowing ratios, jet cores are apparent for jets 1 and 2 but are not distinguishable for jets 3 and 4. For M = 1.0 case a dual shear layer is visible 5 and 10 diameters downstream of jets 1 and 2 yet remain very close to the wall. This indicates slight entrainment of mainstream fluid below the jet causing reduced film cooling performance in these regions. Jets 3 and 4 shows a drop in turbulence levels above the jets compared to that from previous rows and also lower blowing cases. Increasing the blowing ratio even more shows larger drops in turbulence level above the jets and this drop off is noticed even as early as the trailing edge of jet 2.

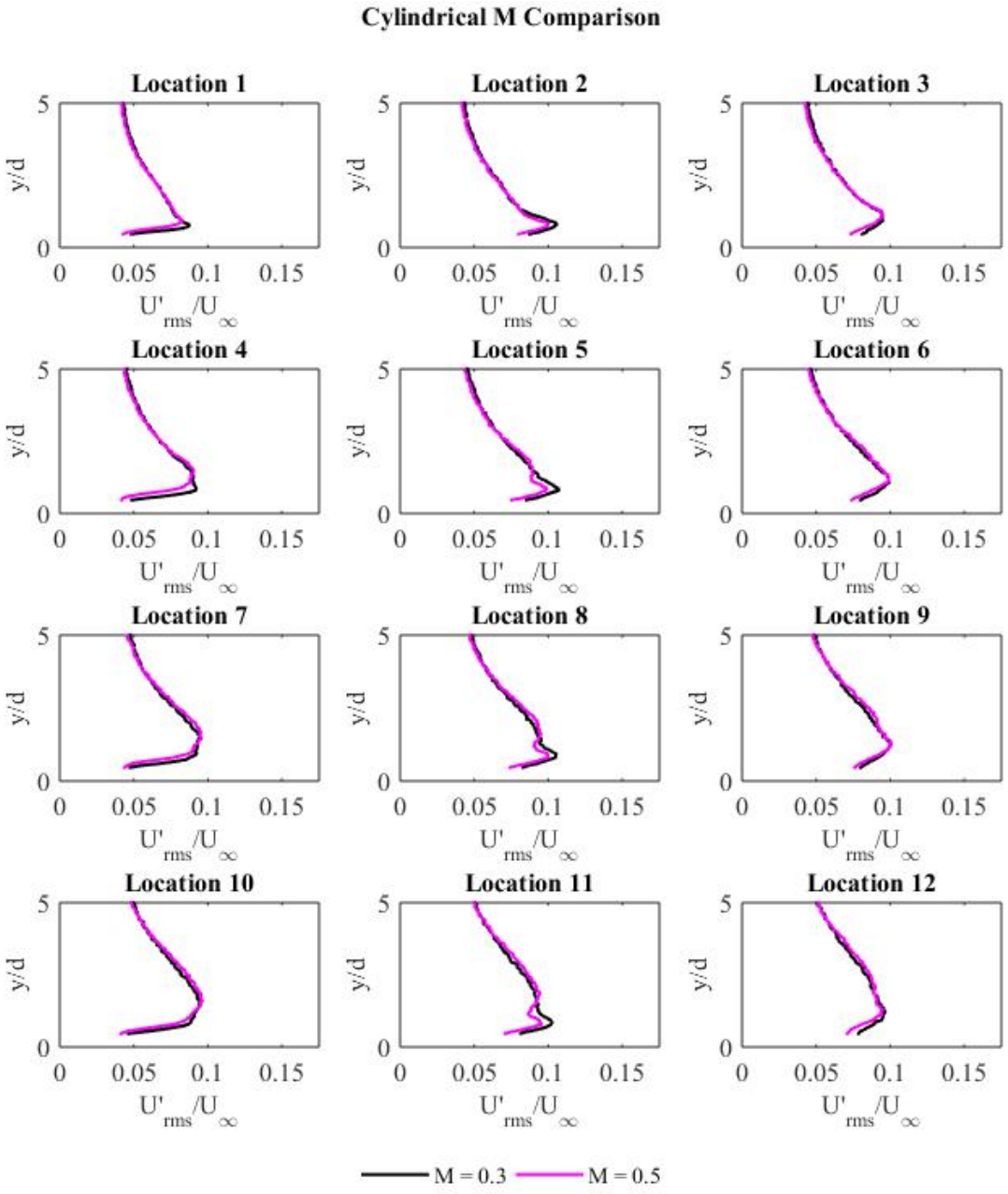

Figure 5.13: Turbulence level for low blowing ratio cases of cylindrical geometry

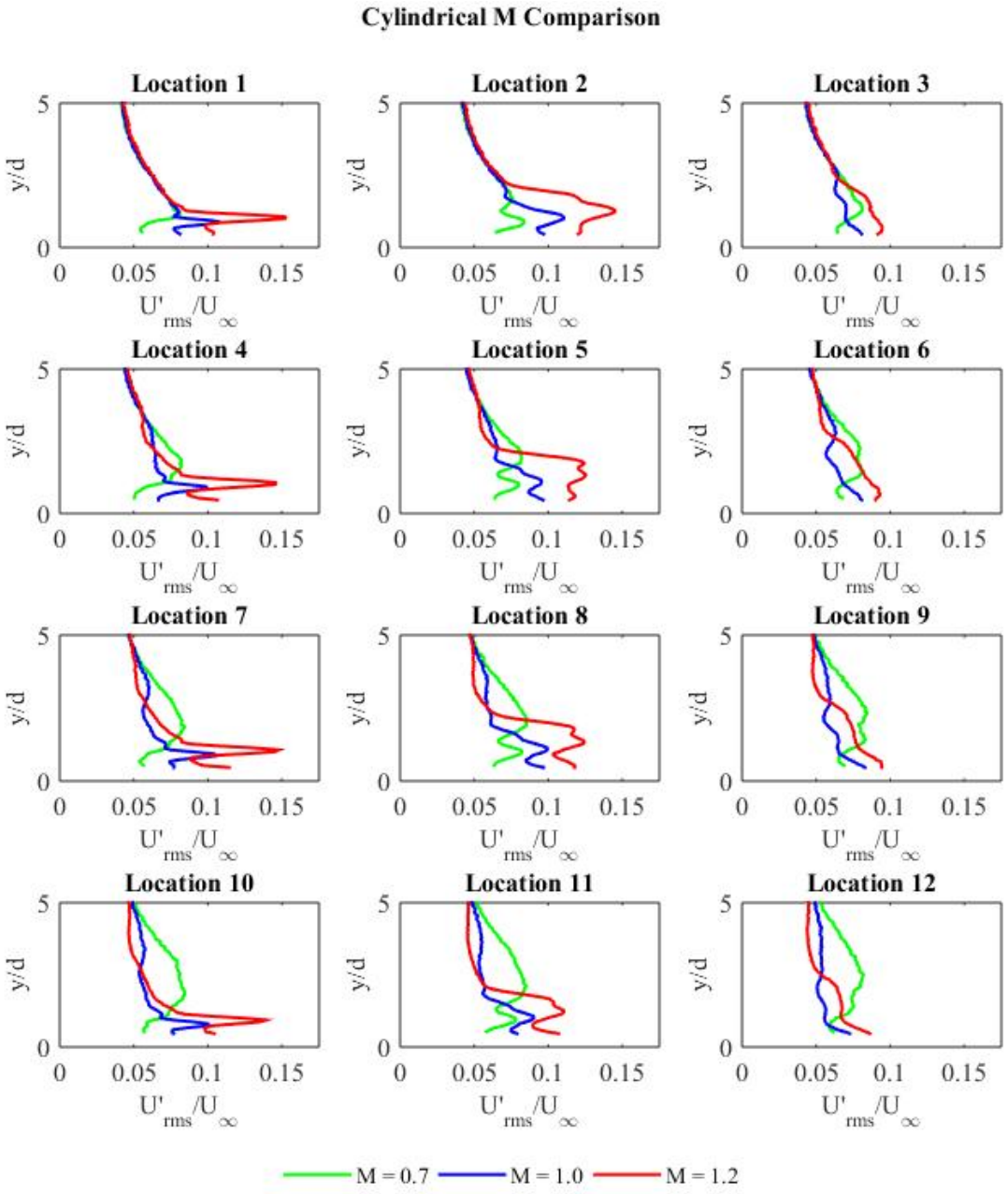

Figure 5.14: Turbulence level for high blowing ratio cases of cylindrical geometry

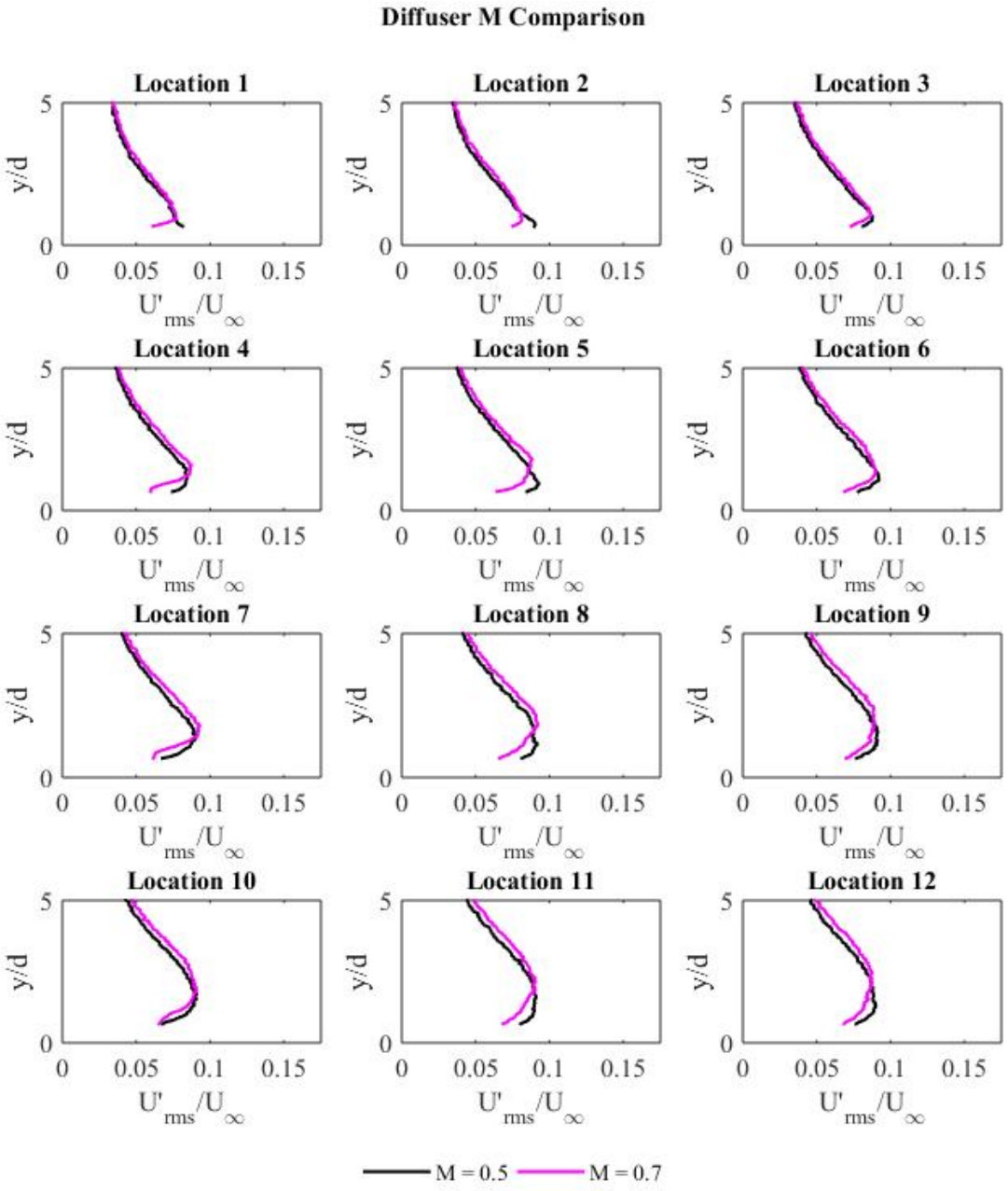

Figure 5.15: Turbulence level for low blowing ratio cases of diffuser geometry

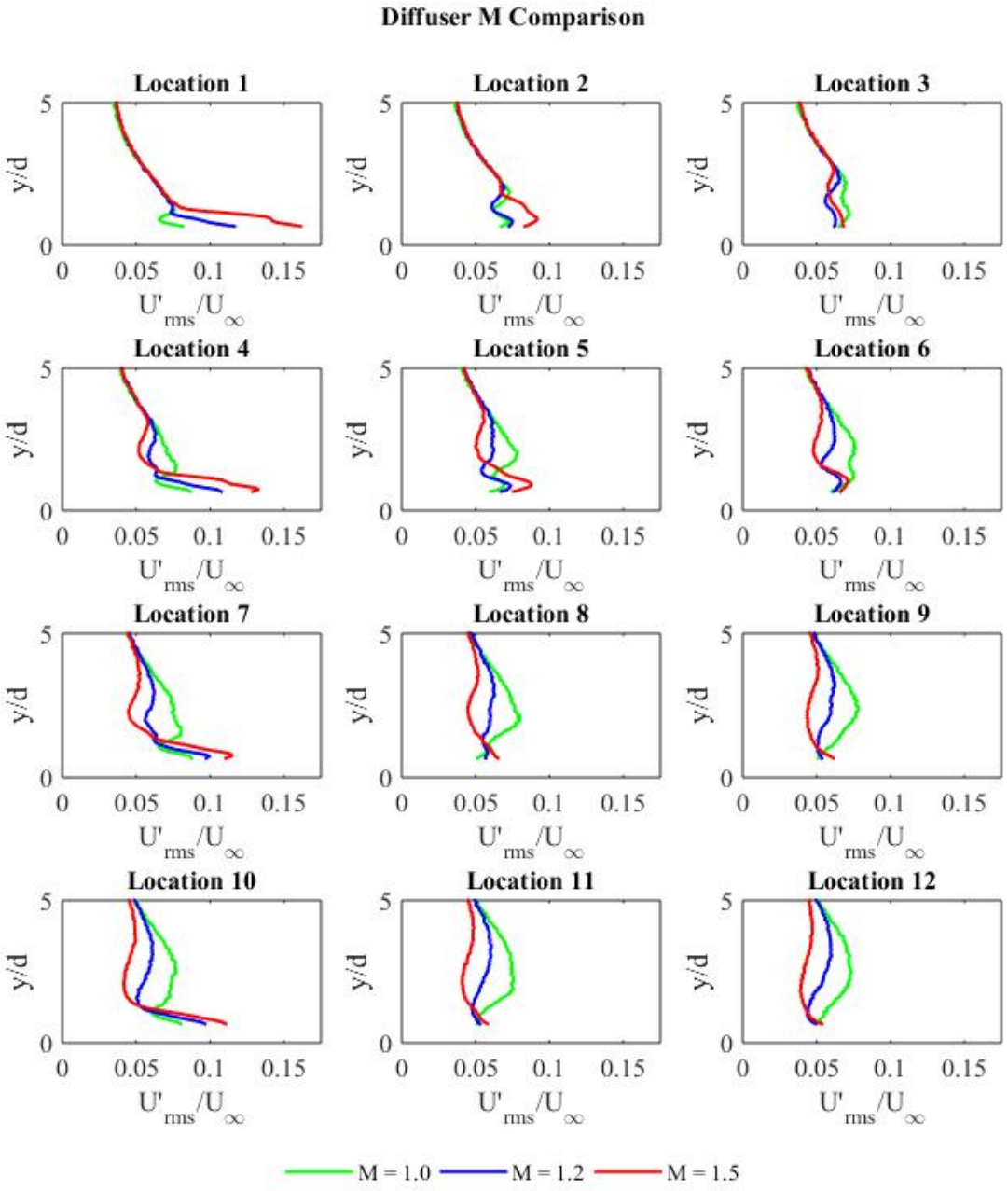

Figure 5.16: Turbulence level for high blowing ratio cases of diffuser geometry

Integral Length Scale

Integral length scales are the sizes of the largest eddies in the flow and are known to account for most of the transport of momentum and energy. They can be calculated by obtaining the zero frequency energy from the energy density spectrum. First the raw velocities are converted from the time domain to the frequency domain using a Fast Fourier Transform. Once in the frequency domain, Power and Energy can be calculated according to equations 5.5 and 5.6 below where L is the length of the time-series and f is the frequency in Hz.

$$Power = \frac{abs(fft(U))^2}{L} \tag{5.5}$$

$$Energy(f) = \frac{Power}{f} \tag{5.6}$$

Integral Length Scales can then be calculated by eqn 5.7 below. To obtain the energy as the frequency approaches zero from teh data, the first 100 points are averaged, where the data asymptotes to a fixed value at the low frequencies [30].

$$\Lambda_I = \left[\frac{E(f)U_{mean}}{4\,U'_{rms}}\right]_{f\to 0} \tag{5.7}$$

Figure 5.17 below shows the energy density spectrum for a velocity sample taken at the trailing edge of the first row at a blowing ratio of 0.3.

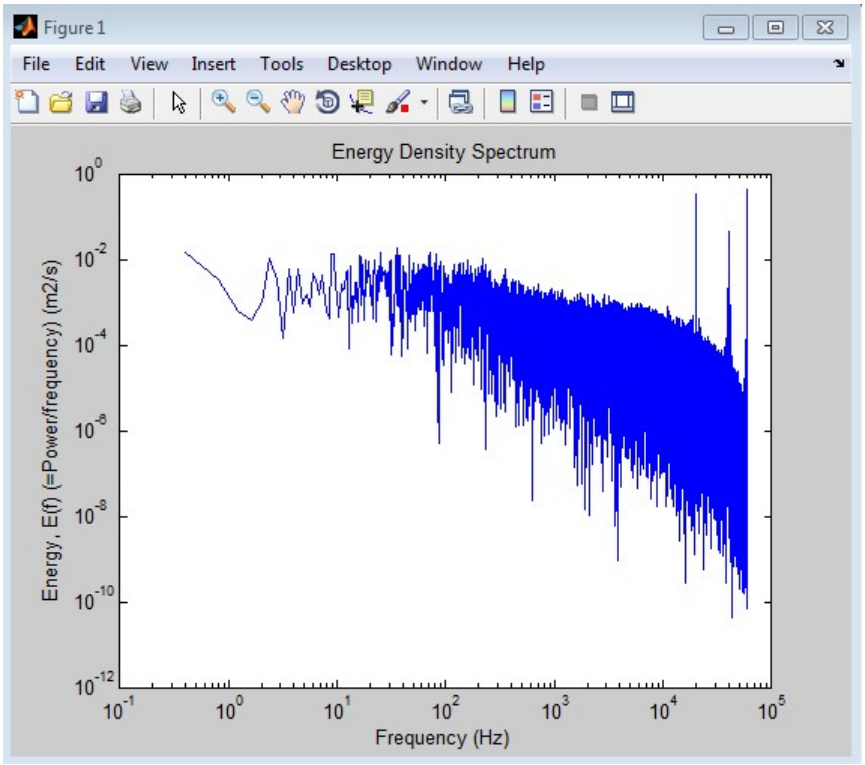

Figure 5.17: Sample Energy Density Spectrum at first row trailing edge of hole, M = 0.3

To prove validity and consistency in measurement, additional tests were conducted in a constant area duct of a low speed wind tunnel operating under suction. The main flow was sucked through a 2D contraction with inlet to exit area ratio of 5.23. The contraction was designed using a fifth order polynomial shape [31]. A woven turbulence mesh grid was installed at the exit of the contraction with wire diameter 2mm and mesh size 5mm x 10mm. The hotwire was installed in the midspan of the constant area duct 127mm downstream of the turbulence grid. The air flows through the constant area duct to a high pressure plenum and is then dumped outside the facility. An image of the test setup can be viewed in Figure 5.18 below. The flowfield was sampled at 60kHz and filtered at 30kHz for 30s. The velocity measured by the hotwire (3 m/s and 3.7m/s) was verified using a pitot tube placed at the same downstream location in the channel. Integral lengthscales were calculated according to the procedure described above and were found to be about 5mm.

Non-dimensionalizing the lengthscale by the diameter of the mesh screen gives a value of around 2.3. This can be compared to the correlation found by Roach [32], given by equation 5.8 below which obtains a value of 1.59. Hence the experimental integral lengthscales are slightly higher than that expected according to the correlation however, the correlation was found for a purely 2D turbulence grid while the one used in this particular study was woven which introduces a slight three dimensional effect on the problem. Additionally, the experimental work has a fair spread about the correlation which gives credibility to the measurement technique. Averaging techniques such as using a Hamming window or using Pwelch's power spectral density estimate might also narrow the gap between the experimental work and the correlation found in Roach. For the present study, the sampling time is kept low to reduce large ambient temperature changes, sensor drift and contamination of the probe since the film cooling wind tunnel is in an unconditioned work-space. Hence, increasing the sampling time may improve the accuracy of the measurements at hand.

$$\Lambda_x/d = 0.2(x/d)^{1/2} \tag{5.8}$$

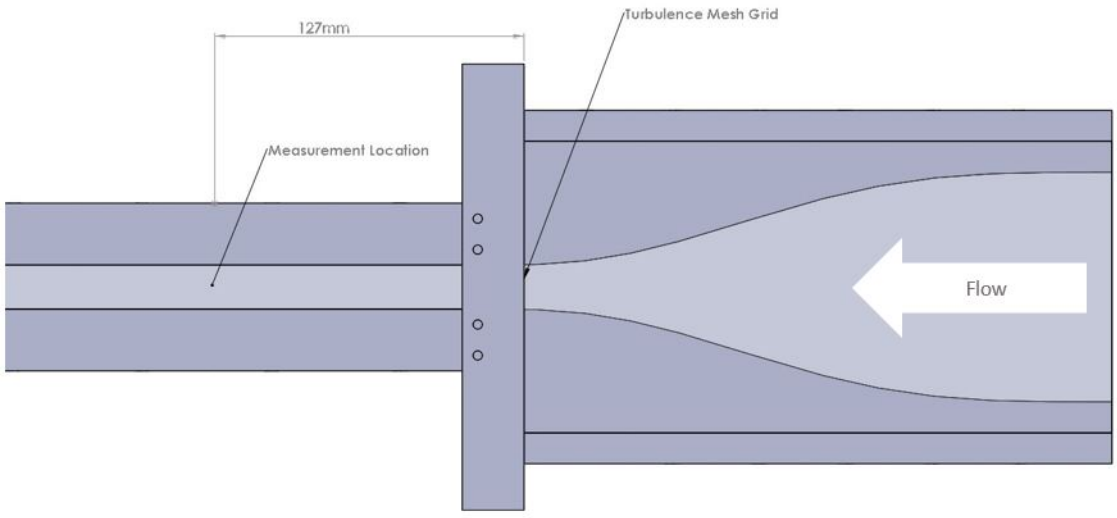

Figure 5.18: Turbulence grid test setup for validation of integral length scale calculations

Calculation of the integral length scales is conducted for each of the 70 vertical locations at each of the 12 horizontal locations per test. The results are plotted in figures 5.19 and 5.20 for the cylindrical and diffuser geometry respectively. The integral length scales in the freestream are measured to be within 7-10% of the hydraulic diameter which is acceptable for channel flow computational modeling using Fluent.

With film cooling through the cylindrical array, low blowing ratios of 0.3, 0.5 and 0.7 show similar integral lengthscales within the boundary layer. Lower blowing ratios however are subject to higher shear due to large velocity gradients which allows a longer correlation. Much larger discrepancies exist for the higher blowing ratio cases. Integral length scales are reduced in magnitude with jets penetrating into the boundary layer. Interactions between similar sized eddies from high blowing ratio jets and the incoming boundary layer cause much shorter correlations. While in the near wall, lengthscales are of similar magnitude compared to the lower blowing ratio cases, but the effect described above is seen primarily in regions where the lifted off jet interacts with the boundary layer into which it penetrates.

Integral length scales calculated for diffuser geometry show comparably different trends. All blowing ratio cases show similar trends compared to that of low blowing ratio cylindrical cases. Slight reduction in integral length scales is noticed for the highest blowing ratio of 1.5 for the first and second jet at 5 and 11 d downstream locations. This is due to the proximity of the jet core velocity to that of the freestream. Similar to cylindrical, interactions between eddies of the jets and freestream cause increased randomness and much shorter correlations. However, since the velocity gradient is high compared to the fluid within the boundary layer at the jet shear layer location, the correlations are still much better compared to that seen in the cylindrical case.

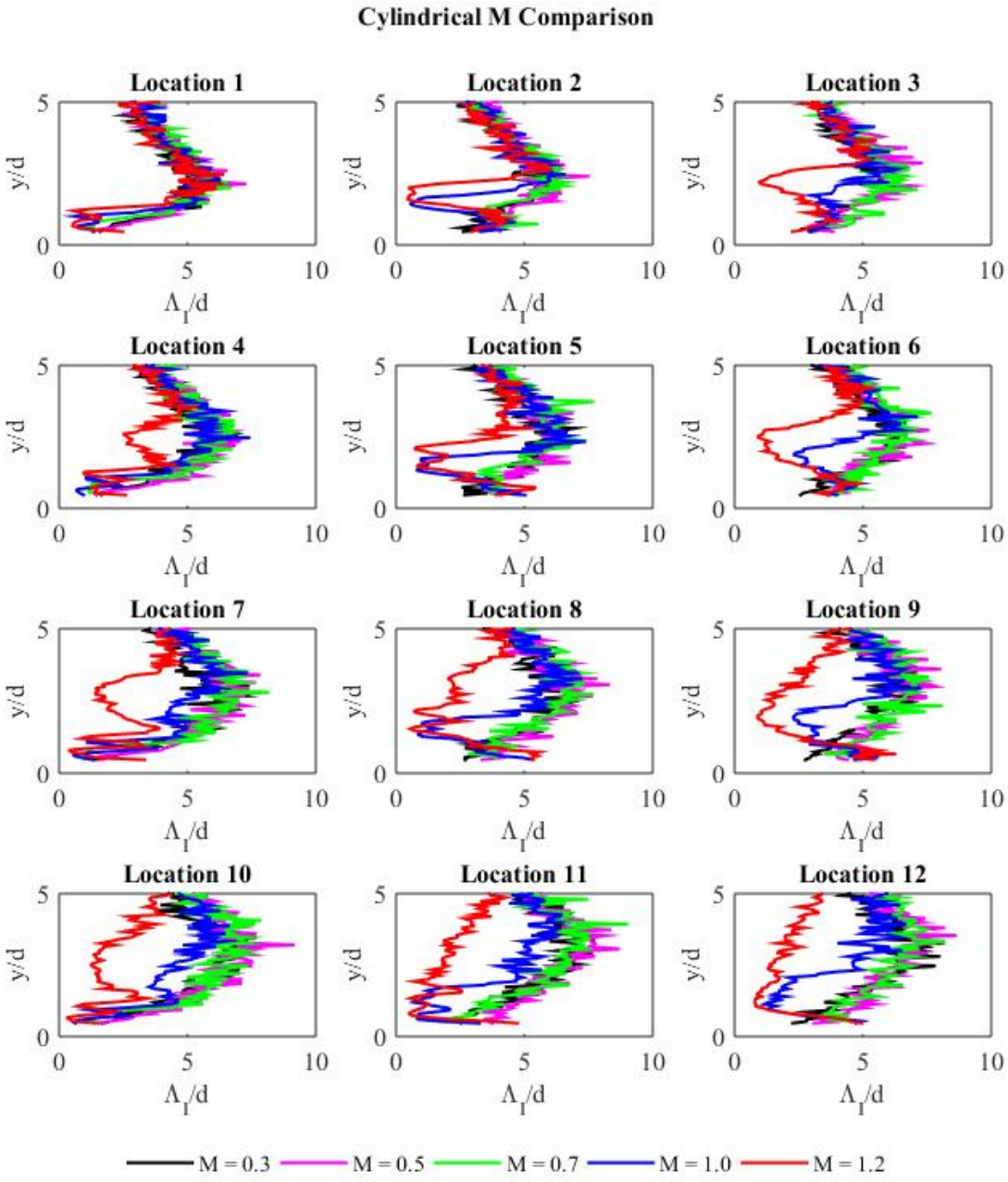

Figure 5.19: Integral length scales for cylindrical geometry

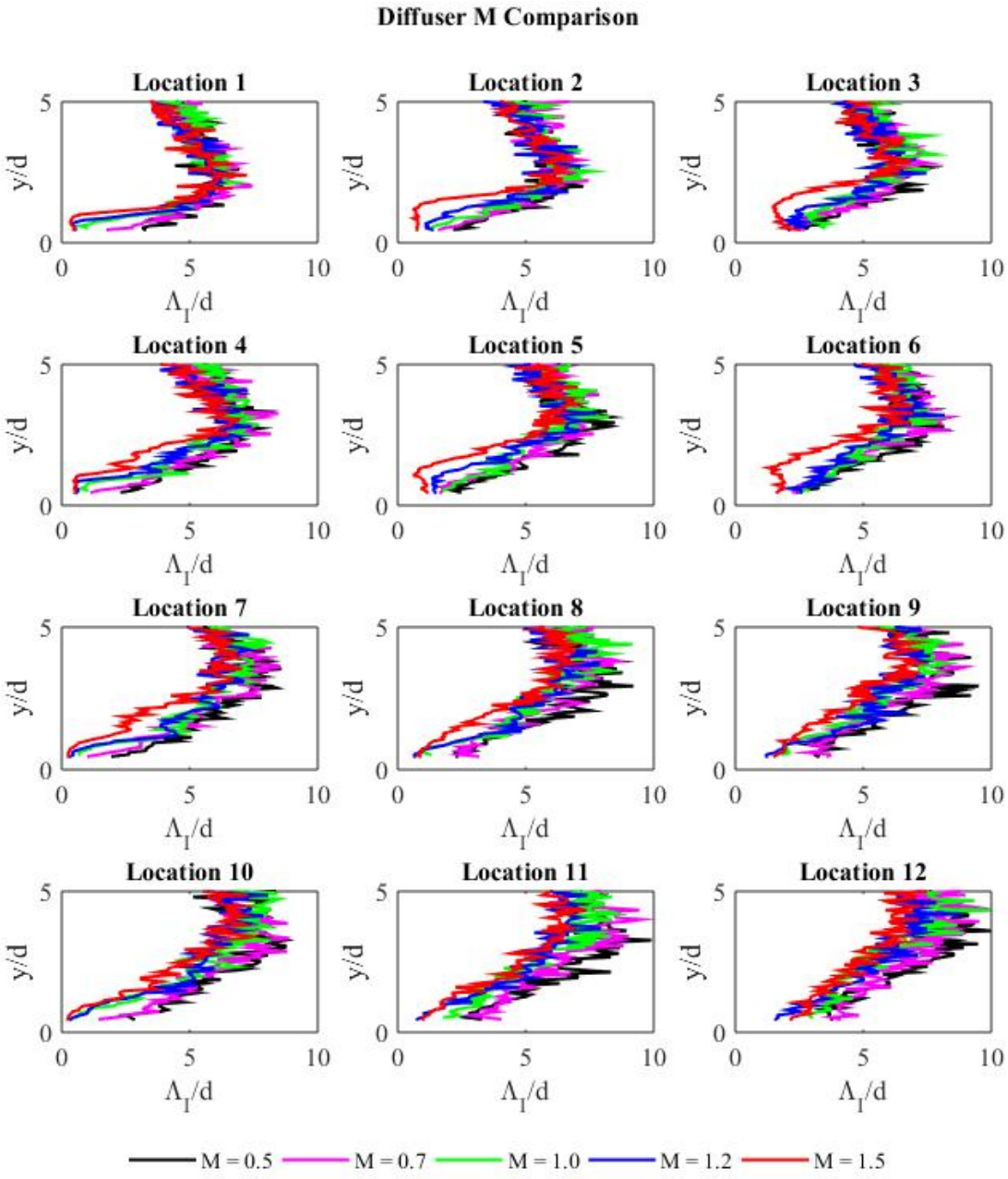

Figure 5.20: Integral length scales for diffuser geometry

Statistical Analysis - Location Comparison

This section analyzes the growth of the boundary layer and differences between similar locations downstream of jets in the array centerline. Special regard is given to magnitudes and locations of jet potential cores and shear layers for both geometries. For better flow of the paper, images of profile location comparisons for each blowing ratio are included in Appendix A but in the sections below. Figures in this appendix are plotted as three line subplots, each representing measurements at the trailing edge, 5d downstream and 10d downstream. The four jets are given the same color in each of the subplots for ease of reference. Example figures are included in this section to aid understanding and conveyance of analysis. In a similar fashion, $\bar{U}$ and U'_{rms} are non-dimensionalized by U_∞ while wall normal location (y) is non-dimensionalized by hole diameter d.

Average Effective Velocity

Location comparisons of mean effective velocity can be found in figures A.1 to 5.22 for cylindrical and 5.23 to A.12 for diffuser geometries. For cylindrical, at M = 0.3 to M = 0.7 velocity profiles are self-similar except that jet 1 tends to have slightly higher velocities compared to the rest of the jets as seen below in Figure 5.21. At low blowing of 0.3 and 0.5 particularly, the boundary layer profile tends to reduce in magnitude in the mid-section. M = 1 and 1.2 show very clear jet profiles at the trailing edge and 5d downstream. It is also very apparent that the fourth jet core is found to be much lower to the surface compared to the other jets as seen in Figure 5.22. Another interesting feature of these higher blowing ratios is that the first row velocities and peaks tend to be of lower magnitude compared to those of downstream jets which contrast that seen in low blowing ratios.

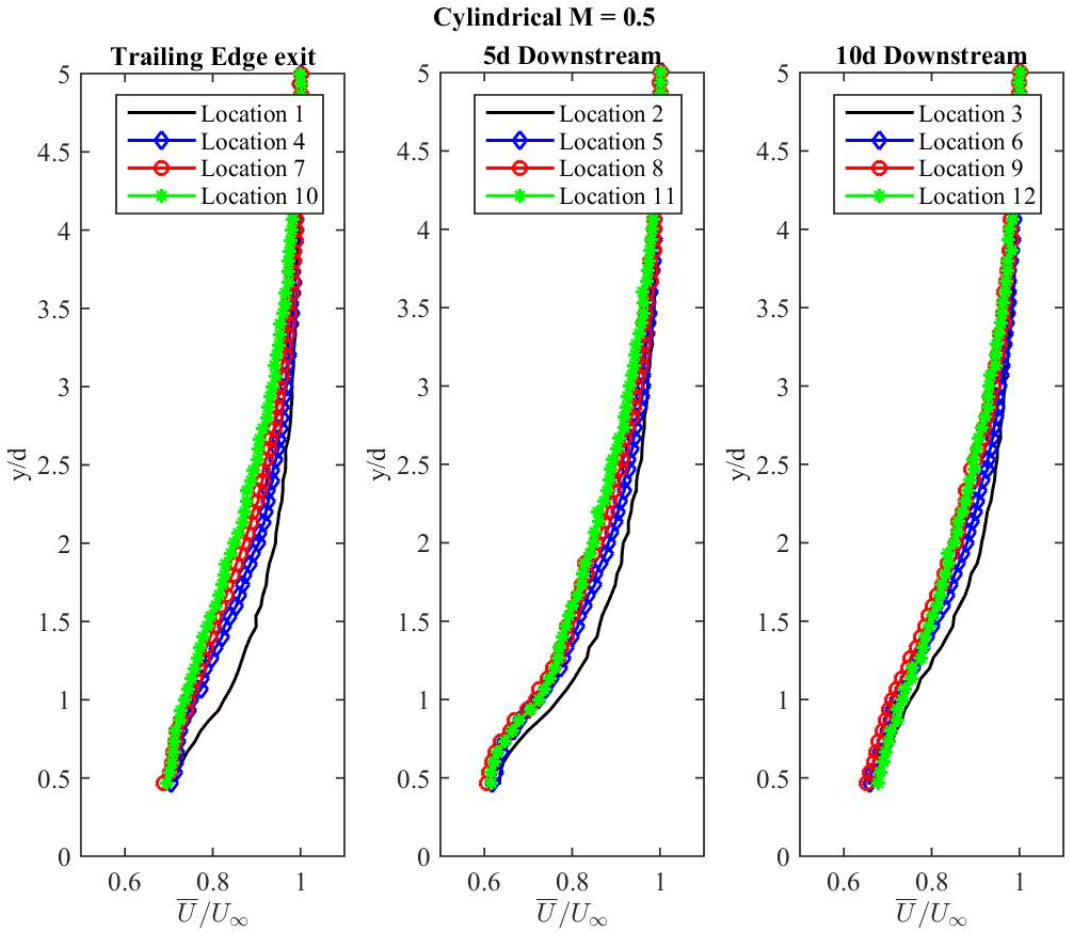

Figure 5.21: Average velocity profiles at trailing edge, 5d and 10d downstream of each cylindrical jet - M = 0.5

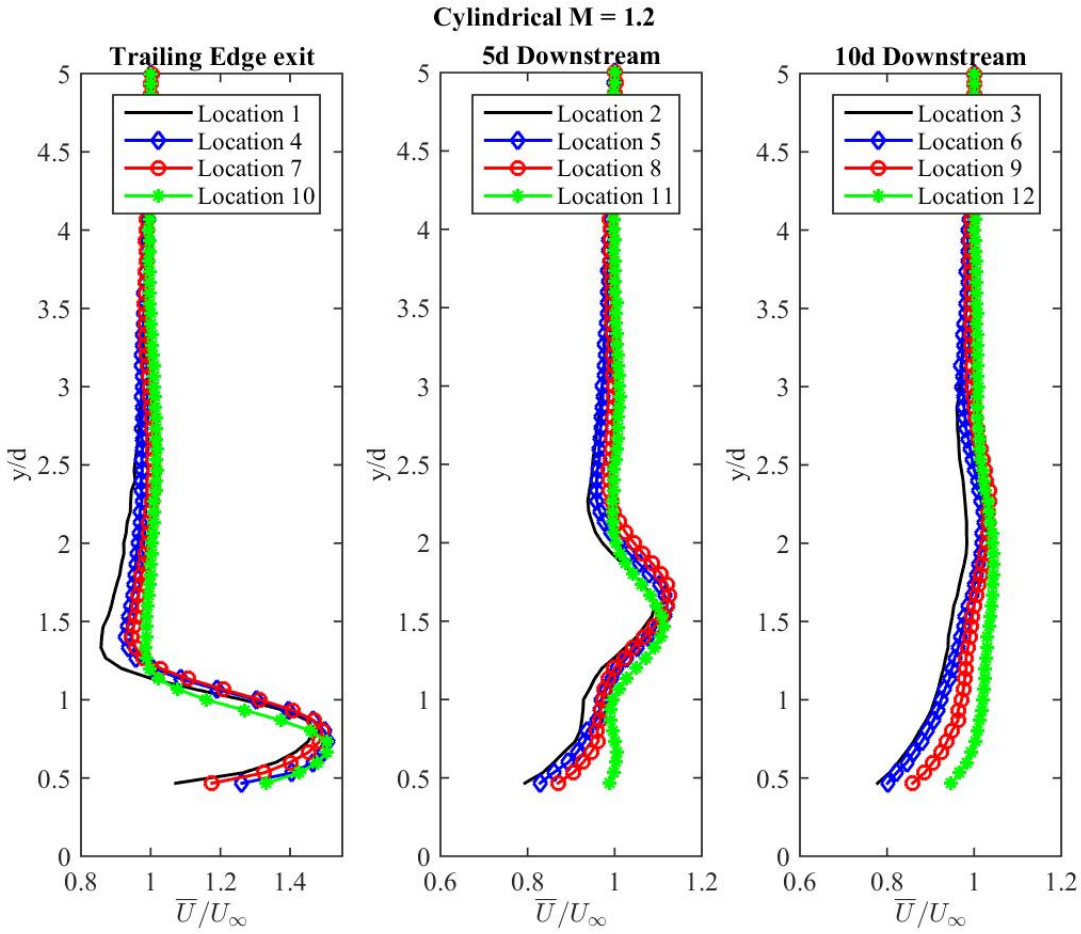

Figure 5.22: Average velocity profiles at trailing edge, 5d and 10d downstream of each cylindrical jet - M = 1.2

For diffuser geometry, while at low blowing ratios, the geometry tends to show similar results as cylindrical except with much more pronounced discrepancies between jets. Unlike cylindrical, jet 4 is seen to have much higher velocities in the near wall region compared with jets 2 and 3 for almost all blowing cases as seen in Figure 5.23. As noted previously, diffuser jet velocities are significantly reduced at 5d downstream of each jet demonstrating the diffusing nature of the

geometry. Unlike cylindrical jets, at high M, jet 1 issuing from the diffuser shaped hole retains its dominance compared to the succeeding rows as seen in Figure 5.24. With each row of blowing the jet appears to spread in a wall normal direction and reducing its peak magnitude at the trailing edge. However, jet 4 retains its velocity much better than jets 2 and 3 whose magnitudes drop with downstream propagation. This is due to the shearing nature of the incoming boundary layer affecting upstream jets. Downstream jets experience a protective shield effect from upstream rows of blowing thus being able to diffuse much better.

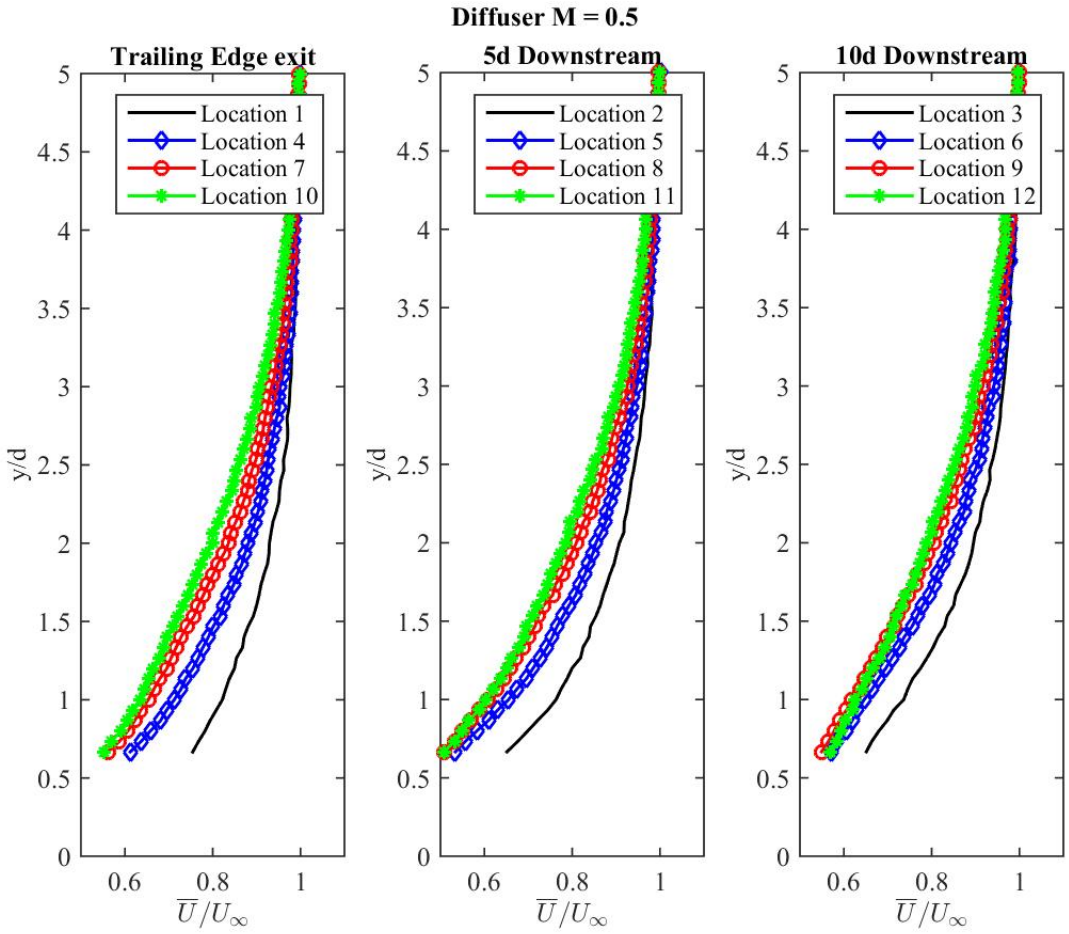

Figure 5.23: Average velocity at trailing edge, 5d and 10d downstream of each diffuser jet - M = 0.5

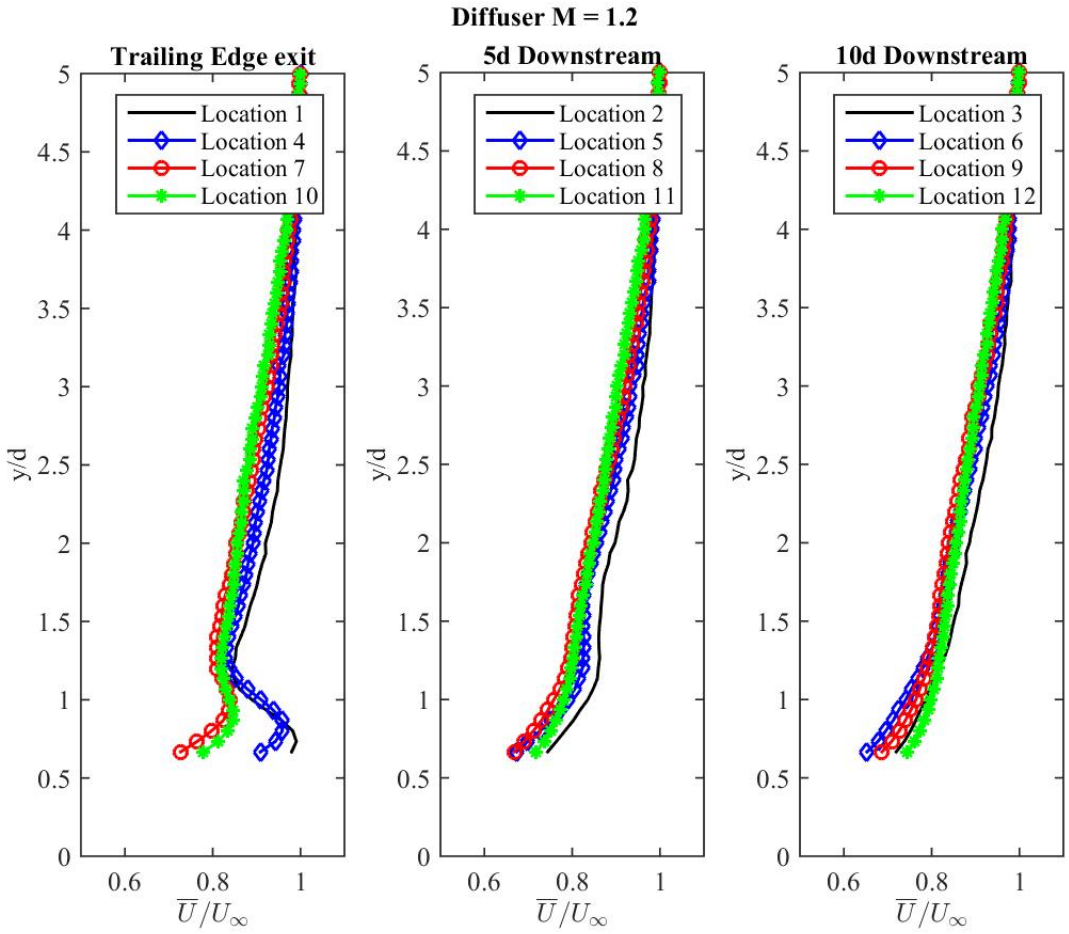

Figure 5.24: Average velocity at trailing edge, 5d and 10d downstream of each diffuser jet - M = 1.2

Turbulence Level

This section discusses some of the differences between U'_{rms} profiles of the four streamwise oriented jets in the centerline of cylindrical and diffuser shaped film cooling array. For low blowing ratios of 0.3, 0.5 and 0.7, turbulence levels remain consistent at downstream locations of each jet. Figure 5.25 displays this well. This entails that the jets do not experience any kind of coalescing

effects after injection. jet turbulence level profiles of higher blowing ratio cases M = 1 and 1.2 show signs of coalescence with peak location differences at downstream locations as seen in Figure 5.26.

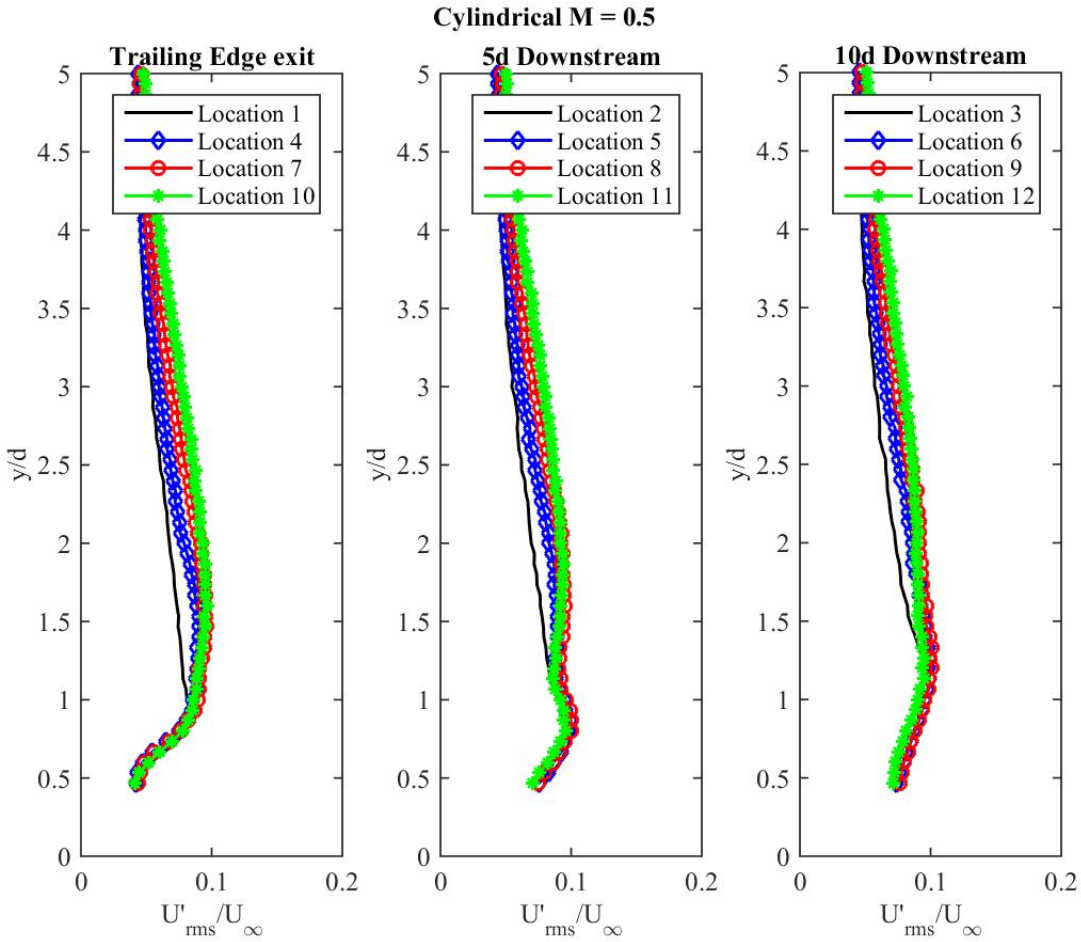

Figure 5.25: Turbulence level profiles at trailing edge, 5d and 10d downstream of each cylindrical jet - M = 0.5

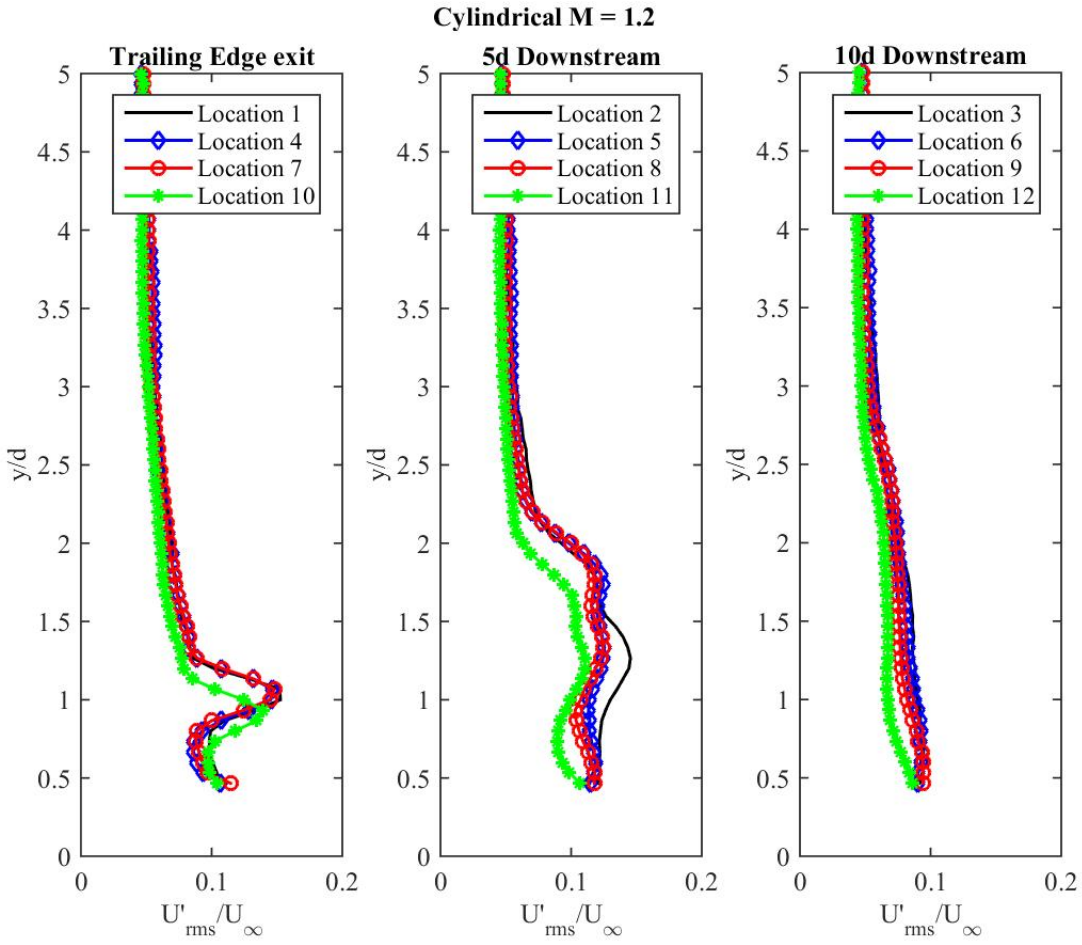

Figure 5.26: Turbulence level profiles at trailing edge, 5d and 10d downstream of each cylindrical jet - M = 1.2

Similar to cylindrical jets, diffuser jets at low blowing ratios (0.5, 0.7) have a fairly steady level of turbulence in the near wall region at all downstream locations as seen in Figure 5.27). At M = 1, and 1.2, near wall turbulence level magnitudes are consistent at the trailing edge but deviate at 5 and 10d downstream. Reduced shear due to increased velocity above the jets in the near wall region causes less turbulence production causing the furthest location downstream to

have the lowest level of turbulence. At M = 1.5 clear differences can be seen even at the trailing edge of the film cooling holes. Reduced turbulence production with each row of blowing is very apparent exemplifying the effects of high blowing ratios with a diffuser configuration. Figure 5.28 below displays the reduction in turbulence level in the near wall region for a blowing ratio of 1.5.

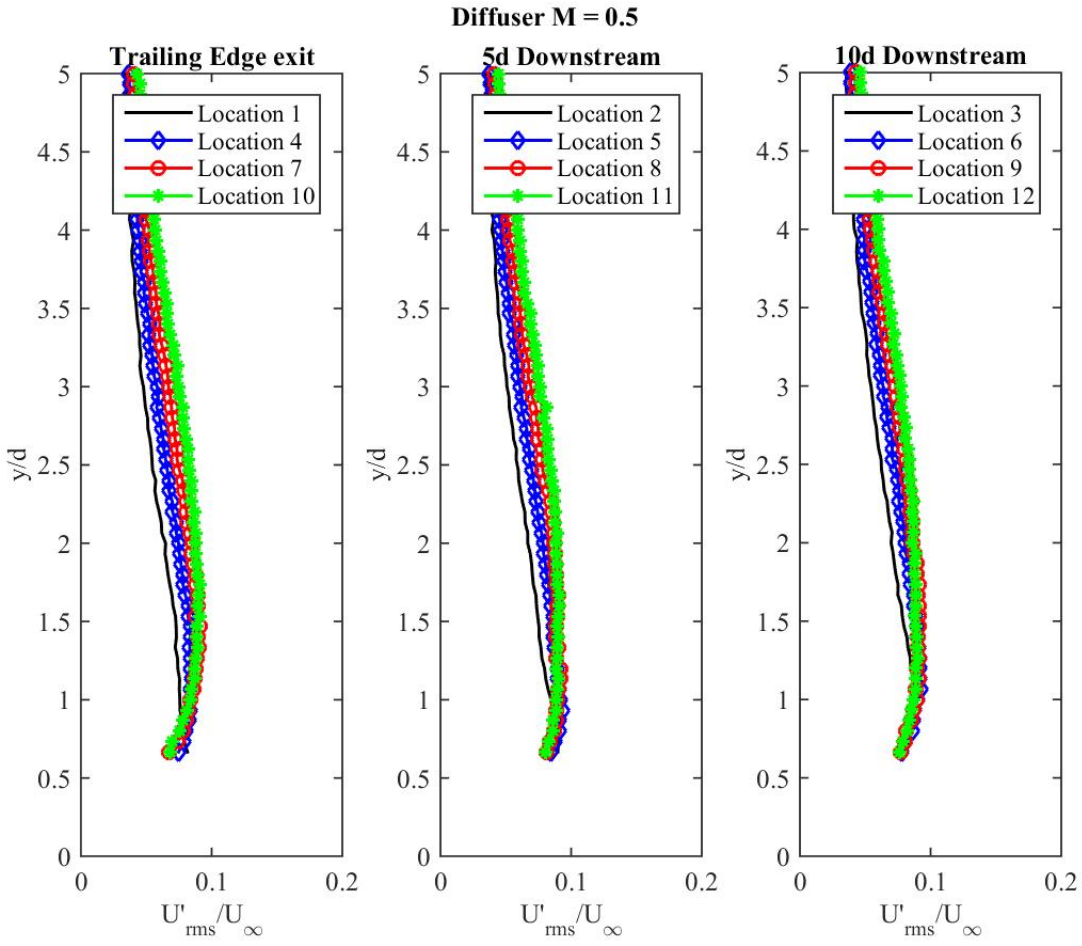

Figure 5.27: Turbulence level profiles at trailing edge, 5d and 10d downstream of each diffuser jet - M = 0.5

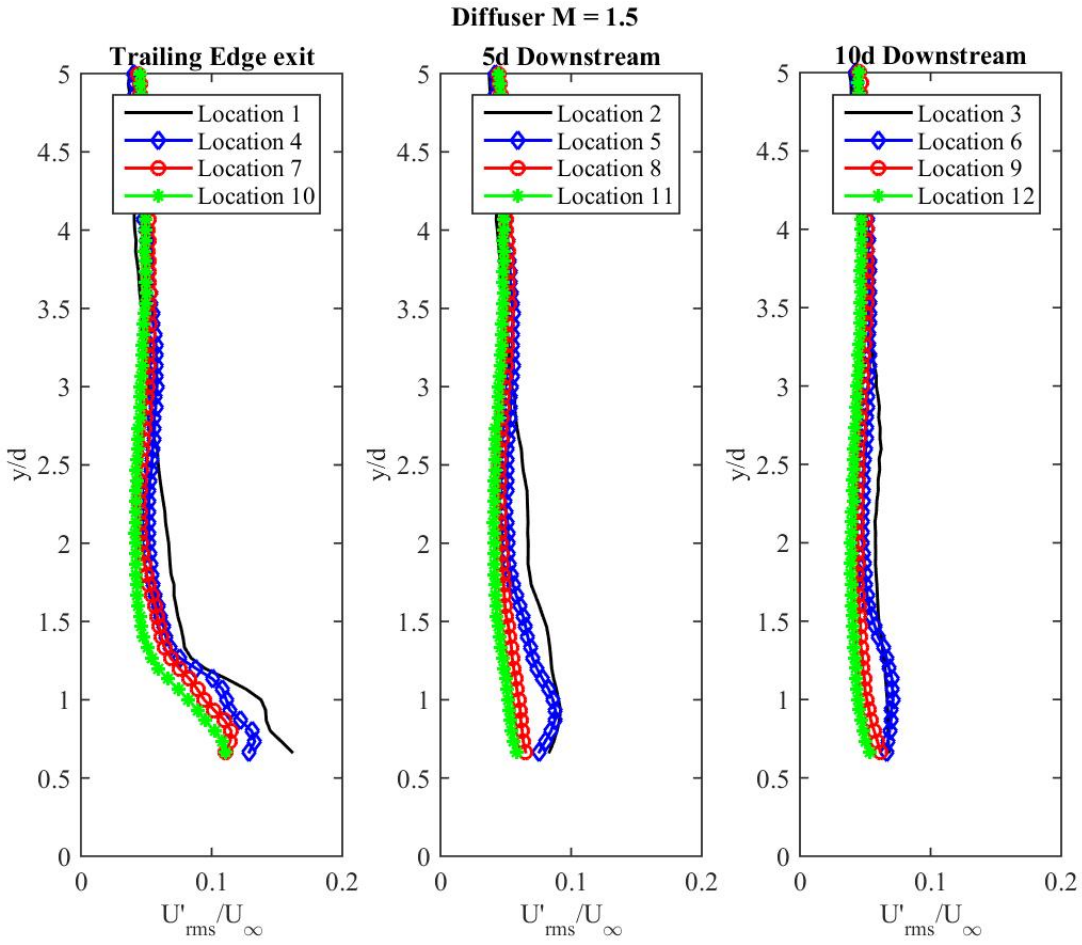

Figure 5.28: Turbulence level profiles at trailing edge, 5d and 10d downstream of each diffuser jet - M = 1.5

Using Matlab's findpeaks feature with a minimum peak prominence of 0.01, the locations of turbulence level peaks on the leading edge side of the jets can be obtained. For cylindrical low blowing ratio cases, where the peaks are easier to identify are plotted in Figure 5.29 below at each location tested. Markers on the x-axis represent hole trailing edges in the array centerline. From this image rising peak locations with each row of blowing shows the effect of film stacking and boundary layer growth where the peaks for M = 0.7 are much higher off the wall compared

with M = 0.3, and 0.5. Diffuser turbulence level peaks at all blowing ratios can be seen in Figure 5.30 below. It is quite evident from the figure that with increasing blowing ratios, particularly at downstream injection sites, the film stacks high off the wall allowing the jets to coalesce and improve its coverage on the surface.

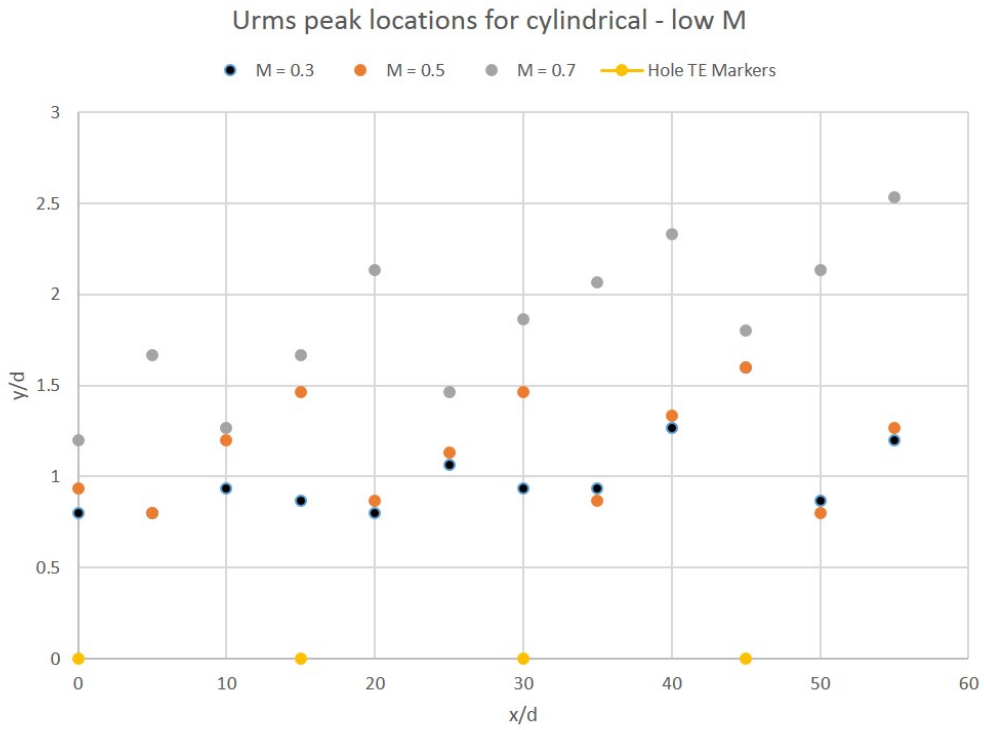

Figure 5.29: Turbulence Level peak locations for low blowing ratio, cylindrical cases

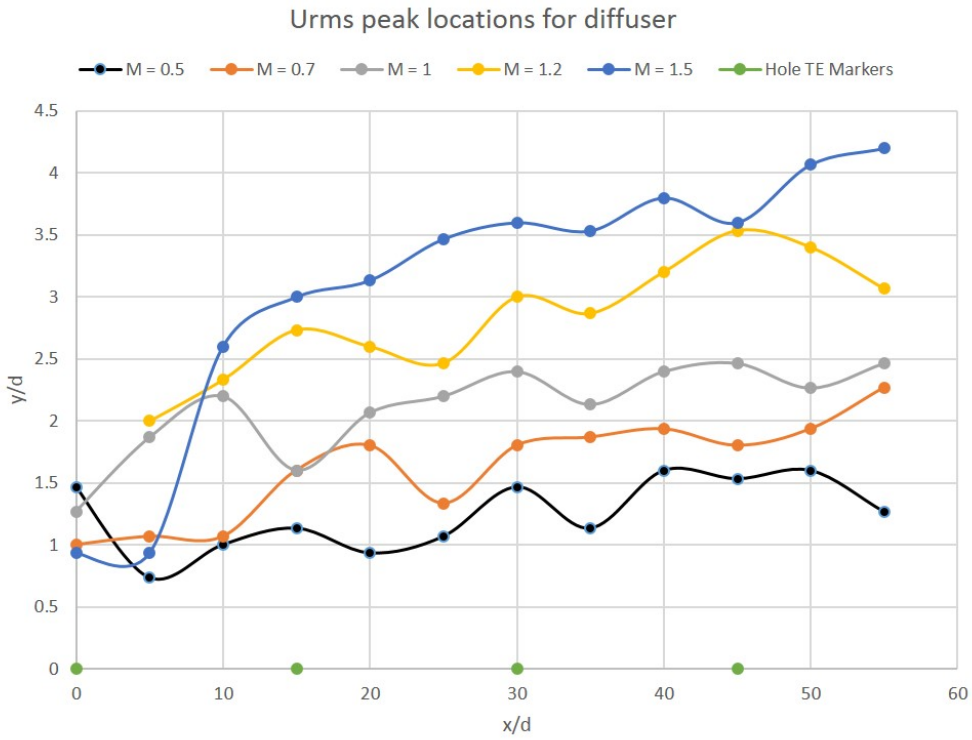

Figure 5.30: Turbulence Level peak locations for low blowing ratio, diffuser cases

Integral Length Scale

This section analyzes the integral length scales (Λ/d) with respect to the location downstream of a jet in the centerline plane. Similar to the sections above, the plots are divided into locations at the trailing edge of each jet, 5d, and 10d downstream. For reference, appendix A contains figures of the cases that are not shown in this section. For the cylindrical array, injection at low blowing ratios of 0.3, 0.5, and 0.7 display integral length scales that remain consistent regardless of location downstream. The example of M = 0.5 case is shown in Figure 5.31 below for ease of reference. M = 0.7 shows smaller integral scales at the trailing edge and 5d downstream as the jets yet their magnitude remains consistent for all four jets indicating little to no propagation of

effects from preceding jets. M = 1 case still shows a consistent trend except for the last jet where the length scales are much lower in the near wall region. M = 1.2 also has consistent trends at downstream locations for jets 1, 2, and 3 in the near wall region but have significant discrepancies at higher wall-normal positions. Integral length scales in this mid-span region reduce with respect to downstream location indicating breakdown of vortices. Jet 4 shows a similar trend as M = 1 at downstream locations increasing credibility and physicality of measurements. Figure A.7 is provided as an example of these high blowing ratio flow phenomena for the cylindrical geometry.

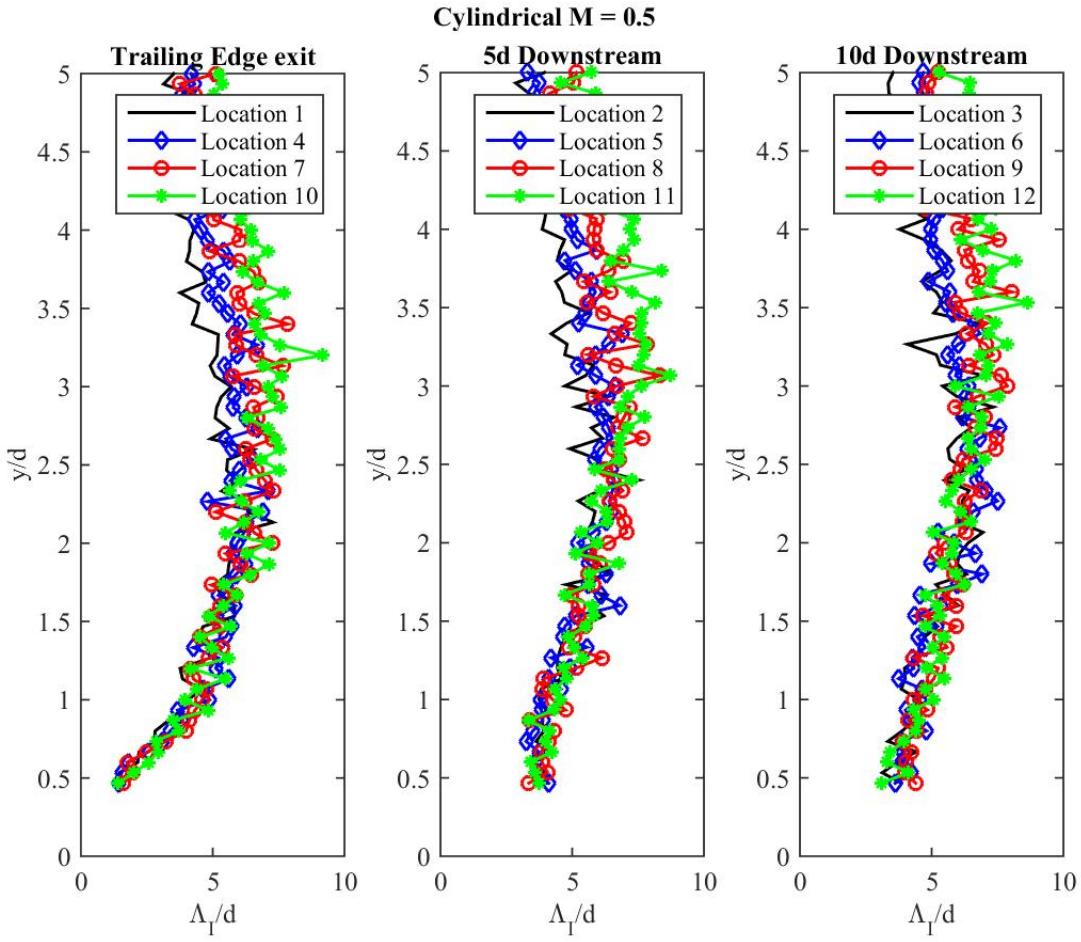

Figure 5.31: Integral length scales at trailing edge, 5d and 10d downstream of each cylindrical jet - M = 0.5

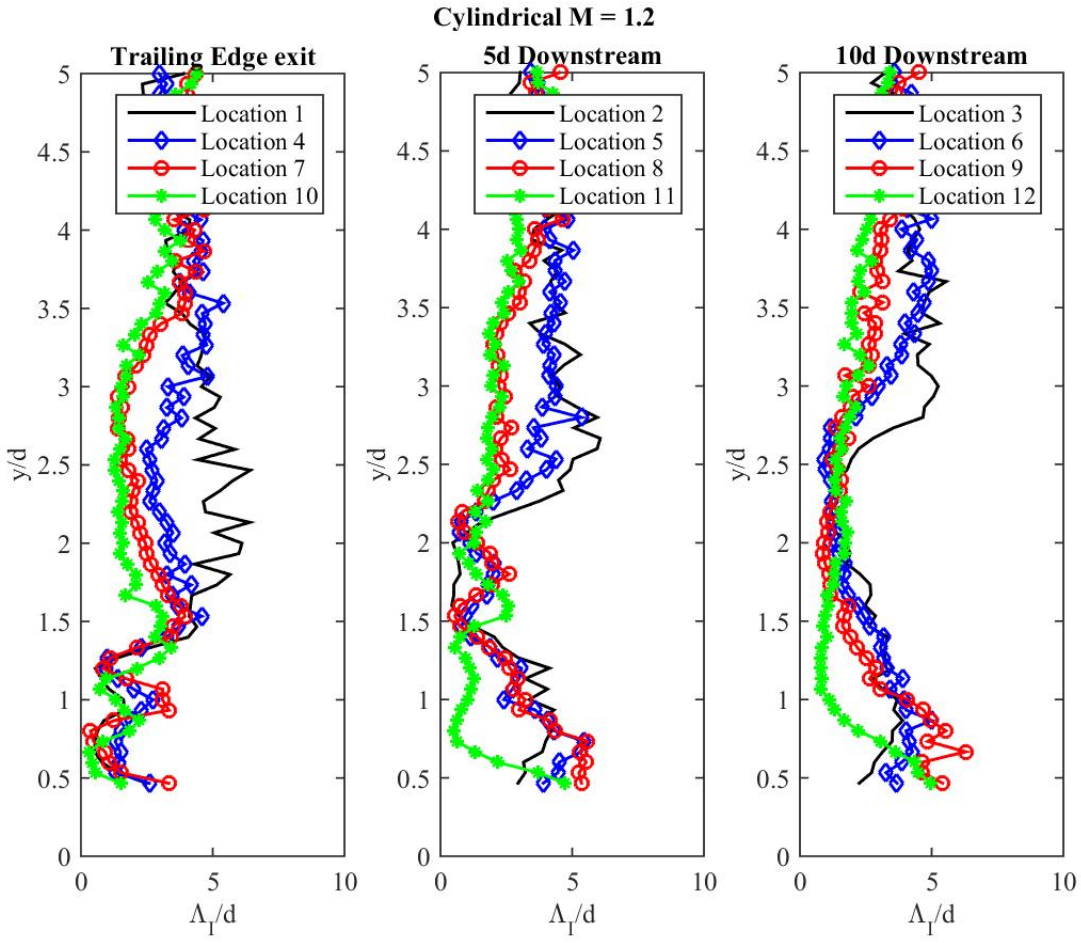

Figure 5.32: Integral length scales at trailing edge, 5d and 10d downstream of each cylindrical jet - M = 1.2

Diffuser jets in the centerline plane display self similarity at all blowing ratios tested except 1.5. The example case of M = 0.5 is shown in Figure 5.33. With increasing blowing ratio, jets tend to have lower integral length scales in the near wall region. At M = 1.5, integral length scales reduce above the jets after the first row of blowing. This can be viewed in Figure 5.34 below.

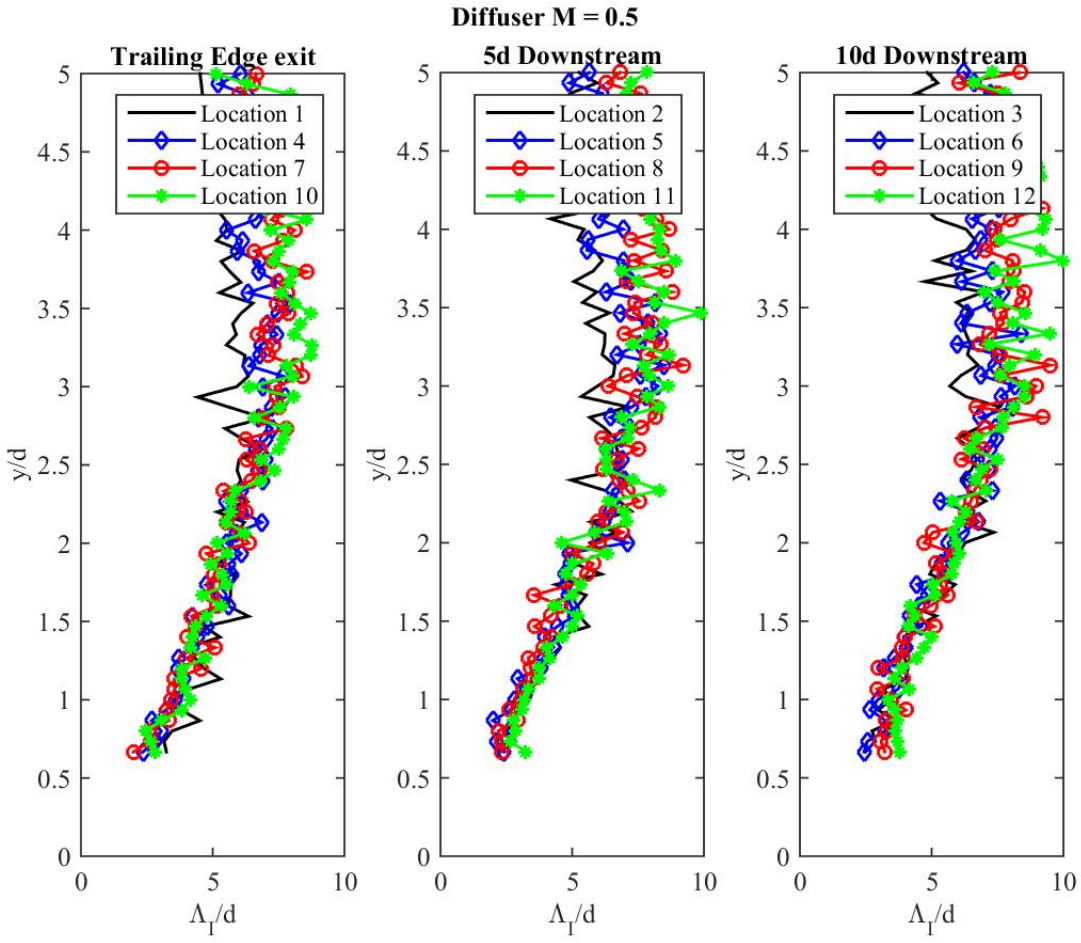

Figure 5.33: Integral length scales at trailing edge, 5d and 10d downstream of each diffuser jet - M = 0.5

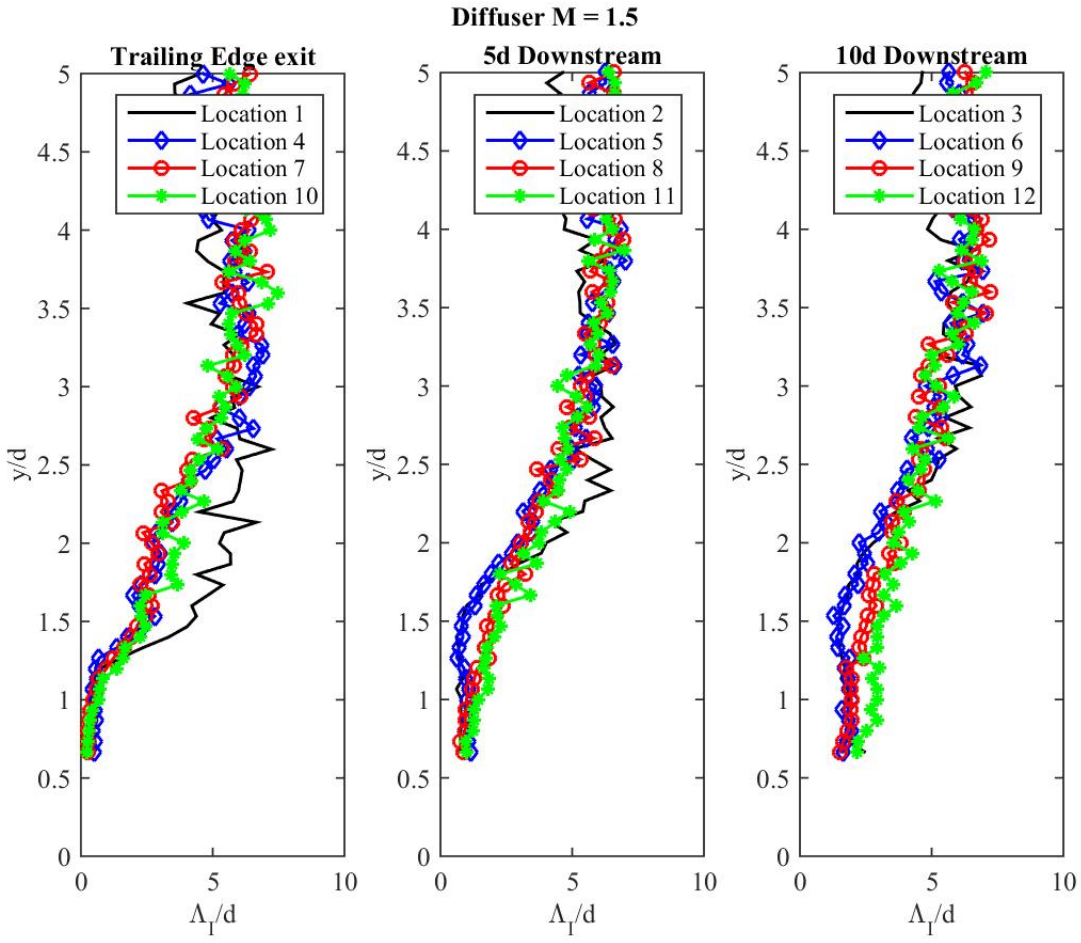

Figure 5.34: Integral length scales at trailing edge, 5d and 10d downstream of each diffuser jet - M = 1.5

Statistical Analysis - Geometry Comparison

The following sections discuss the differences between cylindrical and diffuser geometries at blowing ratios 0.5, 0.7, 1.0, and 1.2. Plots are organized in a 4x3 matrix for convenience of reference and improved understanding of locations. Each row represents a chronological jet ensuing from the array centerline while each column shows measurements at the trailing edge of a film

cooling hole, 5d, and 10d downstream. For reference, mean velocity, U'_{rms} and integral length scale line plot comparisons can be found in appendix B at each of the blowing ratios. Again, wall-normal position is non-dimensionalized by the hole diameter while $\bar{U}$ and U'_{rms} are non-dimensionalized by freestream velocity.

Average Effective Velocity

At a low blowing ratio of 0.5, mean velocity profiles for jet 1 are almost identical for both geometries. Further downstream, diffuser jets 2 through 4 are noticed to have significantly lower velocities thus causing the boundary layer to be dragged. While a similar trend is noticed for diffuser jets at blowing ratio 0.7, cylindrical jets at this blowing ratio begin to show signs of lift off already. Clear jet profiles are visible at the trailing edge of each hole but lose an momentum due to shear with downstream propagation. At M = 1, diffuser jet profiles begin to be visible at the trailing edge of the holes but are dampened back down by 5d downstream. The dragging of the boundary layer persists even at the high blowing ratio of 1 and 1.2. Cylindrical jets show clear jet detachment with jet core peaks dampening out by 10d downstream for M = 1. Cylindrical jets at the highest blowing ratio of 1.2 still retain jet identity even 10d downstream. Diffuser jets at high blowing ratios still show signs of attachment and reduced peak mean velocity magnitudes at the trailing edge with each row of blowing. This contributes to the drastically improved film cooling effectiveness at downstream locations observed for diffuser geometries at high blowing ratios compared to cylindrical [28]. Figure 5.35 below demonstrates the vast differences in mean velocity between injecting through diffuser shaped holes compared to cylindrical shaped holes at a blowing ratio of 1.2.

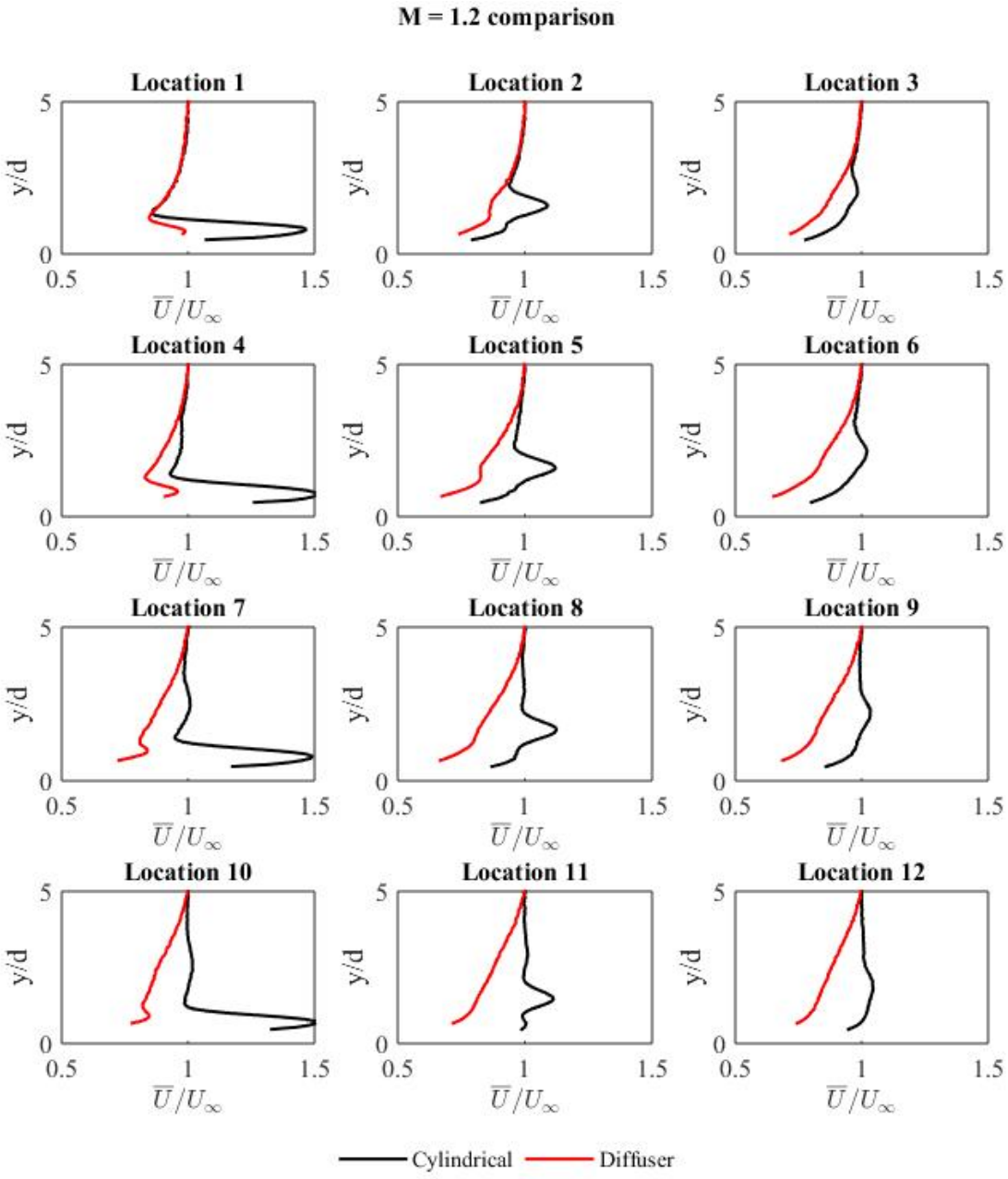

Figure 5.35: Average velocity for both geometries - M = 1.2

To further exemplify the similarities and differences between the effective mean velocity

profiles between cylindrical and diffuser jets, profiles at locations 1 and 12 specifically have been juxtaposed in Figure 5.36. Diffuser geometries show reduction in the peak magnitudes of velocity compared with that of cylindrical allowing much better adhesion to the surface at all M. Boundary layer thickness is also seen to increase for diffuser cases by the last testing location compared with that of cylindrical. While the ”dragging” effect of the boundary layer was observed for both geometries, the concavity shift is much higher in diffuser cases. Finally, the increased magnitudes of velocities above the jets for both cylindrical and diffuser jets can be seen very clearly at location 12 for high M.

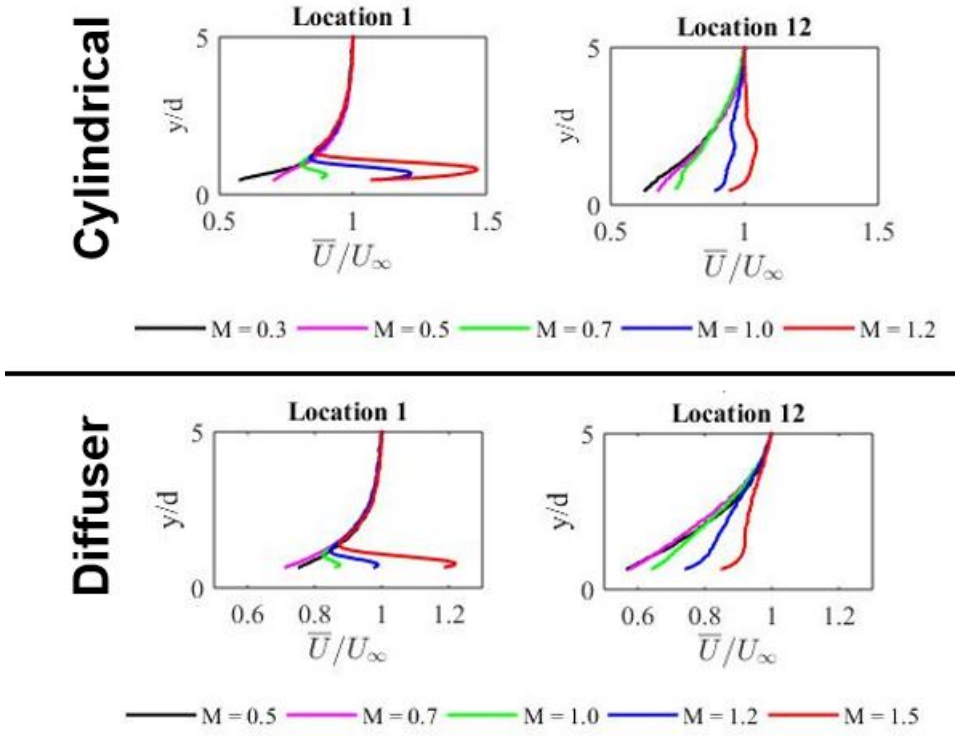

Figure 5.36: Average velocities for cylindrical and diffuser, locations 1 and 12

Turbulence Level

Turbulence level profiles of diffuser vs. cylindrical geometries at the same blowing ratio vary quite significantly as well. U'_{rms} profiles at M = 0.5 has similar magnitude and peaks for both geometries indicating a very comparable flowfield in terms of turbulence production. A slight development of a double shear layer is apparent for the cylindrical geometry at 5d downstream of all but the first jet. At M = 0.7, clear discrepancies arise where cylindrical jets lift-off the surface while diffuser jets do not. Turbulence level magnitudes are similar at all locations indicating that the boundary layer is very comparable for both geometries. By M = 1, diffuser and cylindrical turbulence levels look entirely different throughout the flowfield. With jet lift-off spikes in turbulence production is seen in low wall-normal locations as mainstream fluid is entrained below the jets by means of the counter rotating vortex pair. Lower levels of turbulence are seen in the boundary layer just above the jets with every row of blowing as velocity gradients are minimized. Diffuser jets show significantly lower levels of turbulence in the near wall region. Jets 1 and 2 show signs of lift-off displaying dual shear layers 5d downstream. Jets 3 and 4 display very low turbulence levels 5d and 10d downstream indicating attachment of these jets. Peaks in turbulence level rise in wall-normal position from TE to 10d downstream of each jet indicating spreading of jets. M = 1.2 shows similar trends compared with M = 1 where cylindrical jets blow off penetrating deep into the freestream raising the turbulence levels above that of all other cases by 5d downstream. Diffuser jets show severely reducing turbulence production near the wall with every row of blowing. Figure 5.37 below is displayed as an example of the discrepancies in turbulence levels at M = 1.2.

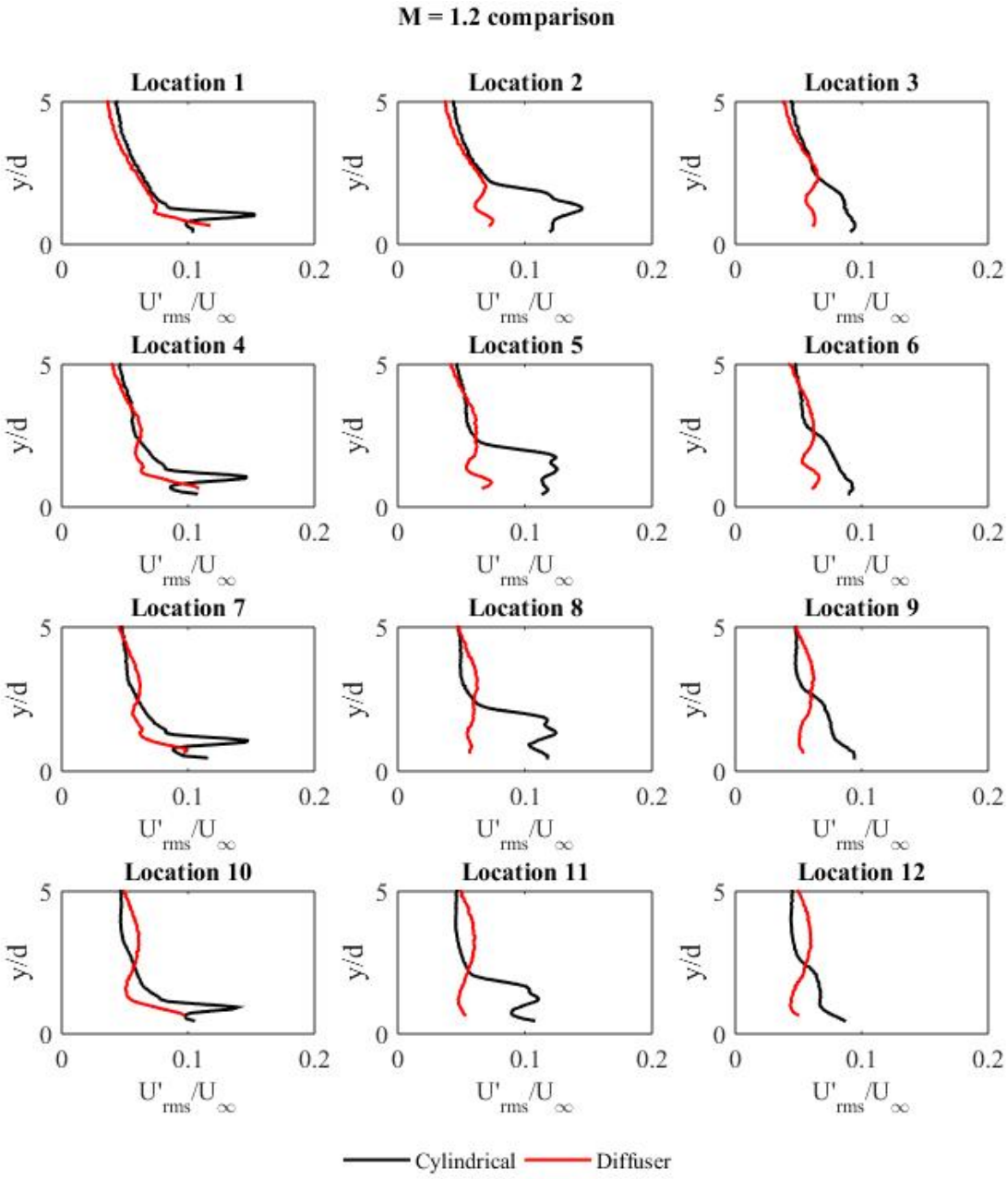

Figure 5.37: Turbulence level for both geometries - M = 1.2

To look further into the differences of turbulence levels of the two geometries, Locations 5,

8, and 11 at low blowing ratios have been extracted and are displayed in Figure 5.38. Diffuser geometries show rising shear layers with peak locations at higher y/d locations with each row of blowing. This is due to the stacking of film and coalescing effects not only from preceding jets but also due to potential out of plane effects. Cylindrical jets on the other hand do not show rising shear layers at these low blowing ratios tested. A second peak, however, is noticed at a blowing ratio of 0.5 for cylindrical implying the onset of jet lift-off. Turbulence levels of higher blowing ratios at locations 2, 5, 8, and 11 have been extracted for each geometry and plotted in figure 5.39. The dual peaks which are observed 5d downstream of each cylindrical jet is only observed for the first two diffuser jets. Only single peaks are apparent for jets 3 and 4. With the increased adherence of the downstream jets to the surface, fluid is not entrained under the jets and the jets are only sheared from the interaction with the mainstream gas. For both geometries, a reduction in the turbulence levels is observed at high M with each row of blowing. This is most apparent for the highest blowing ratio case at location 11 compared with location 2 for each geometry.

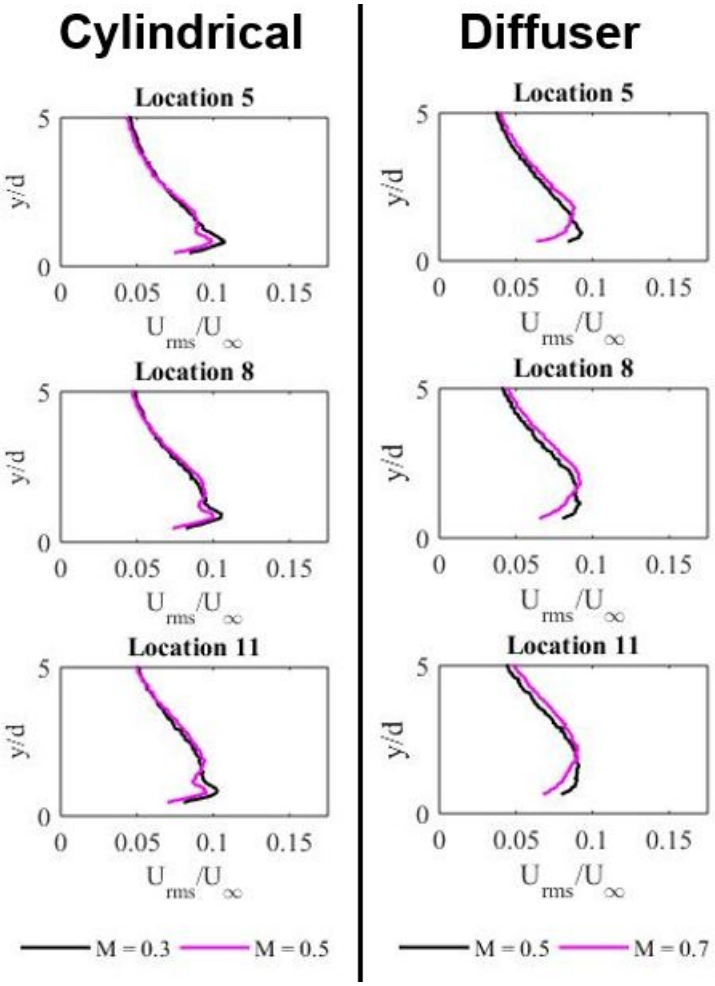

Figure 5.38: Turbulence levels for both geometries at low blowing ratios, locs 5, 8, and 11

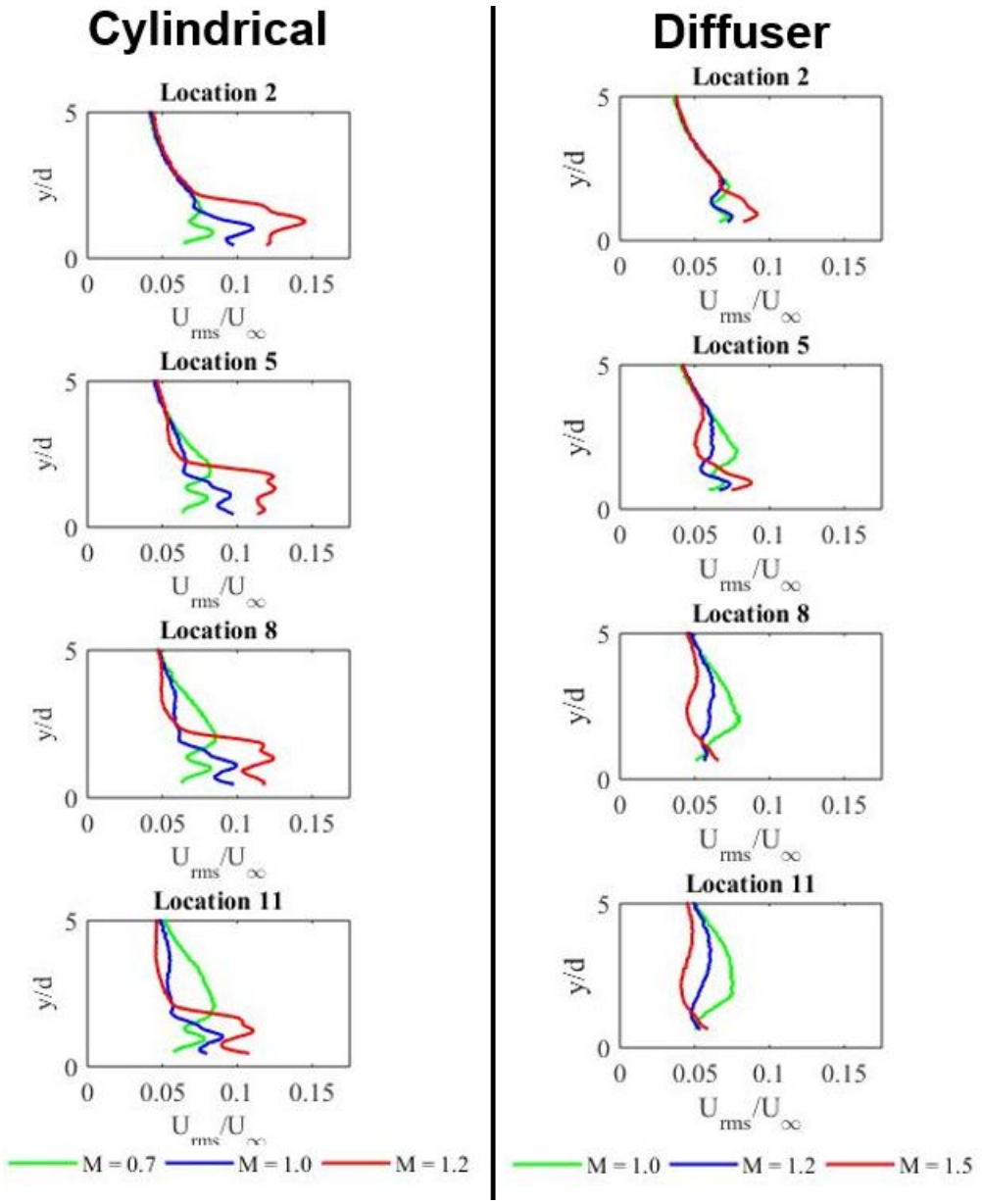

Figure 5.39: Turbulence levels for both geometries at low blowing ratios, locs 2, 5, 8, and 11

Integral Length Scale

Integral Length Scales in the near wall region for both cylindrical and diffuser geometries have similar magnitudes at a low blowing ratio of 0.5. At higher elevations in the boundary layer, slightly longer correlations are seen for the diffuser case. At M = 0.7, near wall correlations for diffuser are shorter than that of cylindrical. As the cylindrical jets lift off, a kind of wake is generated below the jet resulting in longer correlations whereas diffuser jets still have not detached at this blowing ratio. At M = 1.0 and 1.2, integral length scales of cylindrical jets show very low correlations within the shear layers that bound the penetrating jet. Diffuser geometry produces integral length scales that are very small in the near wall region. This is perhaps due to the coherence of the jet and lack of turbulence in this region. For reference, Figure 5.40 is shown below at a blowing ratio of 1.2.

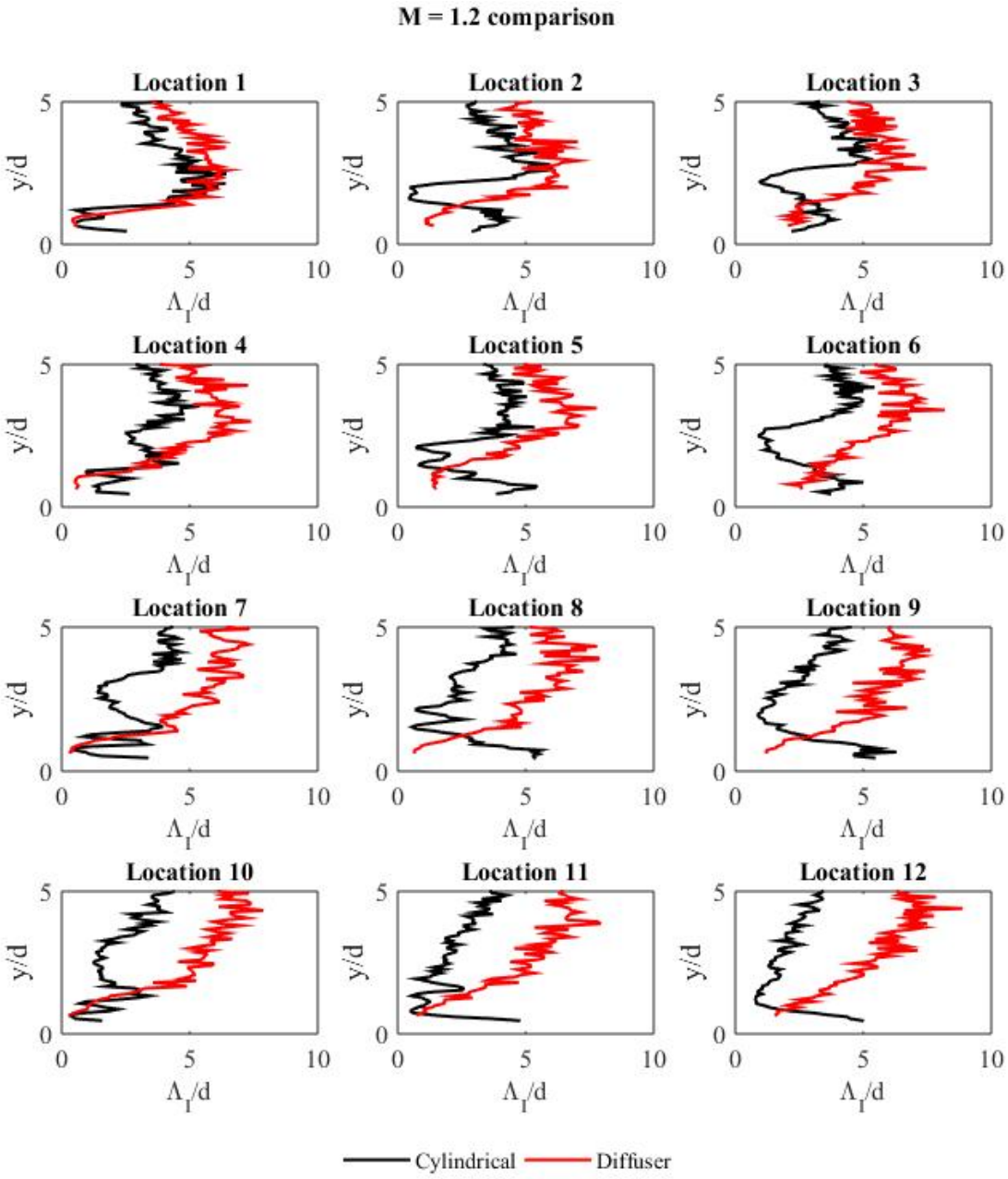

Figure 5.40: Integral Length scales for both geometries - M = 1.2

Effectiveness

Film cooling surface effectiveness measurements were previously conducted by Natsui on the exact same test setup. This gives a unique opportunity to directly compare the findings of this study with those found in [24] and [28]. All surface effectiveness measurements found in this section are obtained from these publications. While the test setup, geometries are almost identical, unfortunately the density ratio used in these publications is 1.67 as opposed to the density ratio of 1 used in the present study. As a result, a density gradient exists in the flowfield where effectiveness measurements have been taken. In order to bridge the gap between the two studies, effectiveness measurements with DR = 1 should be conducted. This would solidify the findings of this document as well as develop a density ratio investigation of the flow field at this shallow angle. The discussion about effectiveness in this section is more of a conjecture and should therefore be taken very loosely, until further analysis can be conducted. The coordinate system of the film cooling effectiveness measurements is also different where the first row hole axis breakout point is considered the origin. The present study uses the trailing edge of the same hole as the global zero.

Figures 5.41 to 5.45 show surface effectiveness measurements for coolant injecting out of a cylindrical array. Low blowing ratio cases of 0.3 and 0.475 show short film traces with increasing streamwise propagation for M = 0.475. Coolant jets are attached for both of these cases and still in the mass addition regime. As per the findings of the present study, at low blowing ratios, the jet core velocities are low and comparable to the local velocity of the boundary layer at injection. Elevated velocities are seen at the trailing edge of each jet but relax by 5d downstream for M = 0.5. Turbulence levels peak in the shear layer above the jet and are higher for the lowest blowing ratio case which. These high turbulence levels coupled with low momentum coolant causes these traces to have short downstream propagation. Low blowing ratio cases were also shown to have short integral length scales near the wall indicating little to no momentum transport in this region.

Higher blowing ratios were shown to have a very clear jet core with high streamwise velocities below the jets. This typically results in much lower effectiveness at the near wall as mainstream fluid is entrained towards the wall. Jet cores were also shown to be slightly closer to the wall at the furthest row downstream yet obviously detached from the surface providing decreased coverage with increasing blowing ratio. The velocity profile above the jets peeled away from that of the boundary layer showing higher velocity fluid propagating along with the jets to downstream rows of injection causing jets to bend slightly towards the surface far downstream. At M = 1.2, shearing caused reduced jet core peaks by 5d downstream and severely dampened jet cores by 10d downstream. Jet cores being so high off the wall at M = 1.5 explain why the surface effectiveness is so poor for this configuration. High blowing ratio cylindrical jets were also shown to have two distinct peaks in turbulence level which shear the jet and promote mixing of the mainstream fluid in the near wall region. Much larger integral length scales were calculated in the near wall region for these blowing ratios signifying high levels of momentum transport.

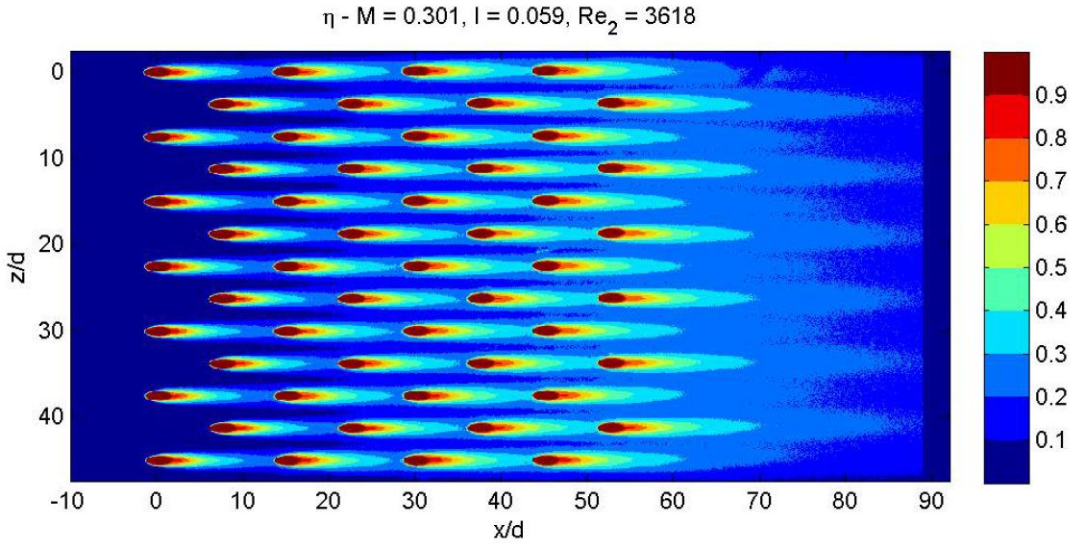

Figure 5.41: Spatially resolved surface effectiveness for cylindrical geometry - M = 0.3, DR 1.67 [24]

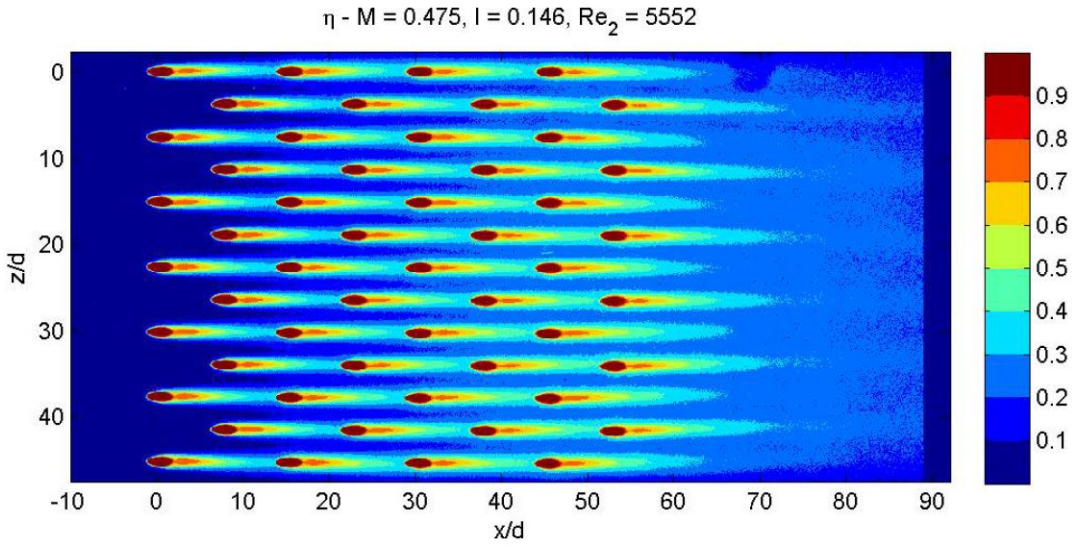

Figure 5.42: Spatially resolved surface effectiveness for cylindrical geometry - M = 0.475, DR 1.67 [24]

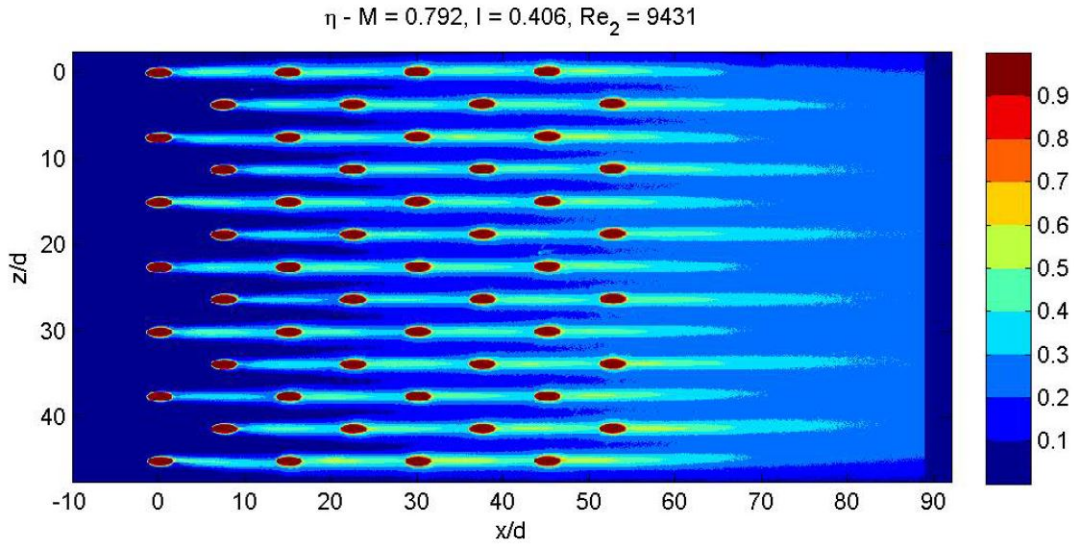

Figure 5.43: Spatially resolved surface effectiveness for cylindrical geometry - M = 0.792, DR 1.67 [24]

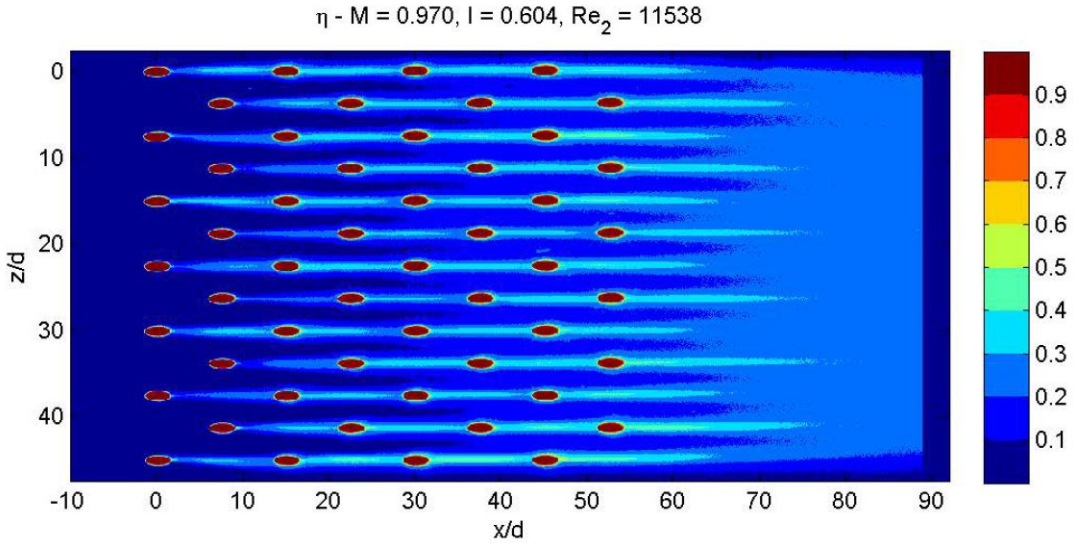

Figure 5.44: Spatially resolved surface effectiveness for cylindrical geometry - M = 0.970, DR 1.67 [24]

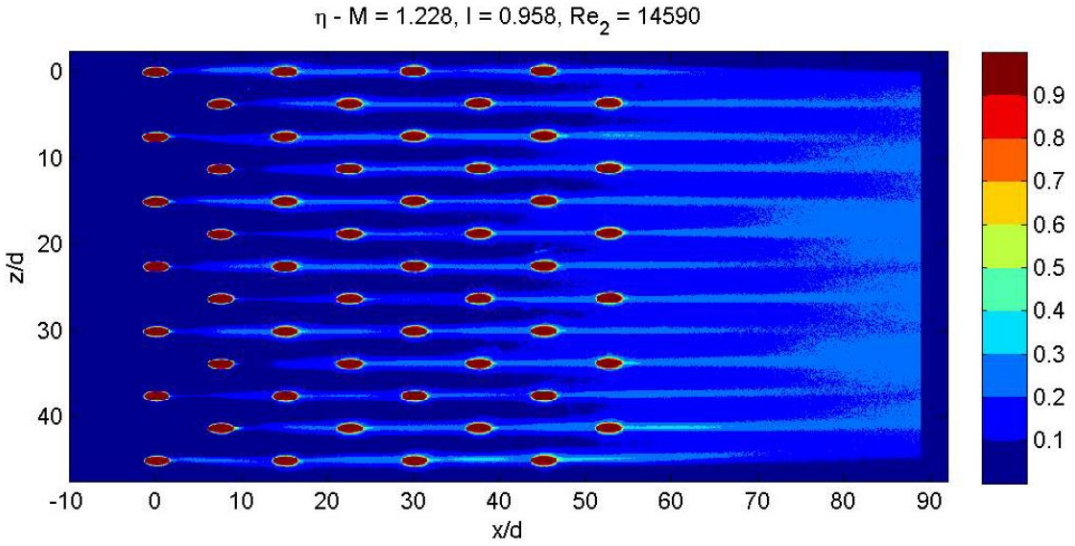

Figure 5.45: Spatially resolved surface effectiveness for cylindrical geometry - M = 1.228, DR 1.67 [24]

Figures 5.46 to 5.48 show surface effectiveness measurements for the diffuser geometry. As discussed above, a disclaimer should be made that these measurements were made with a density

ratio of 1.67 and that the discussion is more of a conjecture until further evidence can be gathered with respect to surface effectiveness measurements at a density ratio of 1.

The retarded boundary layer effect discussed in this paper for injection through diffuser shaped holes was shown to change the boundary layer profile significantly at downstream locations. This effect was due to fluid with very low velocity being injected at elevations comparably far above the viscous sublayer causing higher levels of shear with every row of blowing. At low blowing ratios jets are sped up by 10d downstream but not enough to recover the original boundary layer profile so succeeding jets are influenced, compounding the effect. Shear layers are observed to diffuse as the turbulence level peaks grow in width. The flowfield measurements corroborate the findings by Natsui even with the density difference as downstream rows reap the benefit of the altered boundary layer. Lower integral length scales also provide evidence of jet attachment at these low blowing ratios. Unfortunately since jet cores are not visible for low blowing ratios, it is difficult to discern how far downstream the jets truly propagate without corroborating surface effectiveness measurements at this density ratio.

Even though the alteration of boundary layer profile is clearly evident at low blowing ratios, it is still apparent in higher blowing ratio cases. At M = 1, $\bar{U}$ peaks decrease in magnitude after the first row of blowing. This is due to higher velocity fluid propagating to downstream jets. These downstream jets now inject into a faster moving fluid which acts as increased resistance. The jets relax by 5d downstream of each row of injection to profiles similar to that of low blowing ratios. Turbulence level profiles displayed jet cores and shear layers at locations 5 and 10d downstream of jets 1 and 2 but not 3 and 4. This is indicative of a reduction of velocity gradients at downstream locations and injection of jets 1 and 2 deeper into the boundary layer.

At even higher M (blowing ratio of 1.5) mean velocity profiles retained jet identity even 10d downstream which propagated downstream influencing succeeding jets. Higher local convec-

tive velocities coupled with low $\bar{U}$ gradients allows succeeding jets to be propagated much further downstream. In addition, U'_{rms} profiles show large drops in magnitude near the wall noticed as early as the second jet trailing edge. Low turbulence levels in these regions allows jets to propagate without shearing away much fluid. These phenomena all contribute to the reduced film cooling effectiveness for the first few rows but enhanced coverage and downstream propagation for succeeding rows of blowing. Quite interestingly, integral length scales for diffuser jets all show short lengthscales in the near wall region indicating very low momentum and energy transport. Higher blowing ratios tend to show short integral length scales further away from the wall probably due to interactions between mainstream and jet vortices below the jets. This is noticed only for the first two jets which corroborate the U'_{rms} findings.

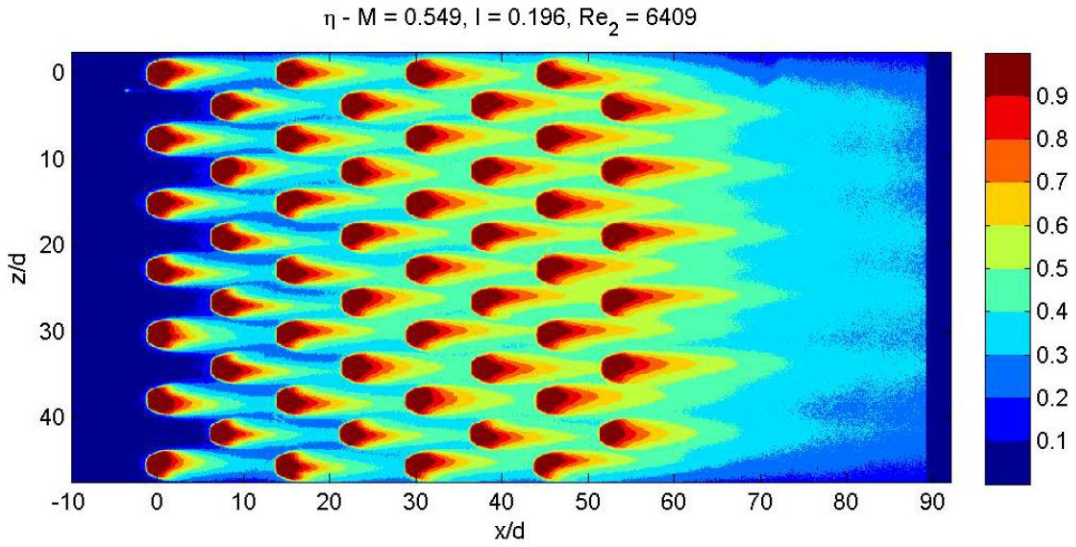

Figure 5.46: Spatially resolved surface effectiveness for cylindrical geometry - M = 0.549, DR 1.67 [24]

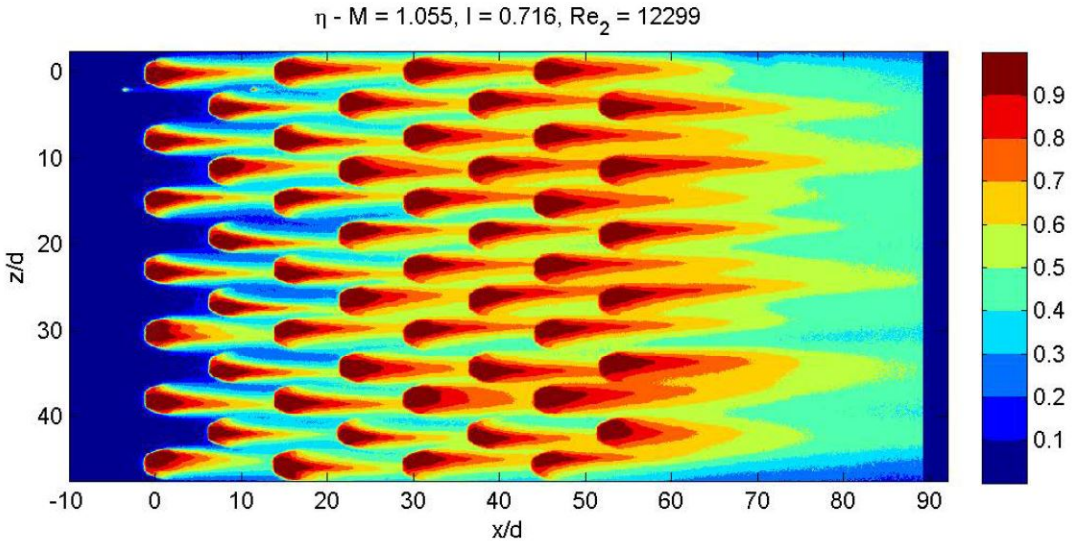

Figure 5.47: Spatially resolved surface effectiveness for cylindrical geometry - M = 1.055, DR 1.67 [24]

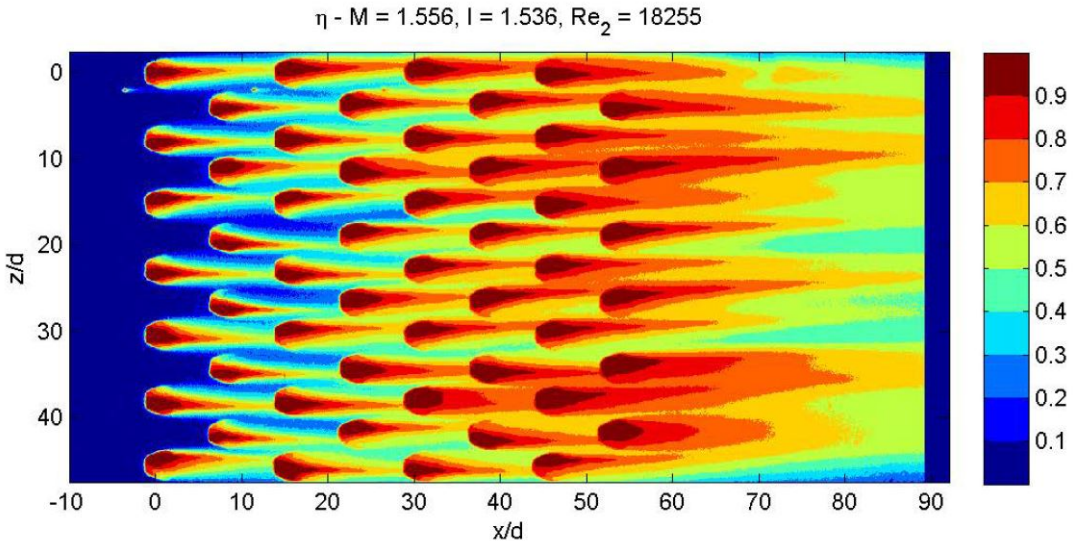

Figure 5.48: Spatially resolved surface effectiveness for cylindrical geometry - M = 1.556, DR 1.67 [24]

CHAPTER 6: CONCLUSION

A detailed analysis has been conducted on the flowfield emanating from multi-row film cooling arrays of cylindrical and diffuser shaped holes. The novelty of the study is the rarity of publications in literature concerning multi-row film cooling holes inclined at 20◦. Even more rare is the characterization of flowfield above diffuser shaped holes.

The objective of the current study was to use hotwire anemometry as a tool to conduct 1D time-resolved turbulent measurements on the flow field of staggered multi-row film cooling arrays with cylindrical and diffuser shaped holes. The study investigated the flow field to determine why the performance of diffuser shaped jets was enhanced even at high blowing ratios. In addition, blowing ratio effects and flowfield discrepancies at set downstream locations in centerline array centerline plane was also investigated.

The experiments were conducted on an open-loop wind tunnel for blowing ratios in the range of 0.3 to 1.5 at a density ratio of 1. Boundary layer measurements were taken at 12 locations at the array centerline to obtain mean velocity, turbulence level, and integral length scales. Measurements were also taken at a location upstream of the array to characterize the incoming boundary layer, estimate the wall normal position of the probe in comparison with the log-law in wall co-ordinates, and to provide inlet conditions for computational work in the future.

Mean streamwise velocity profiles were found to scale with blowing ratio for both geometries. A strong dependence of turbulence levels on velocity gradients between jets and the local fluid was also noticed. For cylindrical jets, attached cases displayed lower integral length scales in the near wall region compared with higher blowing ratio cases. This was found to be due to entrainment of mainstream fluid showing increased momentum transport below the jets. Diffuser cases at all blowing ratios tested do not show increased length scales near the wall demonstrating

their enhanced surface coverage. Row-to-row discrepancies in mean velocity and turbulence level are only evident at extremely high blowing cases for cylindrical, but show significant deviations for diffuser cases at all blowing ratios.

Unlike the cylindrical cases, jets from diffuser shaped holes, due to their extremely low injecting velocities, dragged the boundary layer with each row of blowing. Increased velocity gradients create a rise in peak turbulence levels at downstream locations. At high blowing ratios however, faster moving fluid, due to injection, at lower elevations acts as a shield for downstream jets allowing significantly further propagation downstream. Near the wall, low magnitude integral length scales are noticed for diffuser jets indicating low momentum transport in this region.

The results showed good agreement with effectiveness measurements of a previous study at a higher density ratio. However, to accurately draw the comparison, effectiveness measurements should be conducted at a density ratio of 1. A foreign gas such as N_2 can be used as the coolant media to obtain a density ratio around 1 for PSP testing. Developing trustworthy PIV diagnostics on the same geometry and comparing them to the present hotwire findings would help validate the testing procedures, give credibility to both studies and widen the scope of turbulence measurements to 2 and 3 dimensions. Computational work can also be conducted to back-up the flow phenomena found in the present study.

APPENDIX A: LOCATION COMPARISON

Location comparison - cylindrical

Average effective velocity

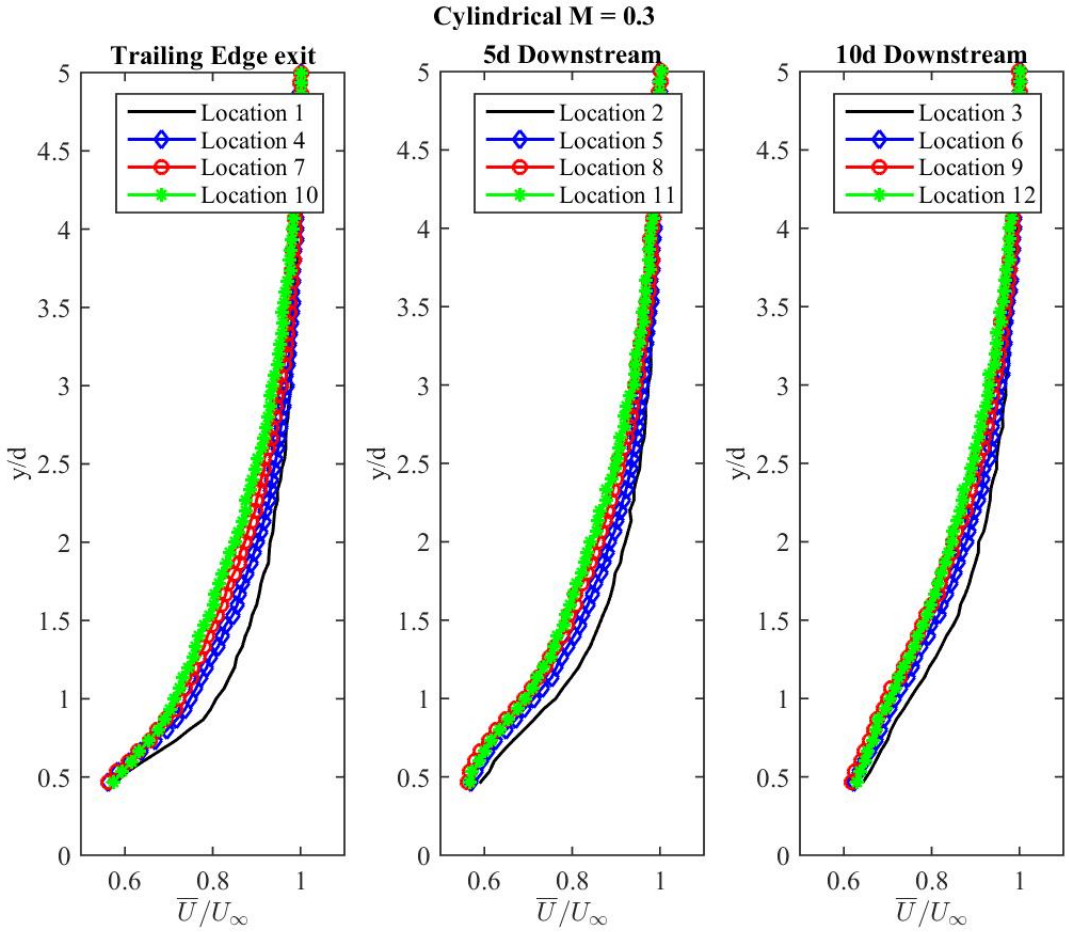

Figure A.1: Average velocity at trailing edge, 5d and 10d downstream of each cylindrical jet, M = 0.3

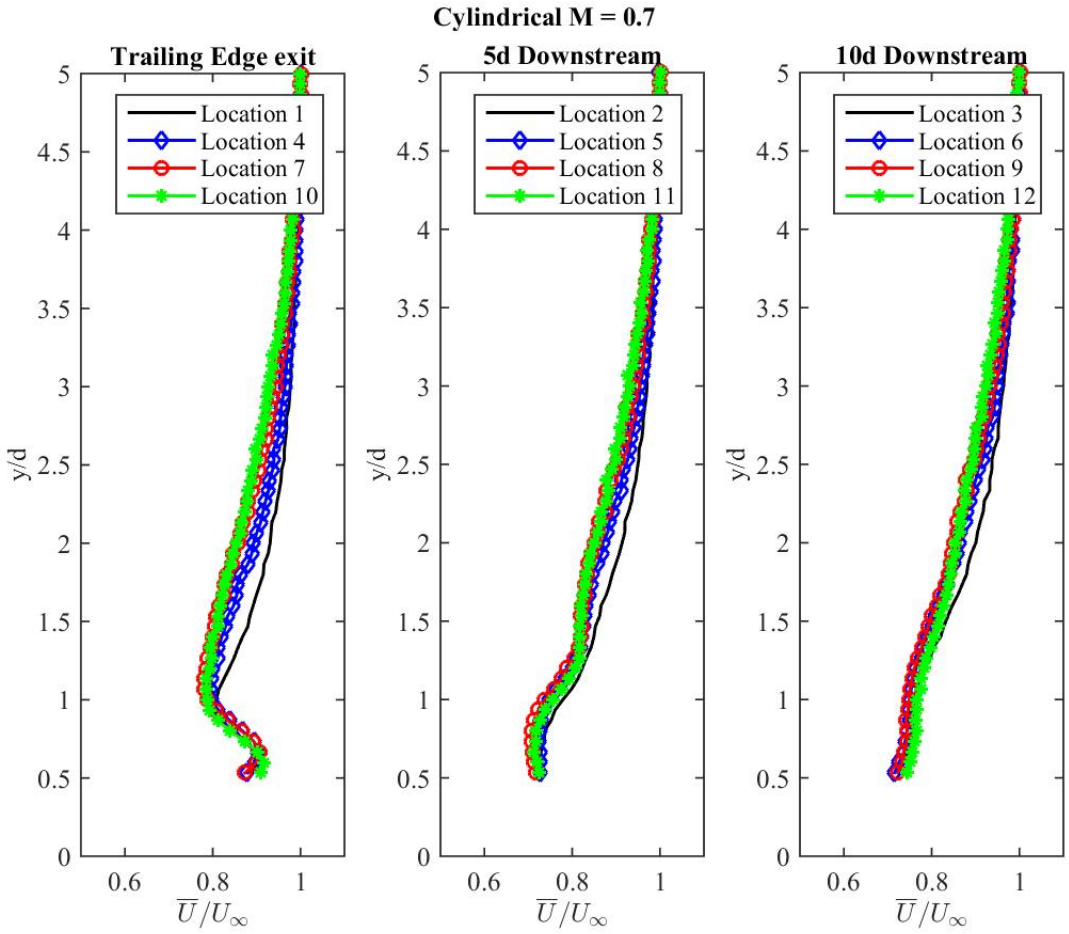

Figure A.2: Average velocity at trailing edge, 5d and 10d downstream of each cylindrical jet, M = 0.7

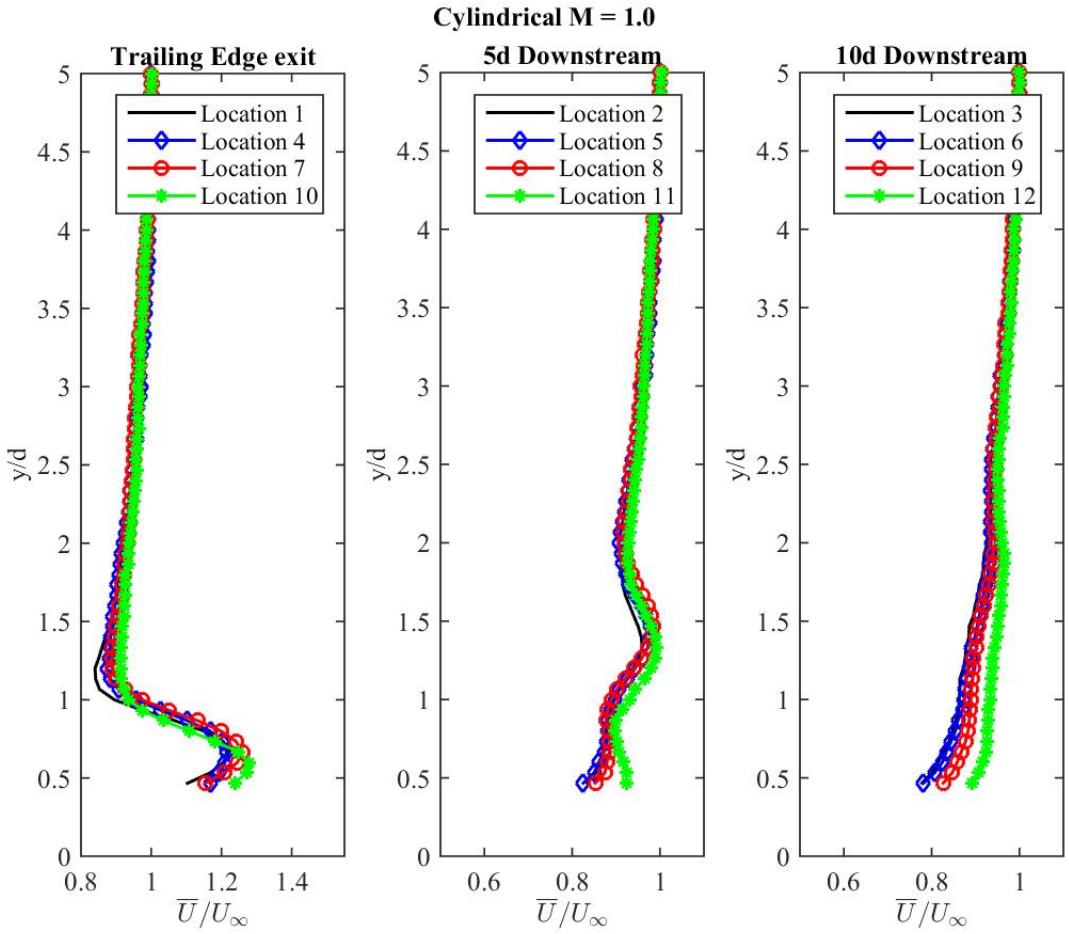

Figure A.3: Average velocity at trailing edge, 5d and 10d downstream of each cylindrical jet, M = 1

Turbulence Level

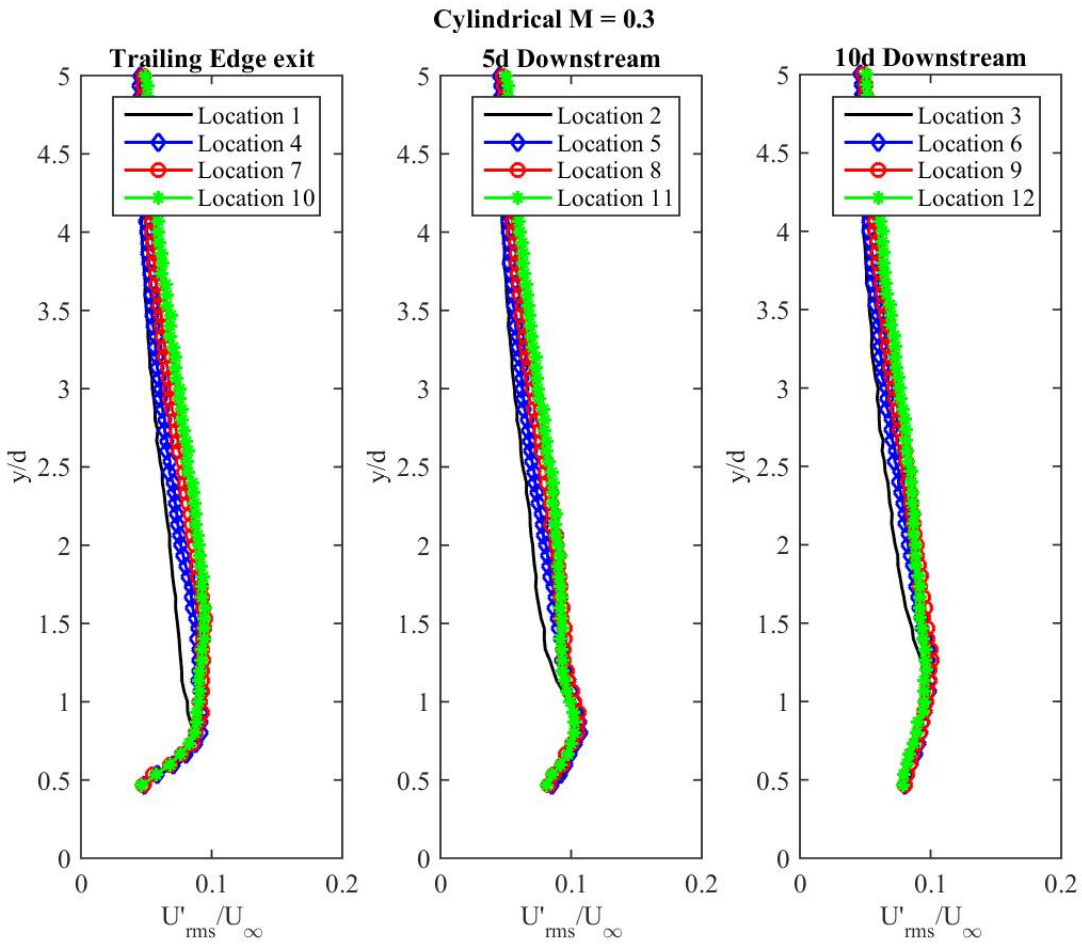

Figure A.4: Turbulence level at trailing edge, 5d and 10d downstream of each cylindrical jet, M = 0.3

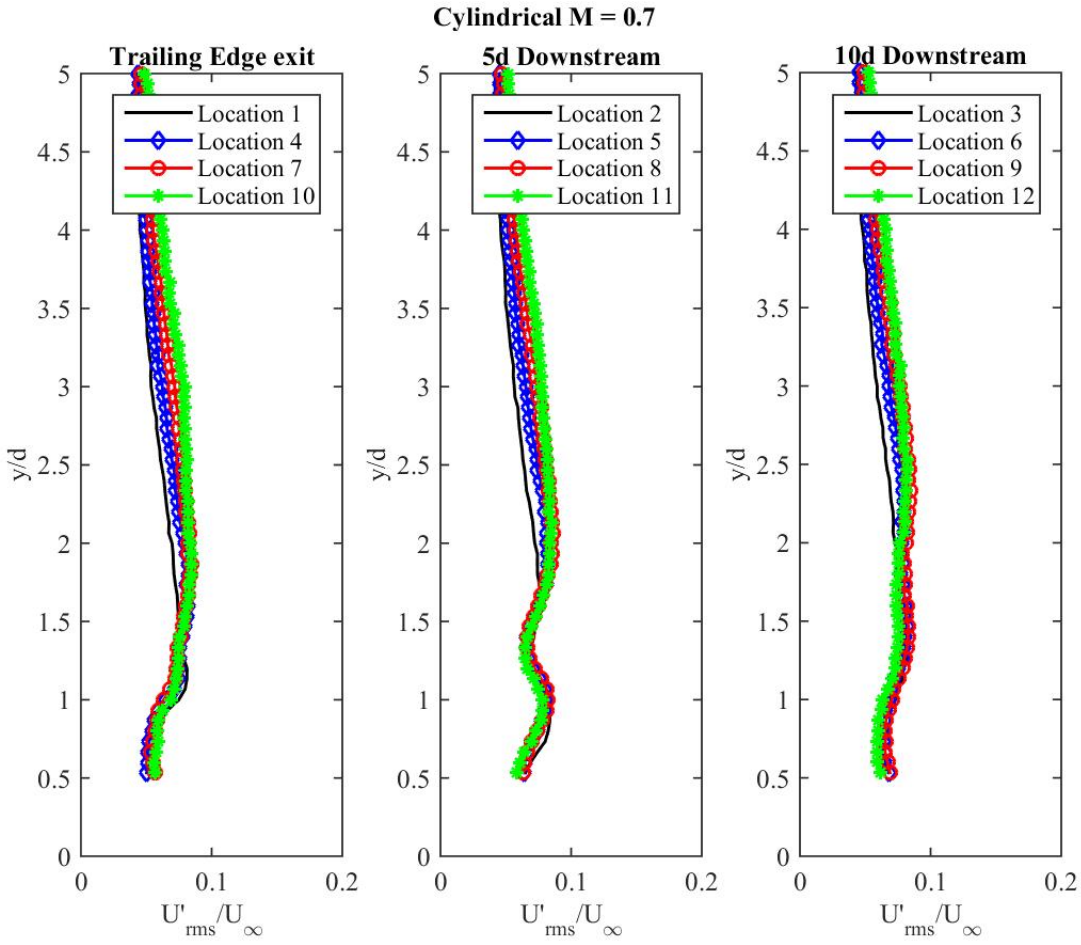

Figure A.5: Turbulence level at trailing edge, 5d and 10d downstream of each cylindrical jet, M = 0.7

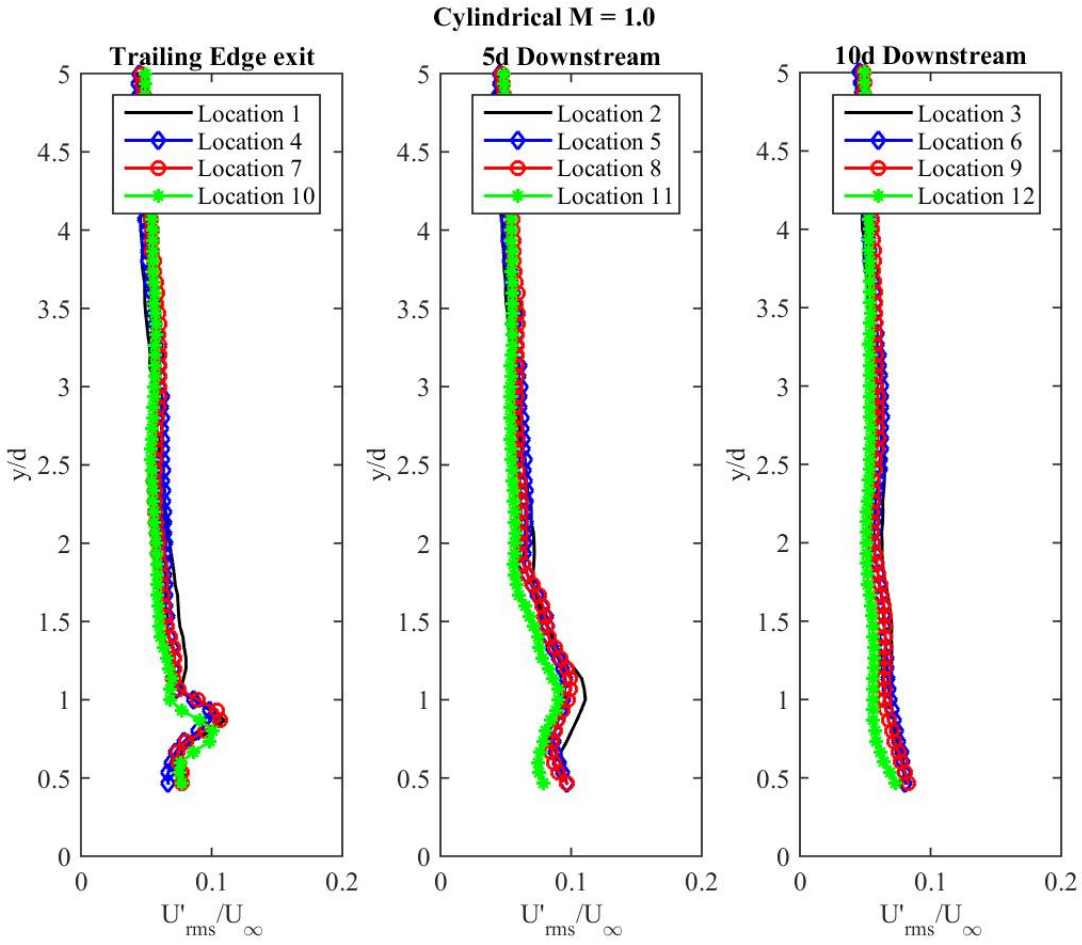

Figure A.6: Turbulence level at trailing edge, 5d and 10d downstream of each cylindrical jet, M = 1

Integral Length Scales

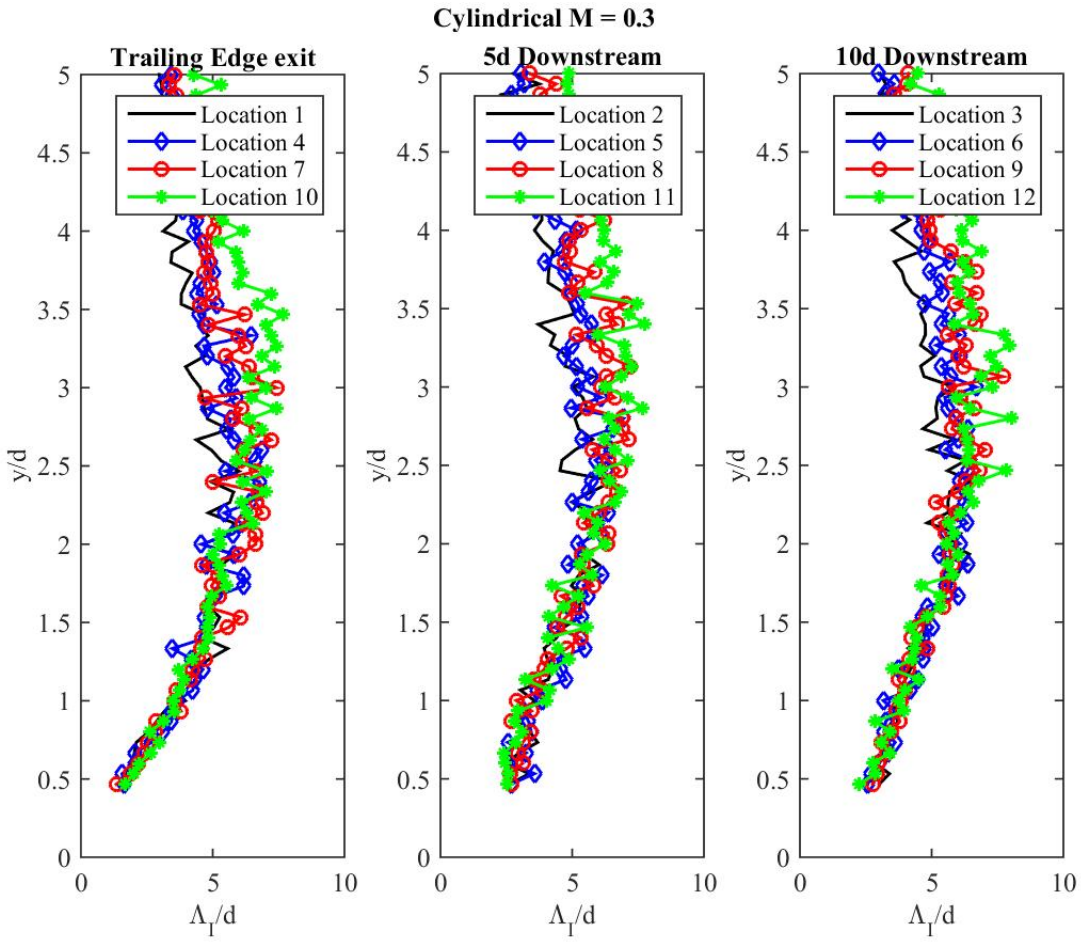

Figure A.7: Integral Length Scales at TE, 5d and 10d downstream of each cylindrical jet, M = 0.3

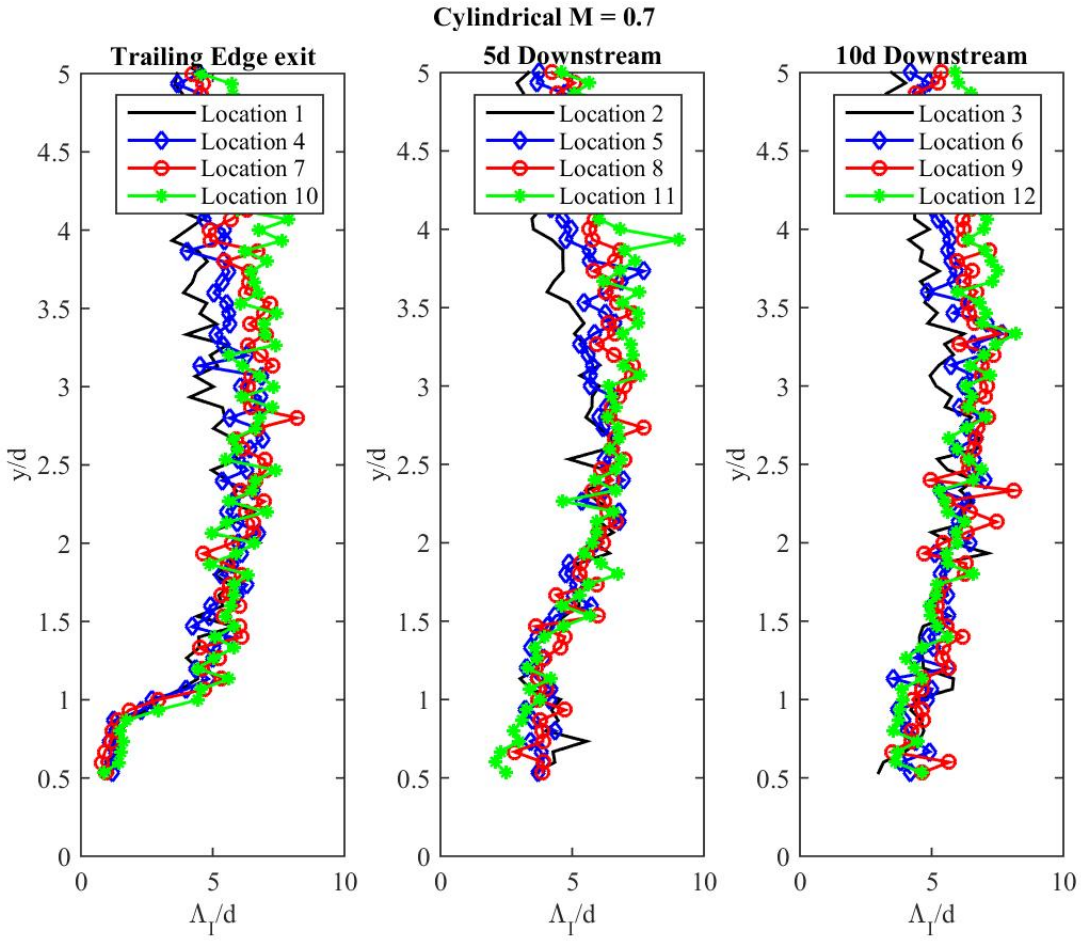

Figure A.8: Integral length scales at TE, 5d and 10d downstream of each cylindrical jet, M = 0.7

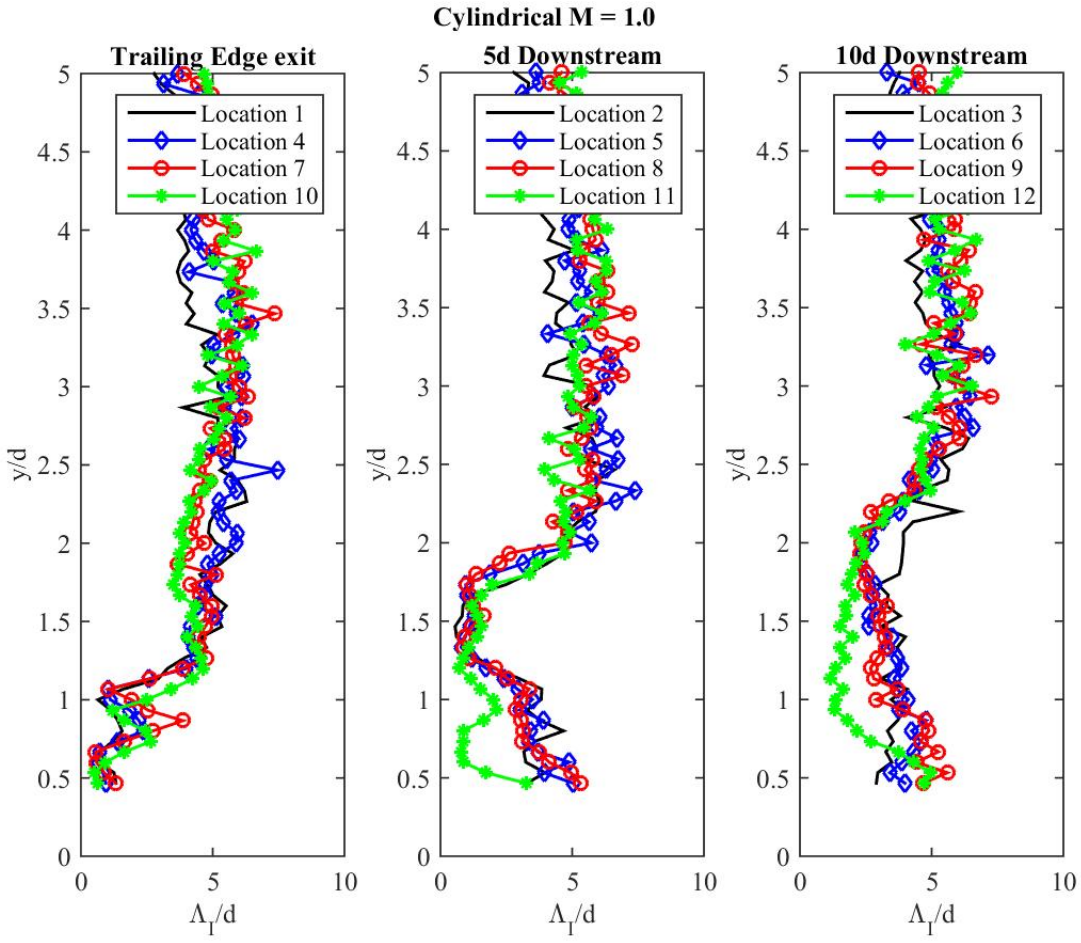

Figure A.9: Integral length scales at TE, 5d and 10d downstream of each cylindrical jet, M = 1.0

Location comparison - diffuser

Average effective velocity

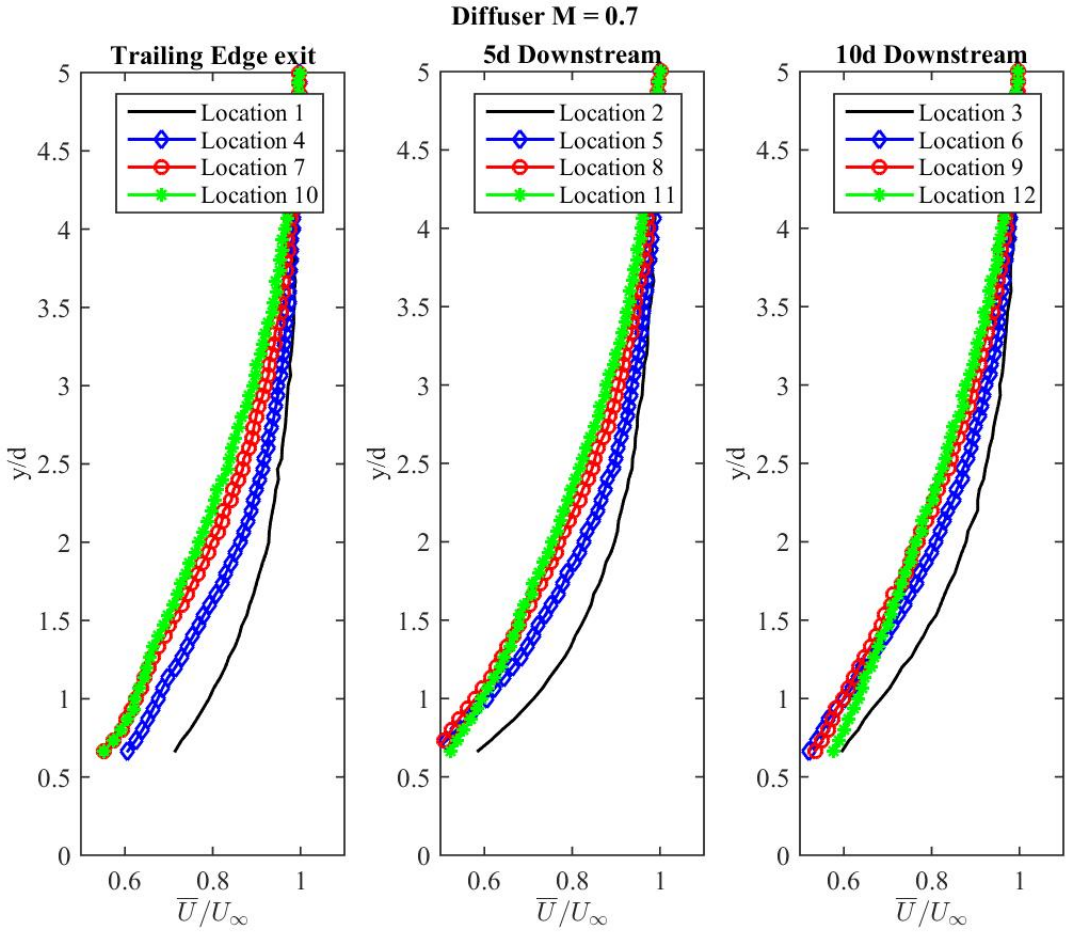

Figure A.10: Average velocity at trailing edge, 5d and 10d downstream of each diffuser jet, M = 0.7

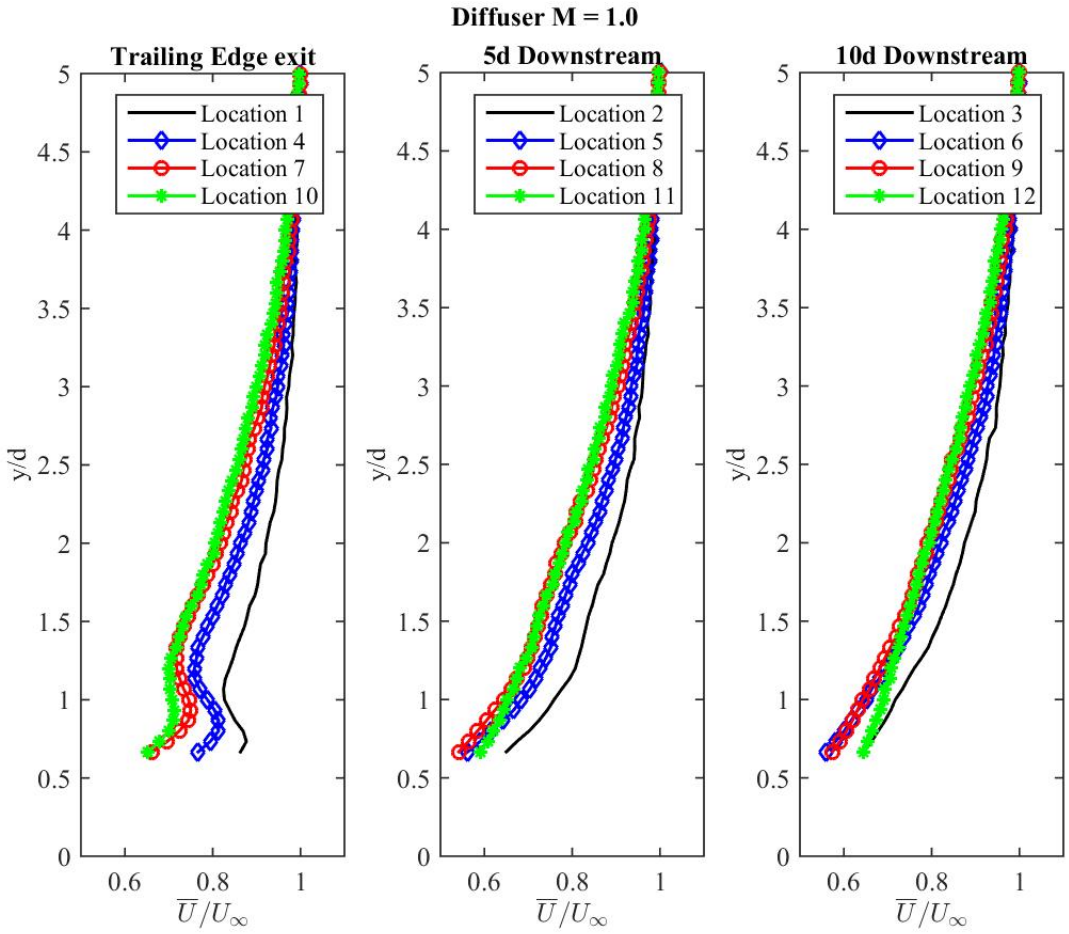

Figure A.11: Average velocity at trailing edge, 5d and 10d downstream of each diffuser jet, M = 1

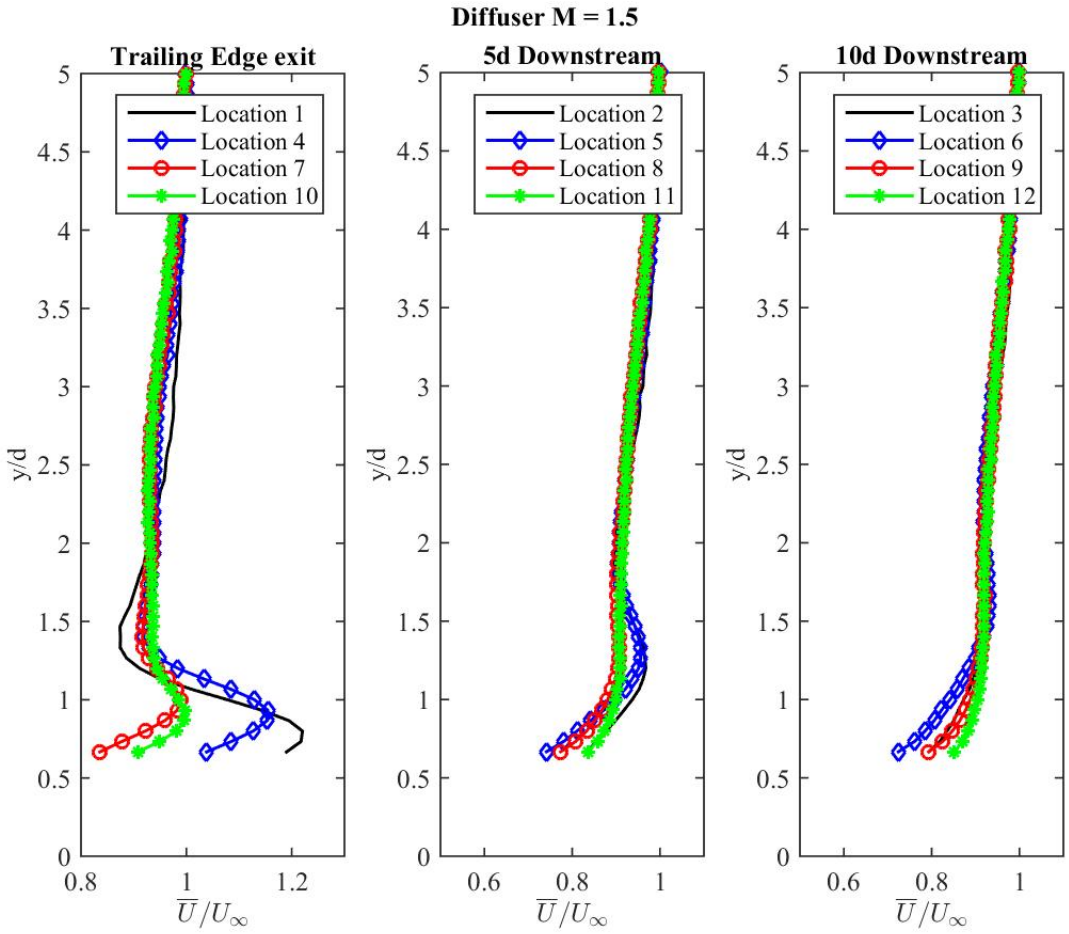

Figure A.12: Average velocity at trailing edge, 5d and 10d downstream of each diffuser jet, M = 1.5

Turbulence Level

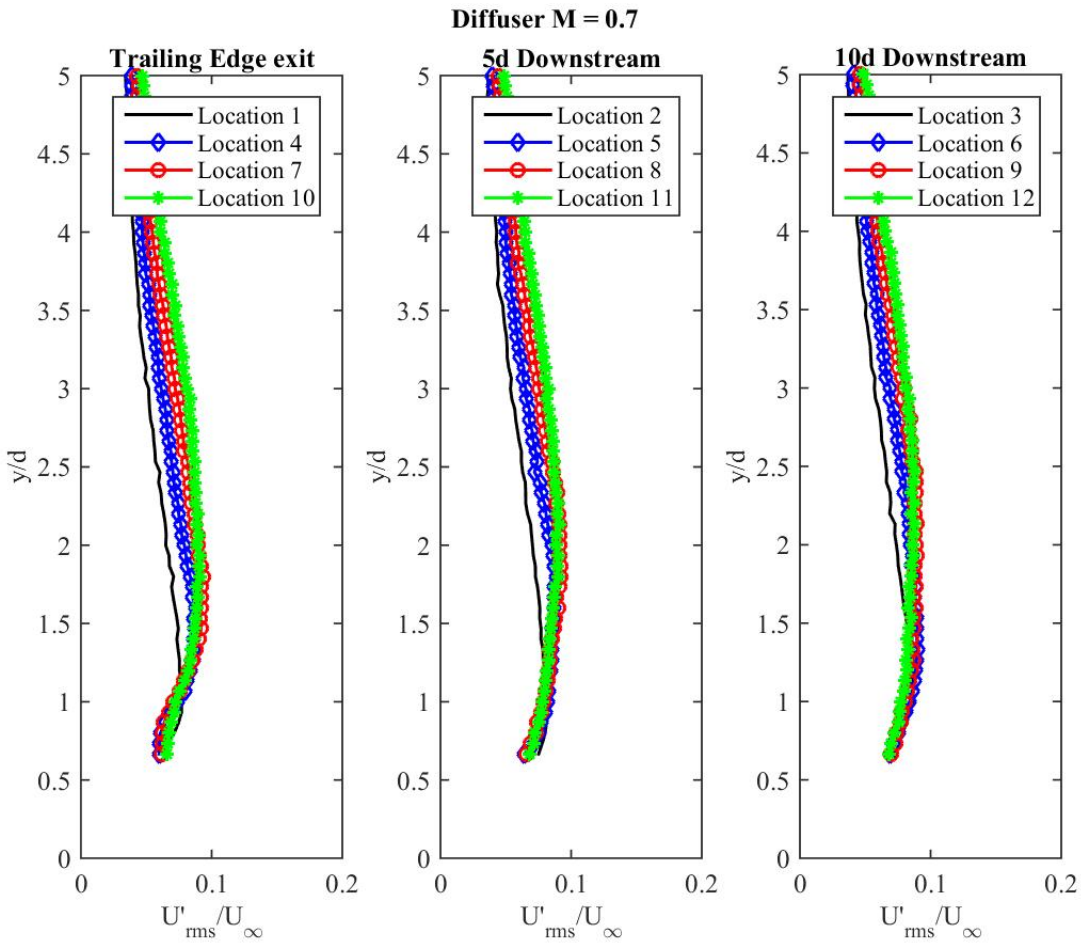

Figure A.13: Turbulence levels at trailing edge, 5d and 10d downstream of each diffuser jet, M = 0.7

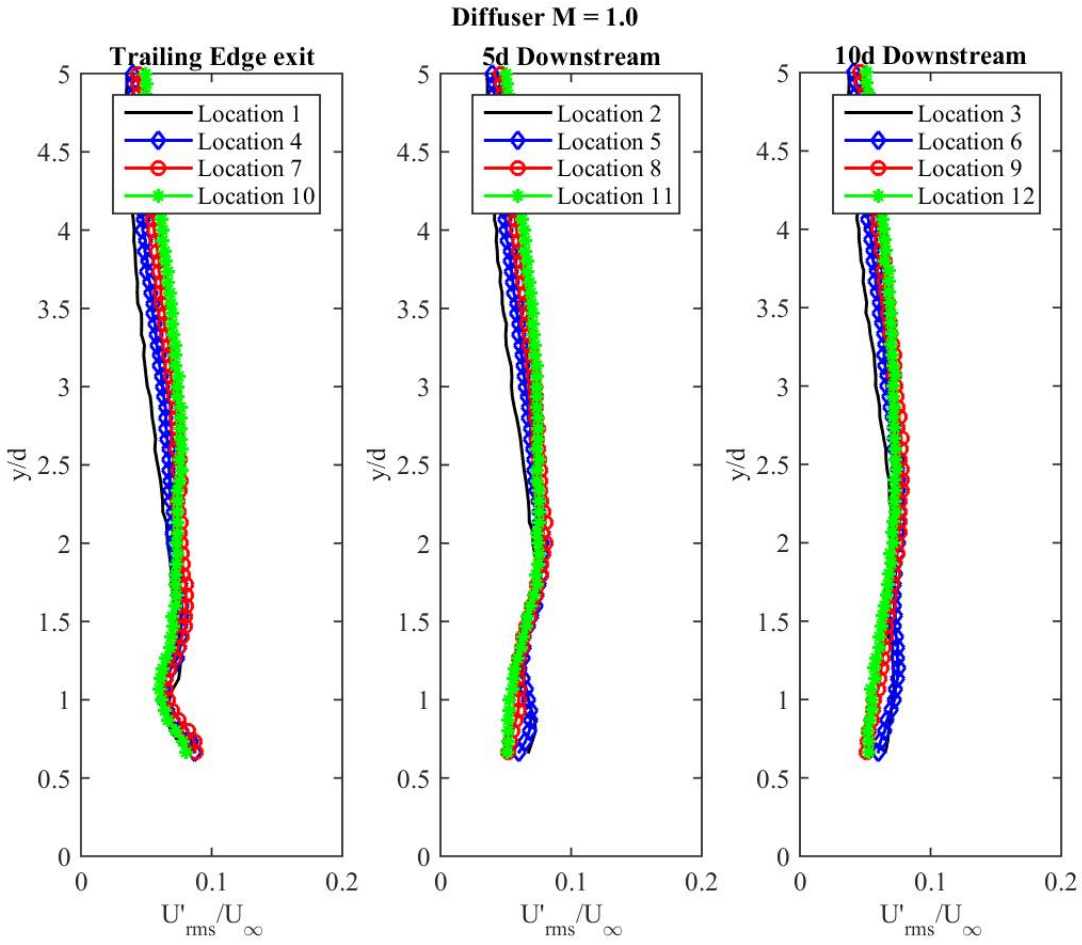

Figure A.14: Turbulence levels at trailing edge, 5d and 10d downstream of each diffuser jet, M = 1

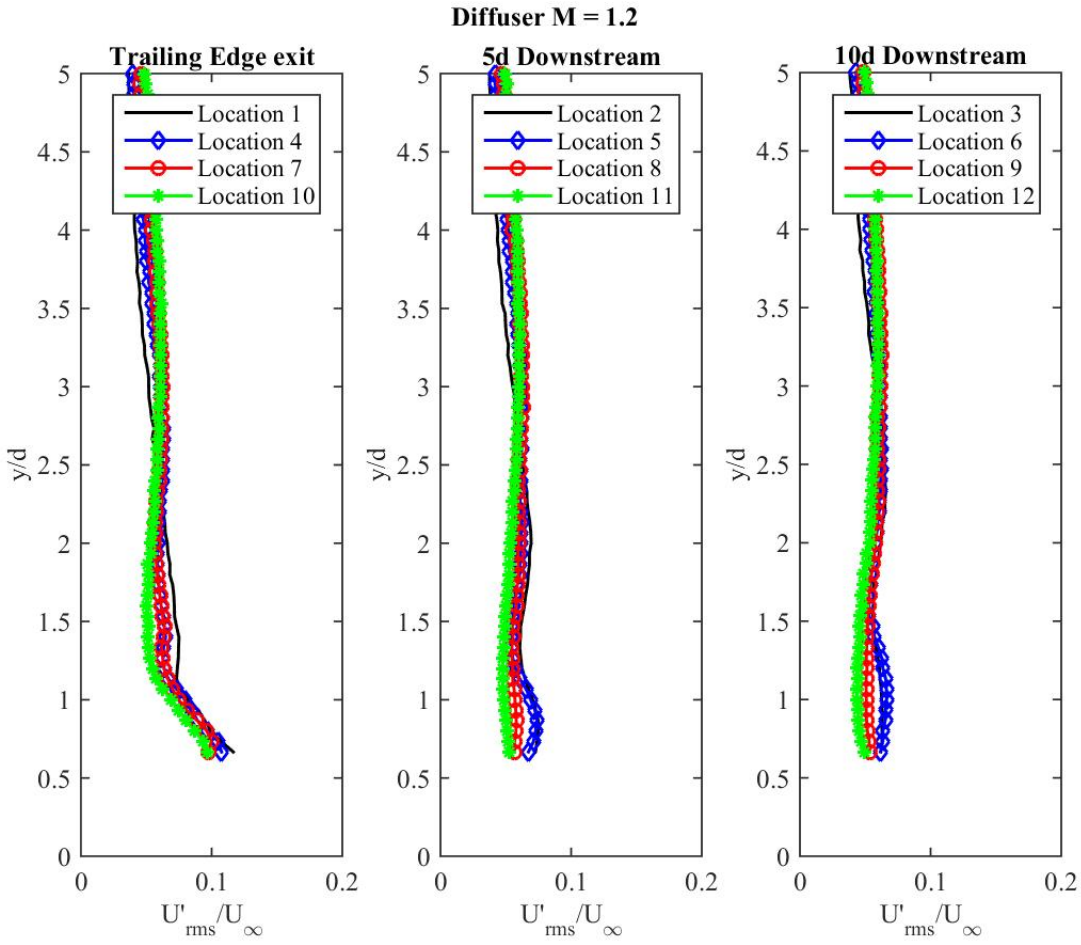

Figure A.15: Turbulence levels at trailing edge, 5d and 10d downstream of each diffuser jet, M = 1.2

Integral Length Scale

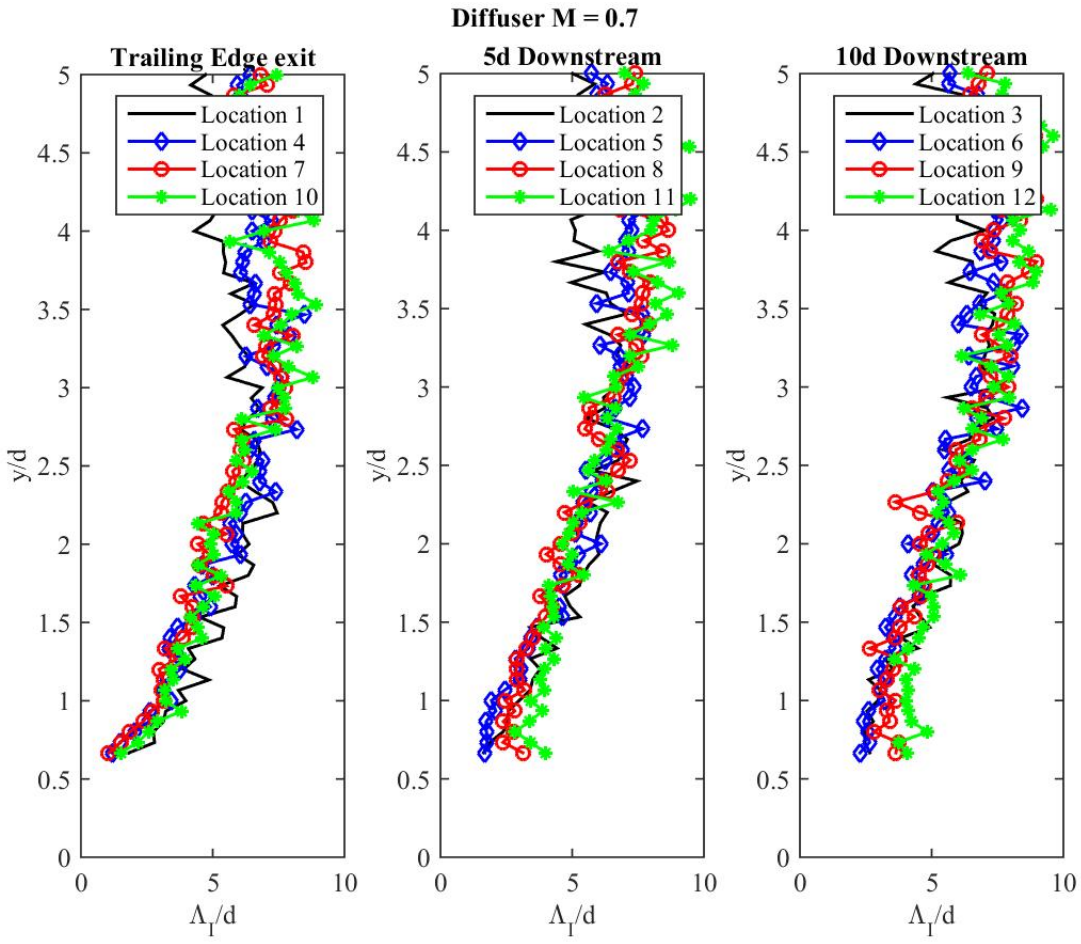

Figure A.16: Integral length scales at trailing edge, 5d and 10d downstream of each diffuser jet, M = 0.7

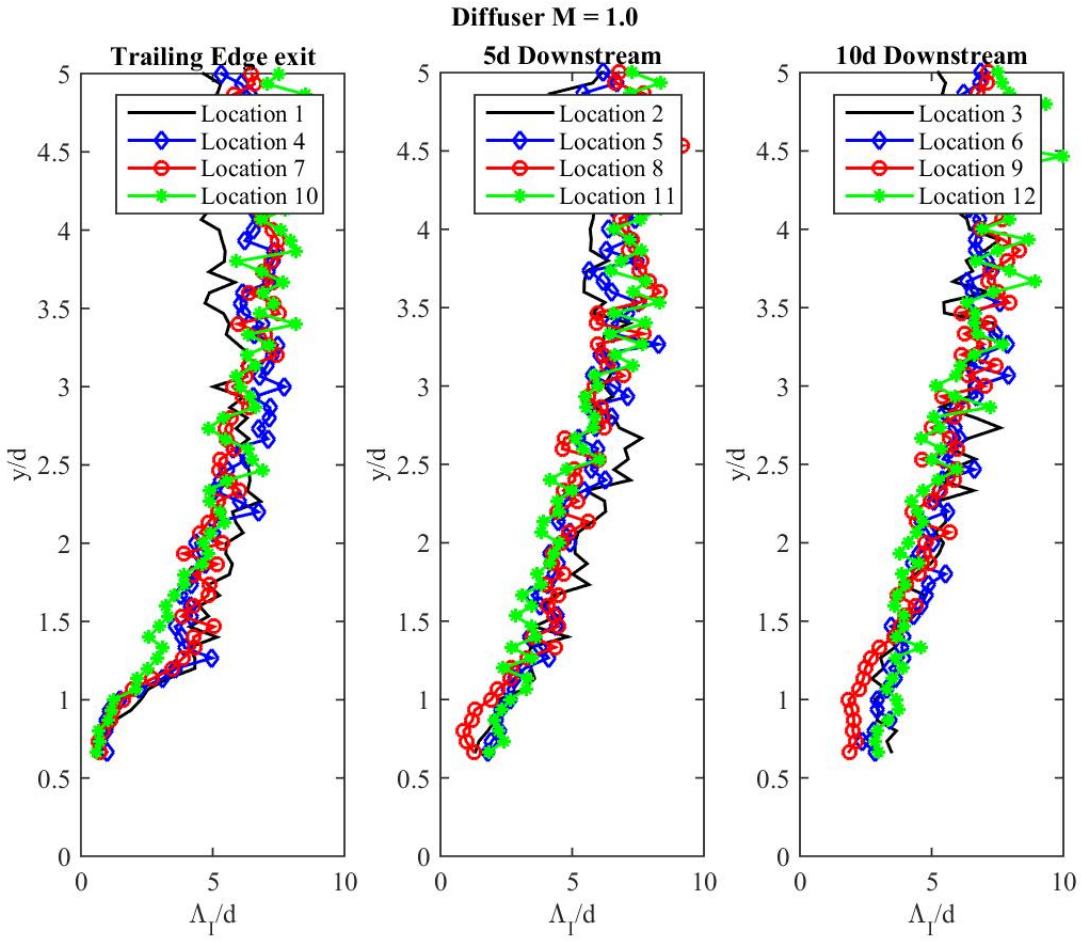

Figure A.17: Integral length scales at trailing edge, 5d and 10d downstream of each diffuser jet, M = 1

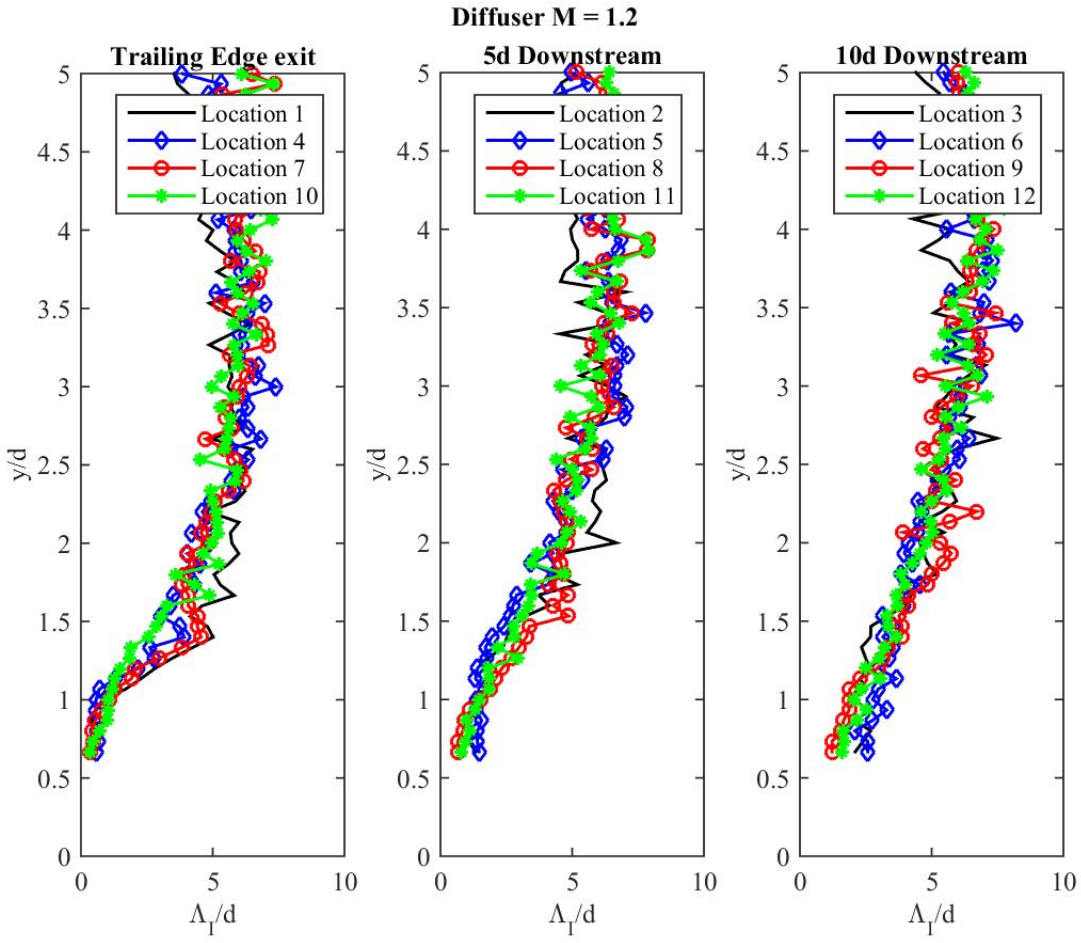

Figure A.18: Integral length scales at trailing edge, 5d and 10d downstream of each diffuser jet, M = 1.2

APPENDIX B: GEOMETRY COMPARISON

Average Axial Velocity

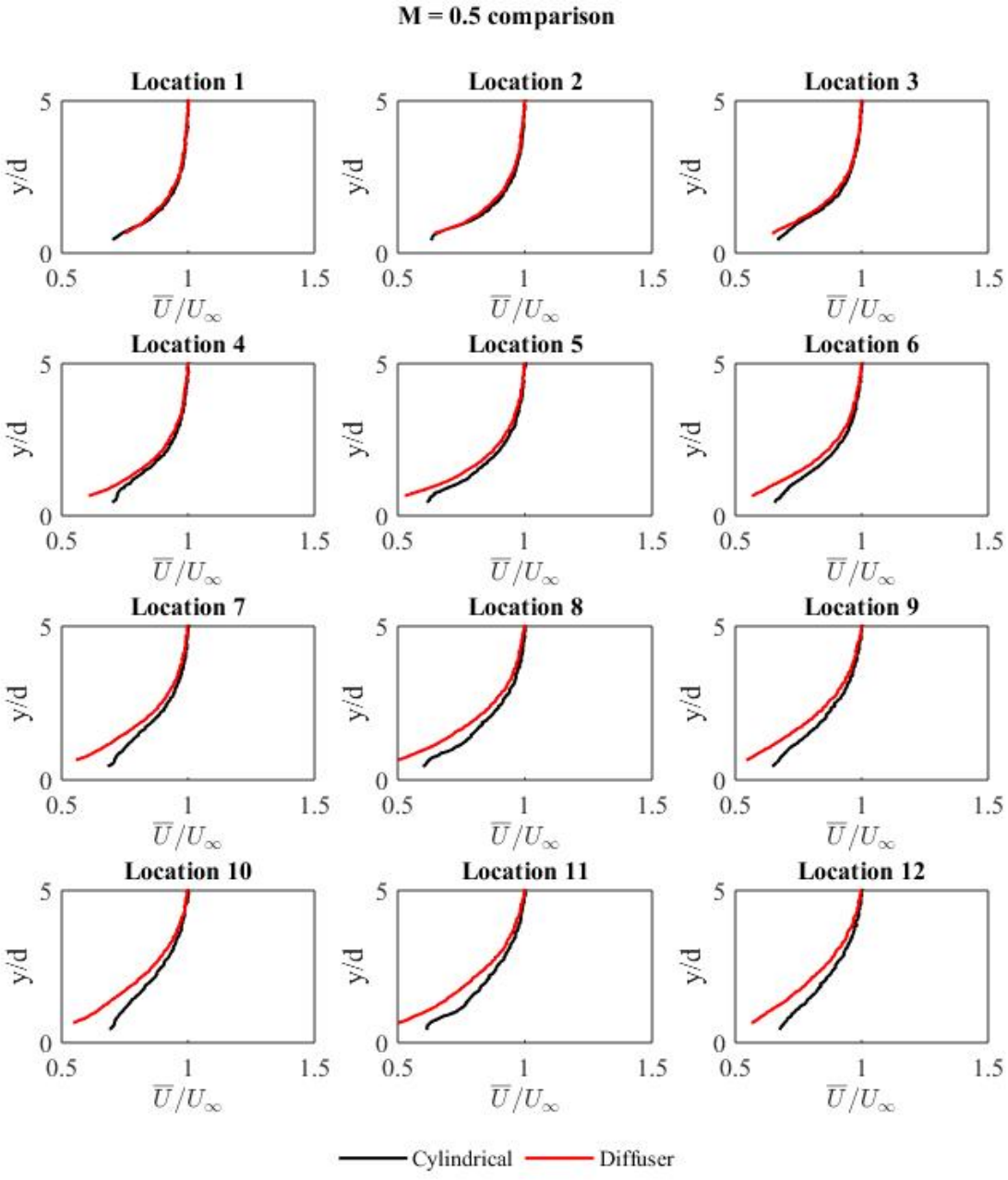

Figure B.1: Average velocity for both geometries - M = 0.5

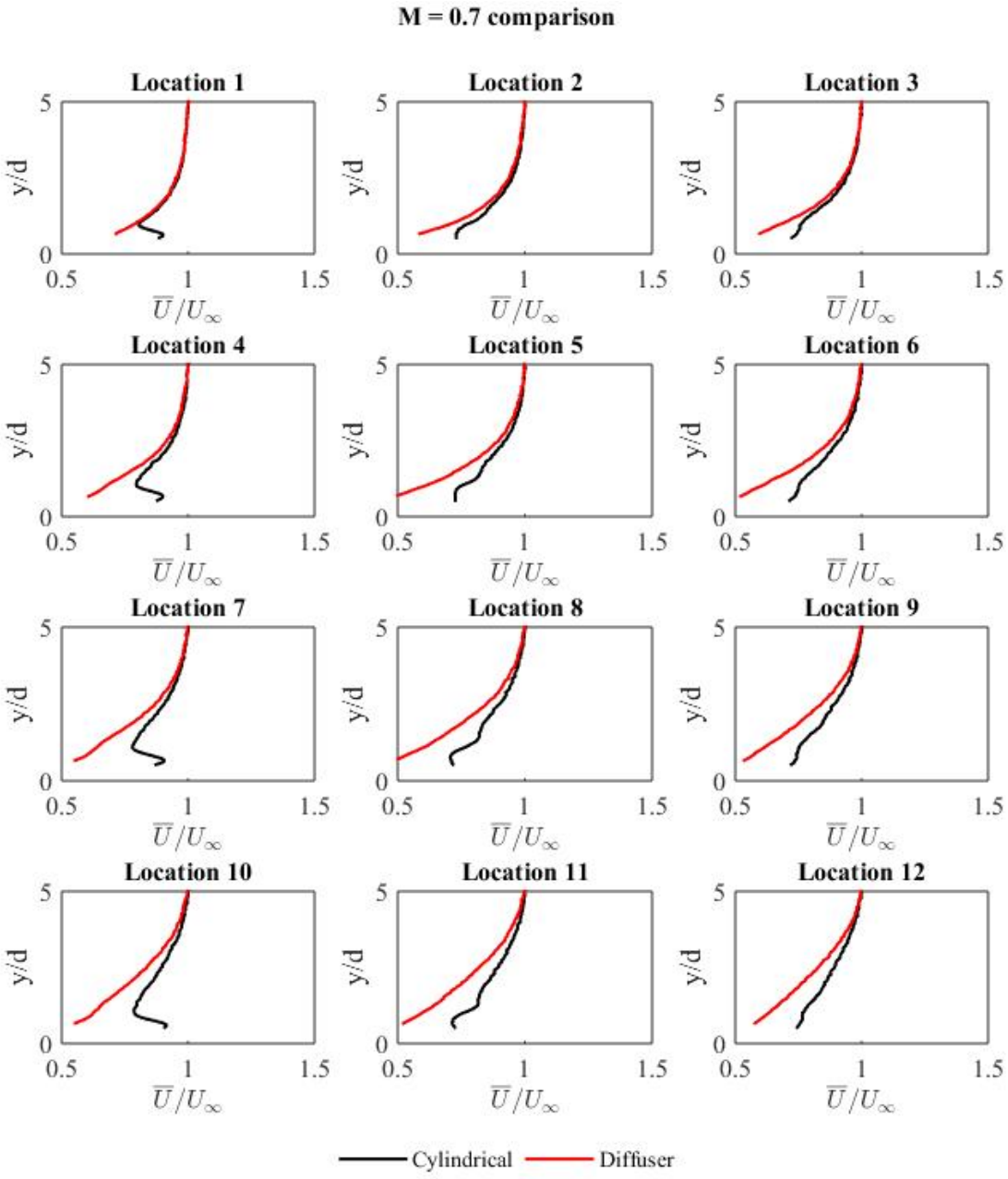

Figure B.2: Average velocity for both geometries - M = 0.7

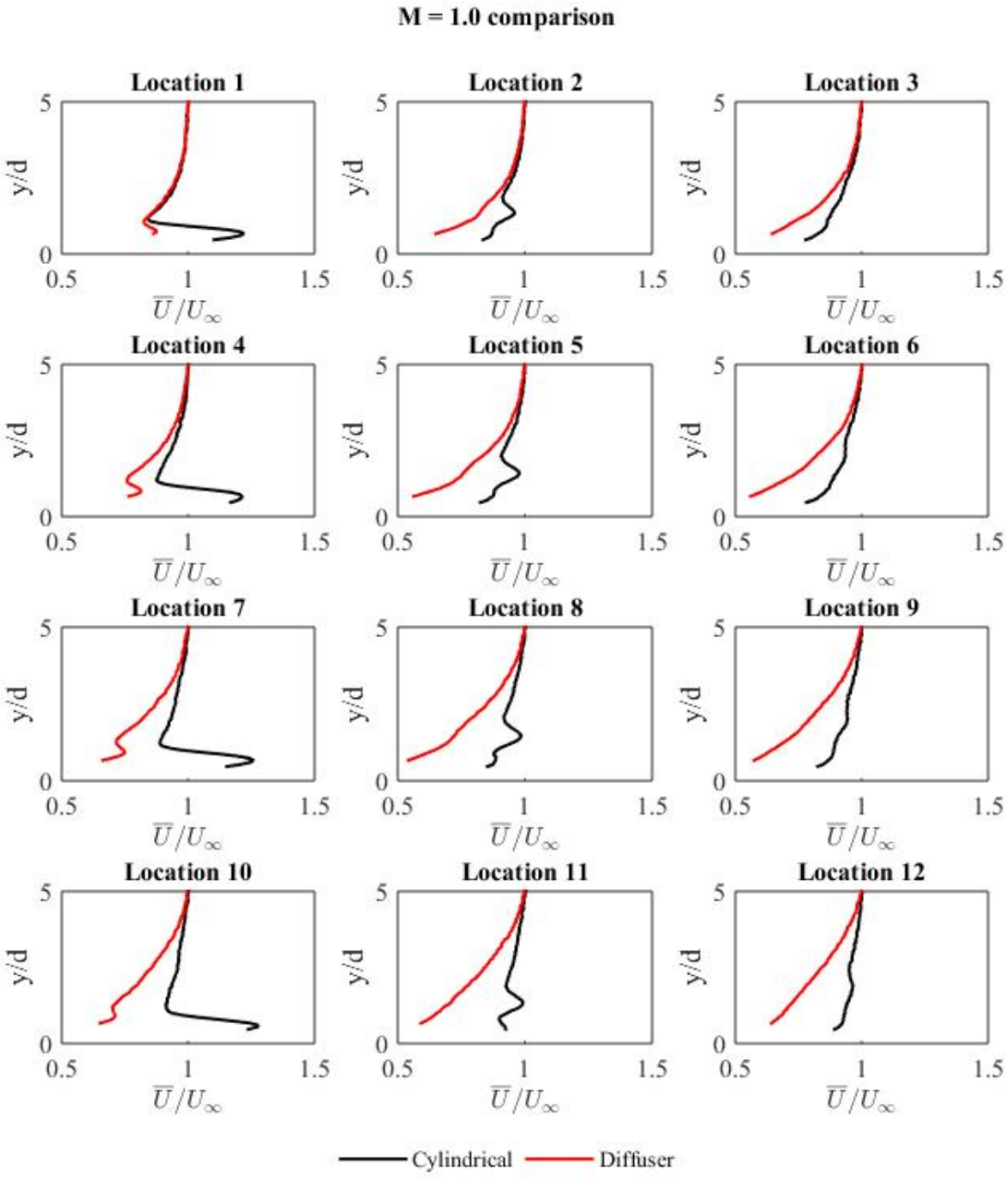

Figure B.3: Average velocity for both geometries - M = 1

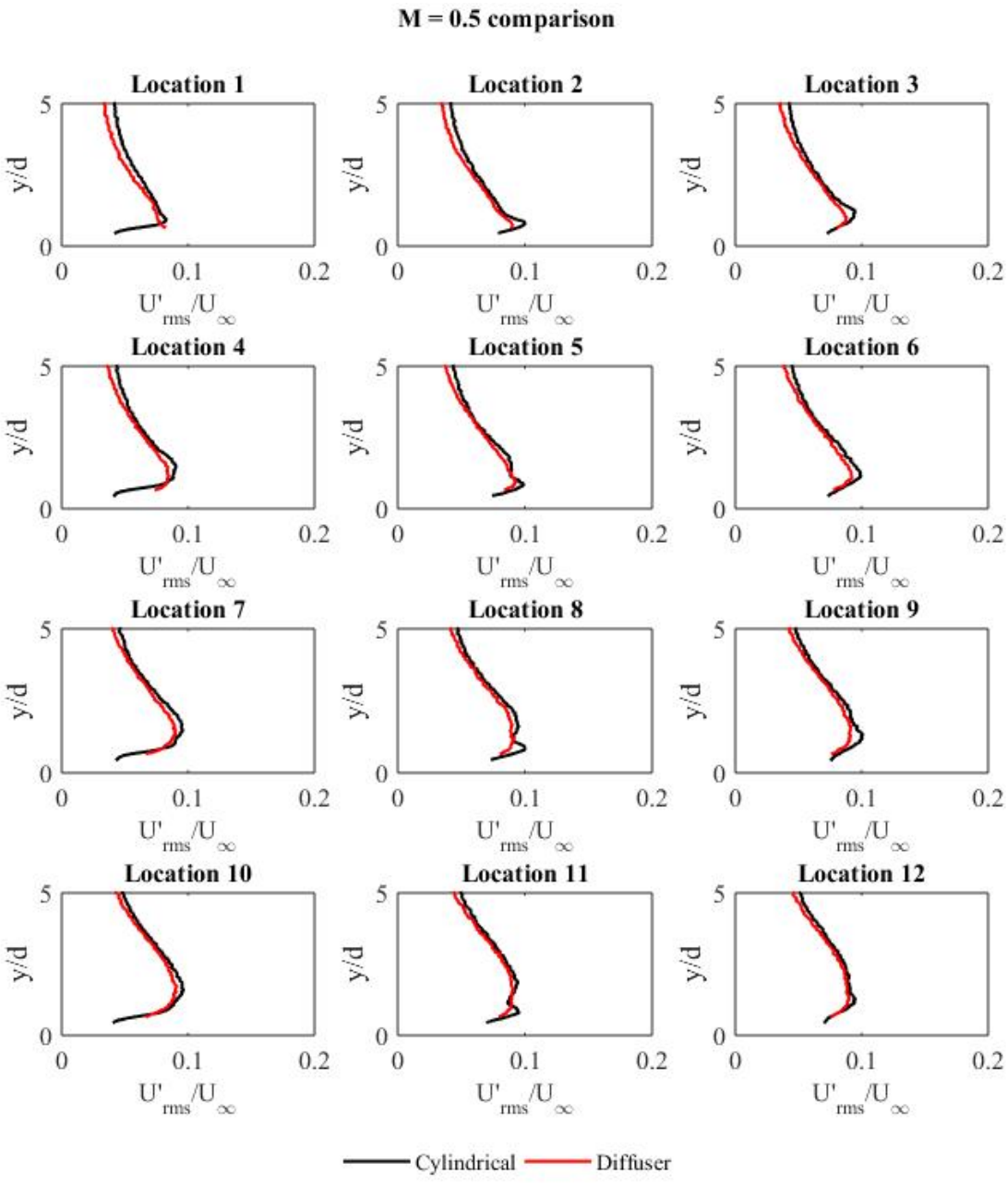

Figure B.4: Turbulence level for both geometries - M = 0.5

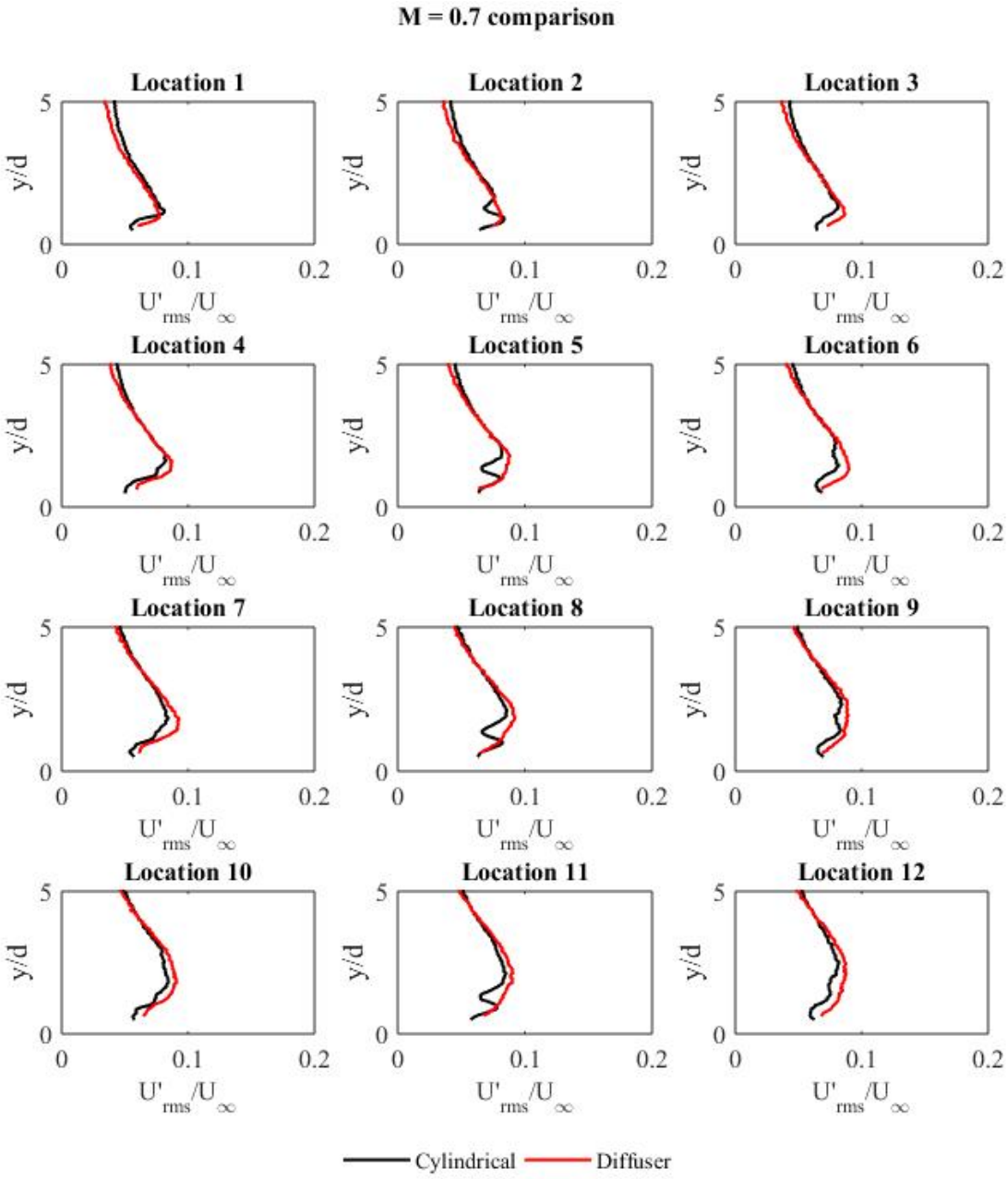

Figure B.5: Turbulence level for both geometries - M = 0.7

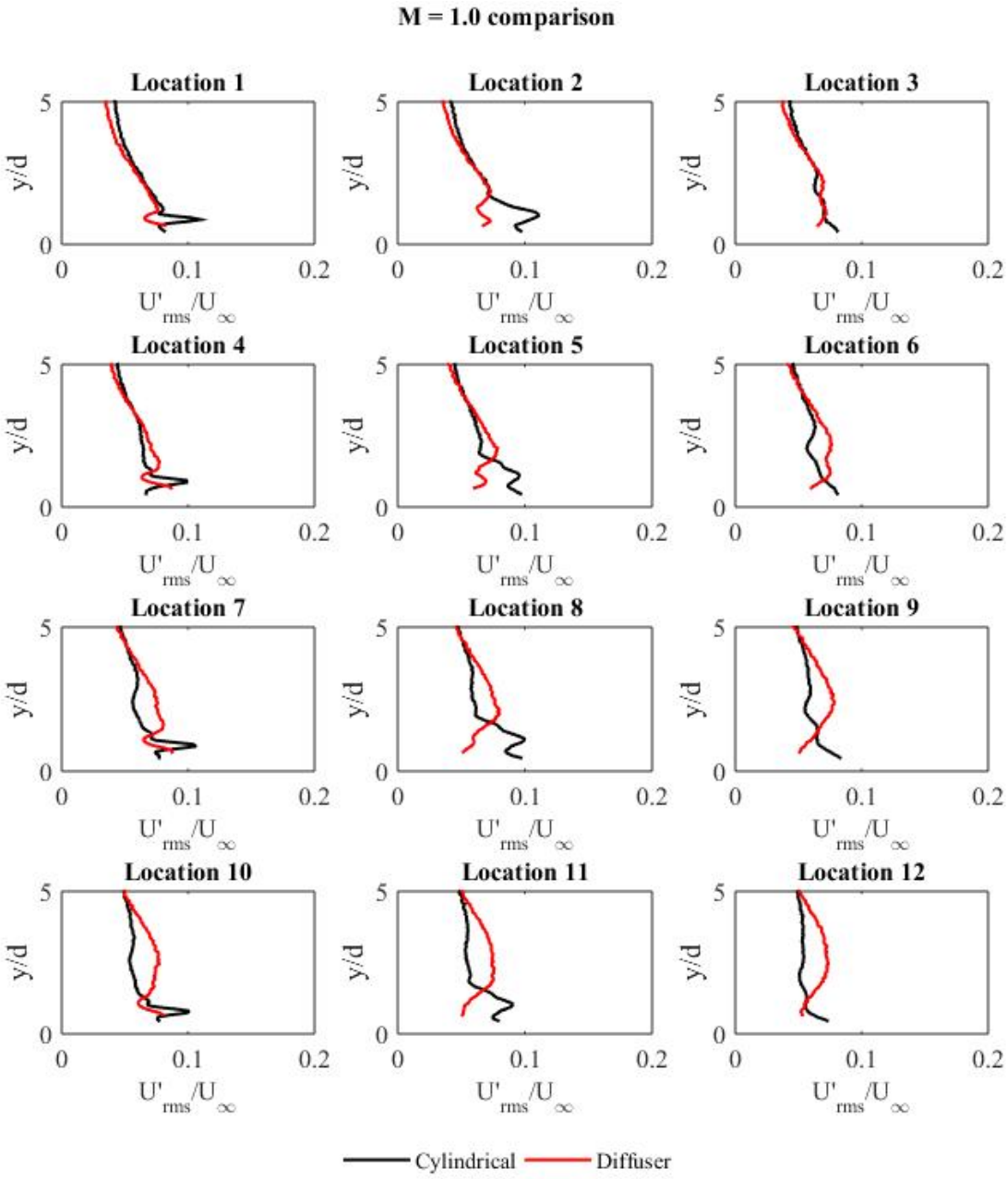

Figure B.6: Turbulence level for both geometries - M = 1

Integral Length Scale

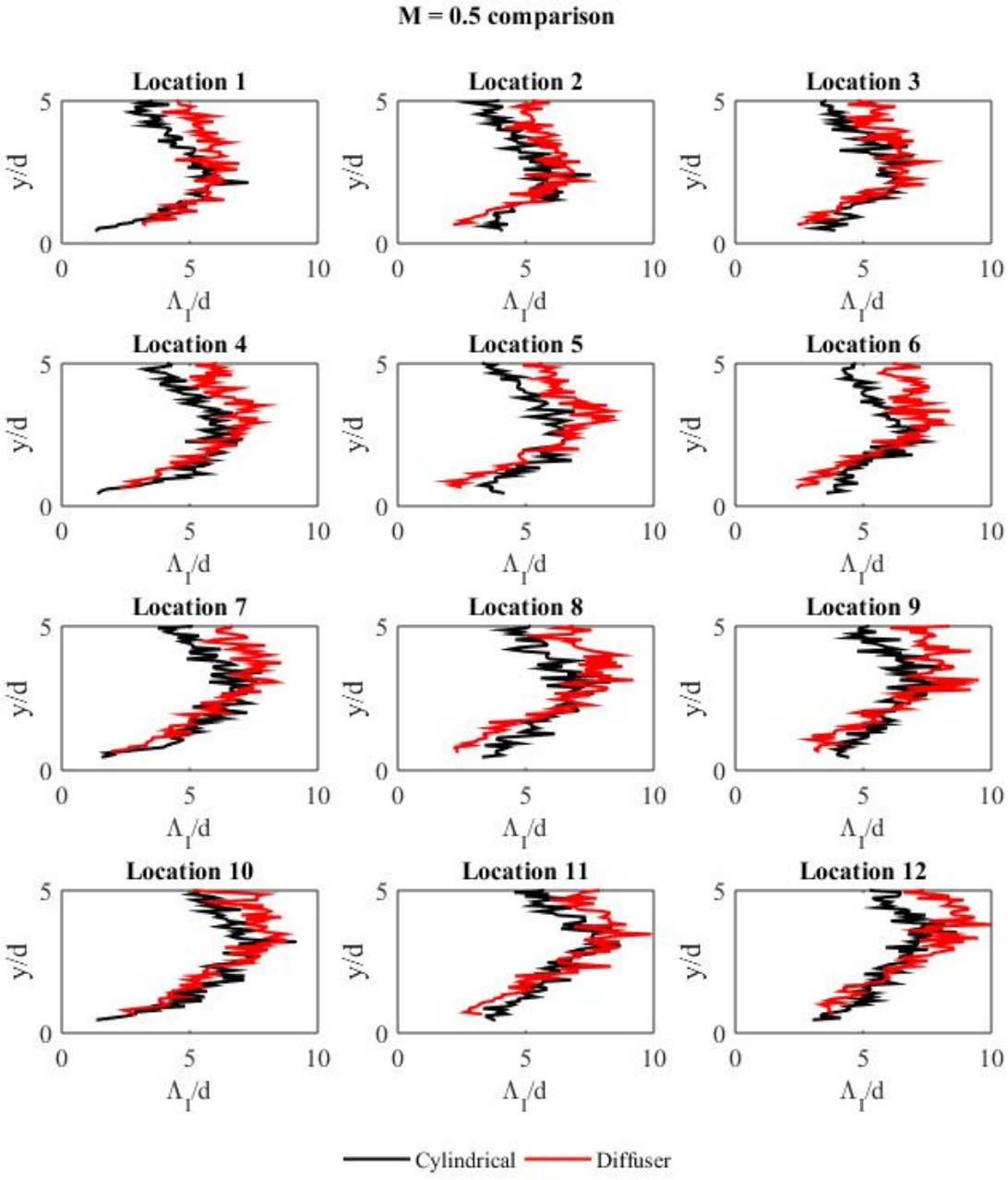

Figure B.7: Integral Length scales for both geometries - M = 0.5

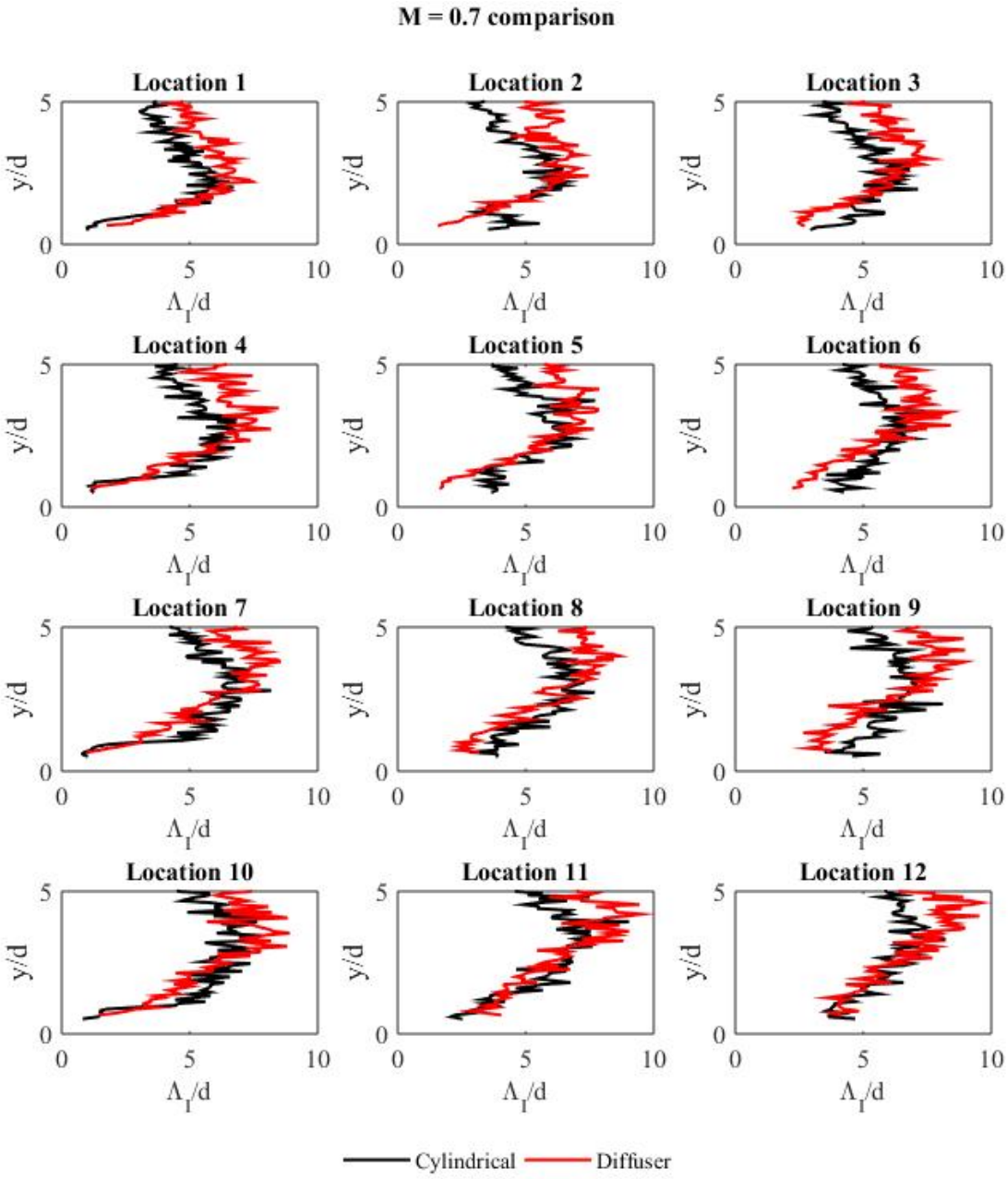

Figure B.8: Integral Length scales for both geometries - M = 0.7

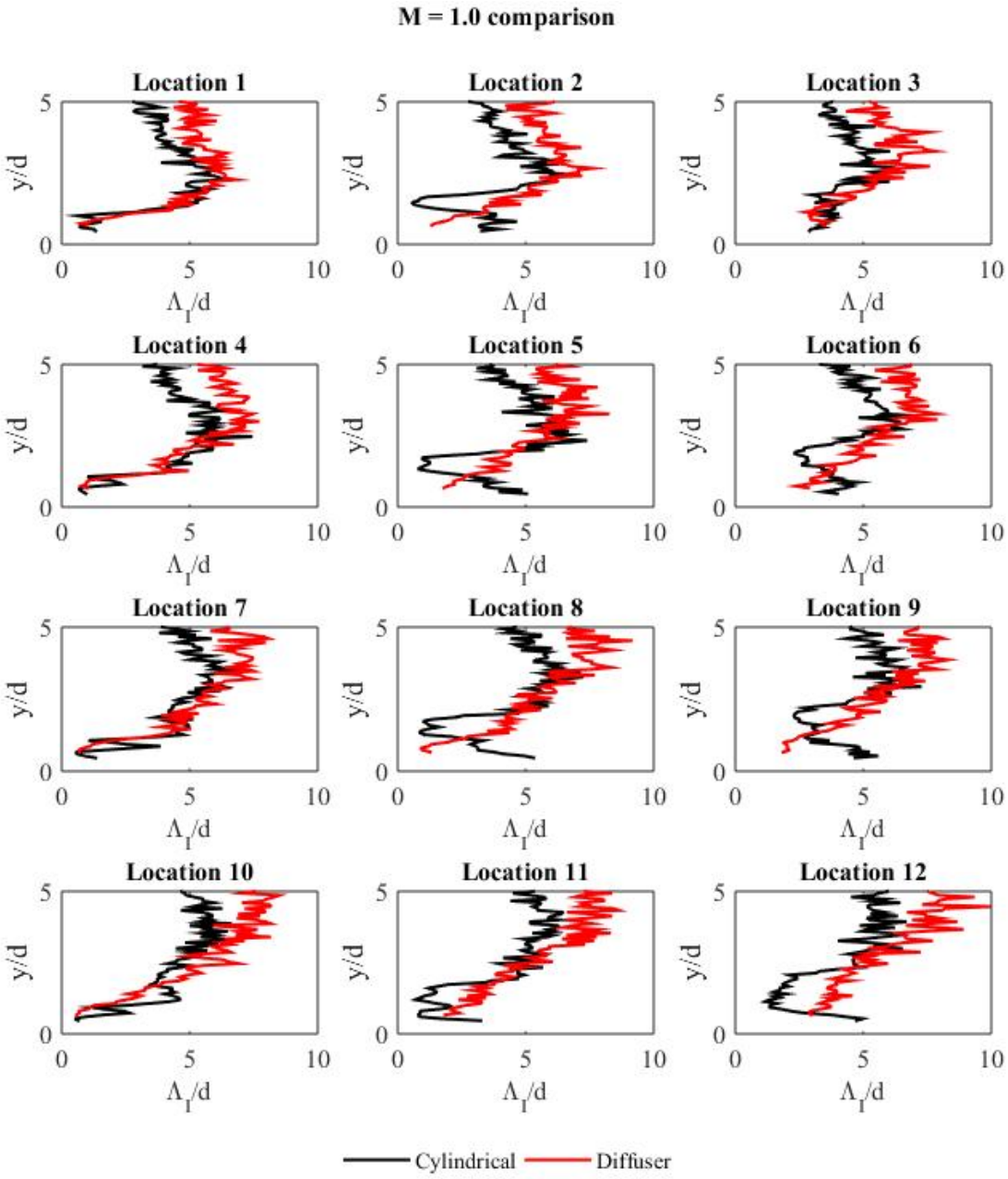

Figure B.9: Integral Length scales for both geometries - M = 1

LIST OF REFERENCES

[1] *Annual Energy Outlook 2017 with projections to 2050,*. U.S.E.I. Administrations, 2017.

[2] Goldstein, R.J., and Thole K, A., *Film Cooling, in Advanced Heat Transfer.* 1971. p. 321-379.

[3] Han, J.C., Dutta, S., and Ekkad, S. V., *Turbine Film Cooling, in Gas Turbine Heat Transfer and Cooling Technology.* 2000. p. 321-379.

[4] Bogard, D.G., and Thole K. A., *Gas Turbine Film Cooling.* Journal of Propulsion and Power, 2006. 22(2): p. 249-270.

[5] Baldauf, S., Scheurlen, M., Schulz, A., and Wittig, S., *Correlation of film cooling effectiveness from thermographic measurements at enginelike conditions.* Journal of Turbomachinery, 2002. 124(4): p. 686-698.

[6] Gritsch, M., Schulz, A., and Wittig, S., *Adiabatic wall effectiveness measurements of film-cooling holes with expanded exits.* Journal of Turbomachinery, 1998. 120(3): p. 549-556.

[7] Burd, S., and Simon, T., *Turbulence spectra and length scales measured in film coolant flows emerging from discrete holes.* Journal of Turbomachinery, 1999. 121(3): p. 554-557.

[8] Burd S. W. , a.S., T. W., *The Influence of Coolant Supply Geometry on Film Coolant Exit Flow and Surface Adiabatic Effectivenes,* in International Gas Turbine and Aeroengine Congress and Exhibition. 1997, ASME: Orlando, Florida, USA.

[9] Kohli, A., and Bogard, D. G., *Adiabatic Effectiveness, Thermal Fields, and Velocity Fields for Film Cooling with Large Angle Injection.* Journal of Turbomachinery, 1997. 119(2): p. 352-358.

[10] Pietrzyk, J.R., Bogard, D.G., *Hydrodynamics Measurements of Jets in Crossflow for Gas Turbine Film Cooling Applications.* Journal of Turbomachinery, 2009. 111: p. 139-145.

[11] Thole, K., Gritsch, M., Schulz, A., and Wittig, S., *Flowfield Measurements for Film-Cooling Holes with Expanded Exits.* Journal of Turbomachinery, 1998. 120: p. 327-336.

[12] Aga, V., Rose, M., and Abhari, R. S., *Experimental flow structure investigation of compound angled film cooling.* 2009, ETH Zurich.

[13] Sen, B., Schmidt, D. L., and Bogard, D. G., *Film Cooling with Compound Angle Holes: Heat Transfer.* Journay of Turbomachinery, 1996. 118(4): p. 800-806.

[14] Takeishi, K., Komiyama M, Oda, Y., Egawa, Y., *Aerothermal Investigations on Mixing Flow Field of Film Cooling with Swirling Coolant Flow.* Journal of Turbomachinery, 2014. 136(5).

[15] Bons, J.P., Macarthur, C. D., Rivir, R. B., *The Effect of High Free-Stream Turbulence on Film Cooling Effectiveness.* Journal of Turbomachinery, 1996. 118(4): p. 814-825.

[16] Wright, L.M., McClain, S.T., Clemenson, *Effect of Freestream Turbulence Intensity on Film Cooling Jet Structure and Surface Effectiveness Using PIV and PSP.* Journal of Turbomachinery, 2011. 133(4).

[17] Wright, L.M., McClain, S.T., Clemenson, *PIV Investigation of the Effect of Freestream Turbulence Intensity on Film Cooling from Fanshaped Holes,* in ASME. Turbo Expo: Power for Land, Sea, and Air. 2011: Vancouver, British Columbia, Canada. p. 493-507.

[18] El-Gabry, L., Thurman, D., Poinsatte, P., and Heidmann, *Turbulence and heat transfer measurements in an inclined large scale film cooling array: Part i: velocity and turbulence measurements,* in ASME TurboExpo 2011. 2011: Vancouver, Canada. p. 541-550.

[19] Eberly, M., and Thole, K., *Time-resolved film-cooling flows at high and low density ratios.* Journal of Turbomachinery, 2014. 7(10): p. 1334-1348.

[20] Bernsdorf, S., Rose, M., Abhari, R., *Modeling of Film Cooling Part i: Experimental Study of Flow Structure.* Journal of Turbomachinery, 2006. 128(1): p. 141-149.

[21] Yavuzkurt, S., Moffat, R. J., and Kays, W. M., *Full-coverage film cooling part 1: three-dimensional measurements of turbulence structure.* Journal of Fluid Mechanics, 1980. 101: p. 129-158.

[22] Abdullah, K., Hisato, O., Ken-ichi, F., and Takeomi, I., *Heat transfer and aerodynamics studies of multiple cooling holes.* International Journal of Gas Turbine, Propulsion and Power Systems, 2012. 127(5): p. 513-520.

[23] Jessen, W., M. Konopka, and W. Schroeder, *Particle-Image Velocimetry Measurements of Film Cooling in an Adverse Pressure Gradient Flow.* Journal of Turbomachinery, 2011. 134(2).

[24] Natsui, G., *Multi-Row Film Cooling Boundary Layers,* in Mechanical and Aerospace Engineering. 2015, University of Central Florida.

[25] Dantec Dynamics, *StreamWare pro installation and user guide.* Denmark, 2013.

[26] TSI, *IFA 300 Constant Temperature Anemometer System Instructional Manual.*

[27] Tennekes, H., and Lumley, J.L., *A First Course in Turbulence.*

[28] Natsui, G., Little Z., Kapat, J., Socotch, A., Wang, A, and Dees, J. E., *Adiabatic Film Cooling Effectiveness measurements throughout multi-row film cooling arrays.* ASME. Turbo Expo: Power for Land, Sea and Air, Volume 5C: Heat Transfer. doi: 10.1115/GT2016-56183.

[29] Jorgensen, Finn E., *How to measure turbulence with hot-wire anemometers - a practical guide* 2002. Dantec Dynamics.

[30] El-Gabry, L. A., Thurman, D. R., Poinsatte, P. E., *Procedure for Determining Turbulence Length Scales Using Hotwire Anemometry.* NASA/TM, 2014.

[31] Bell, J. H., Mehta, R. D., *Contraction Design for Small Low-Speed Wind Tunnels.* National Aeronautics and Space Administration, 1998 Sanford University.

[32] Roach, P. E., *The generation of nearly isotropic turbulence by means of grids.* Journal of Heat and Fluid Flow, Vol. 8, pp. 82-92.